ABSTRACT

Title of Document: METER SCALE HETEROGENEITIES IN THE OCEANIC MANTLE REVEALED IN OPHIOLITE PERIDOTITES

Mitchell Bruce Haller, Master of Science, 2017

Directed By: Professor Richard J. Walker
Department of Geology

The upper oceanic mantle is the largest accessible terrestrial geochemical reservoir. Numerous aspects of the upper oceanic mantle's current state, as well as its chemical evolution through time, remain obscure. Although studies of Mid Ocean Ridge Basalts (MORB), and other oceanic mantle-derived melts have provided important insights into the nature of their sources, previous studies have shown that they fail to capture the full range of end-member compositions present in oceanic peridotites. Ophiolites are especially useful in interrogating this issue as field-based observations can be paired with geochemical investigations over a wide range of geologic time. Grid sampling methods (3m x 3m) at the 497 Ma Leka Ophiolite Complex (LOC), Norway, and the 1.95 Ga Jormua Ophiolite Complex (JOC), Finland, offer an opportunity to study mantle domains at the meter and kilometer scale, and over a one billion year timespan. The lithology of each locality predominately comprises harzburgite, hosting layers and lenses of dunite and pyroxenite. Here, we combine highly siderophile elements (HSE) and Re-Os isotopic analysis of these rocks with major and trace element measurements.

Two grids sites are studied within the LOC harzburgite mantle section. Harzburgites at individual LOC grid sites show variations in initial $\gamma Os_{(497\ Ma)}$ (-2.1 to +2.2) at the meter scale. Analyses of dunites within the same LOC grid, reveal that dunites may either have similar γOs to their host harzburgite, or different, implying interactions between spatially associated rock types may differ at the meter scale. A harzburgite sample is characterized

by low initial $^{187}Os/^{188}Os$ (<0.121), reflecting Proterozoic melt depletion. Preservation of Os isotopic compositions consistent with ancient melt depletion is a common characteristic in oceanic peridotites. Grid sampling of adjacent harzburgites and dunites reveal that the geometry of these refractory domains can be constrained to be < 1 m^3. T_{MA} model ages of an LOC websterite reveals at least one other stage of partial melting in the LOC, which broadly corresponds to the opening of the Iapetus Ocean (~620 – 550 Myr). Averaged γOs values between the mantle sections of two LOC grid sites (+1.3 and -0.4) separated by ~5 km, indicate km-scale heterogeneity in the convecting upper mantle. Major and trace element compositions suggest that the km-scale heterogeneity in the LOC, is a result of variable melt-extraction at different depths, and local scale processes. Analyses of two, 1 cm thick orthopyroxenite veins, hosted by harzburgite near Kvaløya-moen, are more radiogenic than host harzburgites, and suggest vein formation had minimal impact on the host harzburgite. Whole rock major and trace element data, and thin sections of relict olivine grains, are also examined to shed light on the causes of the isotopic heterogeneities in the LOC.

Two grids sites are studied within the JOC serpentinite mantle section. Serpentinites at JOC grid JU15-16, display modest heterogeneities at the meter scale in $\gamma Os_{(1.95\ Ga)}$ (-0.5 to -3.0). T_{RD} model ages show evidence of melt depletion at least 400 Ma prior to the accepted age of the ophiolite. Re-Os systematics of a separate JOC grid site, JU15-18 (~3 km away), show evidence of Re addition/loss at the age of the ophiolite (~1.95 Ga). LREE-enriched REE patterns suggest that this grid location was subsequently affected by metasomatic processes possibly associated with gabbroic dykes, affecting the geochemical and Os isotopic compositions of these JOC serpentinites. Enrichments of fluid mobile elements including Re, Ba, and Sr, may implicate recent Re mobilization caused by weathering and ground-water interactions. Trends in major elements show signs of variable MgO and SiO_2 loss by serpentinization.

Meter Scale Heterogeneities in the Oceanic Mantle Revealed in Ophiolite Peridotites

by

Mitchell B. Haller

Thesis submitted to the Faculty of the Graduate School of the
University of Maryland, College Park in partial fulfillment
of the requirements for the degree of
Master of Science
2017

Advisory Committee:

Professor Richard J. Walker, Chair
Associate Professor Sarah Penniston-Dorland
Research Scientist Igor S. Puchtel

Table of Contents

1. INTRODUCTION

1.1. Upper Oceanic Mantle

The oceanic mantle, or DMM (depleted mid-ocean ridge mantle), is the largest accessible geochemical reservoir on Earth. Mid Ocean Ridge Basalts (MORB) are produced by partial melting of upwelling DMM at divergent plate boundaries. Residual oceanic lithospheric mantle forms as a result (Dick et al., 1984). Indirect studies of the DMM based on MORB, and more direct studies of abyssal and ophiolite peridotites from the oceanic lithospheric mantle have shown chemical and isotopic heterogeneity among ocean basins, along mid-ocean ridges, as well as centimeter to kilometer scale local heterogeneities (Dick et al., 1984; Sharma et al., 1995; Workman & Hart, 2005; Warren et al., 2009). These heterogeneities are thought to have resulted from processes including: variable melt depletion, metasomatism, refertilization, lithospheric recycling, and melt-rock reactions. (Allégre & Turcotte, 1986; Snow et al., 1994; Sharma & Wasserburg, 1996; Liu et al., 2009; Warren et al., 2009). The causes, timing, relative impact, and extent of these processes is however, still poorly understood. Further work investigating these processes is crucial for advancing our understanding of the composition of this major terrestrial reservoir, how the DMM has evolved throughout time, and assessing the extent of mantle mixing today.

Although extensive studies of MORB and other oceanic mantle-derived melts have provided important insights into the nature of their sources, previous studies have shown that MORB fail to capture the full range of end-member chemical and isotopic compositions present in mantle peridotites (Brandon et al., 2000; Alard et al., 2005; Harvey et al., 2006; Lui et al., 2008; Rampone & Hofmann, 2012). Due to the relationship between the oceanic crust (MORB) and its underlying residual mantle (peridotites), both are

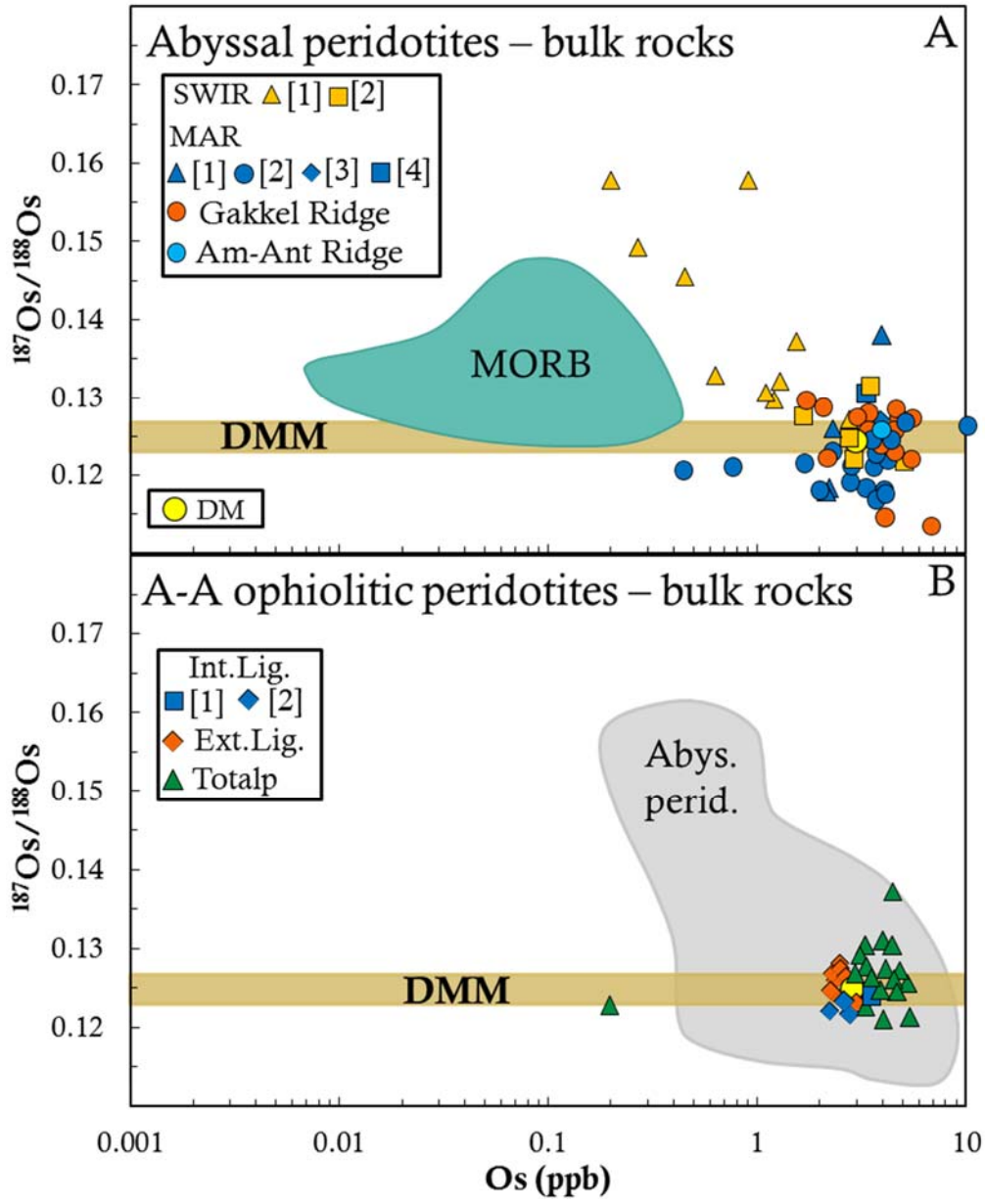

Figure 1. Os concentrations (in ppb) vs. Os isotopic composition of bulk rock abyssal peridotites and Alpine–Apennine ophiolitic peridotites. Figures adapted from Rampone and Hofmann (2012). (**A**) South West Indian Ridge (SWIR): [1] Standish et al. (2002), [2] Snow and Reisberg (1995); Mid Atlantic Ridge (MAR): [1] Standish et al. (2002), [2] Harvey et al. (2006), [3] Brandon et al. (2000), [4] Alard et al. (2005); Gakkel Ridge (Liu et al., 2008); and American–Antarctic Ridge (Snow and Reisberg, 1995). Also shown are the compositional field of global MORBs (after Gannoun et al., 2007) and the Depleted MORB Mantle (DM) average (after Snow et al., 2000). (**B**) Alpine–Apennine ophiolitic peridotites, Internal Ligurides: [1] Alard et al., (2005), [2] Snow et al., (2000); External Ligurides (Snow et al., 2000); and the Totalp ophiolite complex (Van Acken et al., 2008). The gray field refers to the abyssal peridotite compositions, in **A**.

expected to have identical initial Hf, Sr, Nd, Pb, and Os isotopic compositions at the time of primary melting, assuming: (1) a homogeneous mantle source; (2) partial melting under equilibrium conditions; and (3) the melt is not contaminated during extraction and solidification (Rampone & Hofmann, 2012). However, recent isotopic studies of peridotites present in modern oceanic environments and ophiolites have shown significant heterogeneities in their Sr, Nd, Hf, and Os compositions at variable length scales, beyond those observed in MORB (Sharma et al., 1995; Alard et al., 2005; Harvey et al., 2006; Liu et al., 2009; Warren et al., 2009; Stracke et al., 2011; Burton et al., 2012; Rampone & Hofmann, 2012: **Fig. 1**). In order to investigate heterogeneity further, direct sampling of oceanic mantle is advantageous.

Oceanic mantle is primarily sampled through the dredging and drilling of abyssal peridotites, which are commonly interpreted to be the residues of the DMM after partial melting at mid-ocean ridges. Abyssal peridotites are useful in providing access to the present-day mantle compositions beneath ridge segments. However, because of the method by which they are sampled, rarely are they associated with petrological or spatial context (Brandon et al., 2000; Warren et al. 2009).

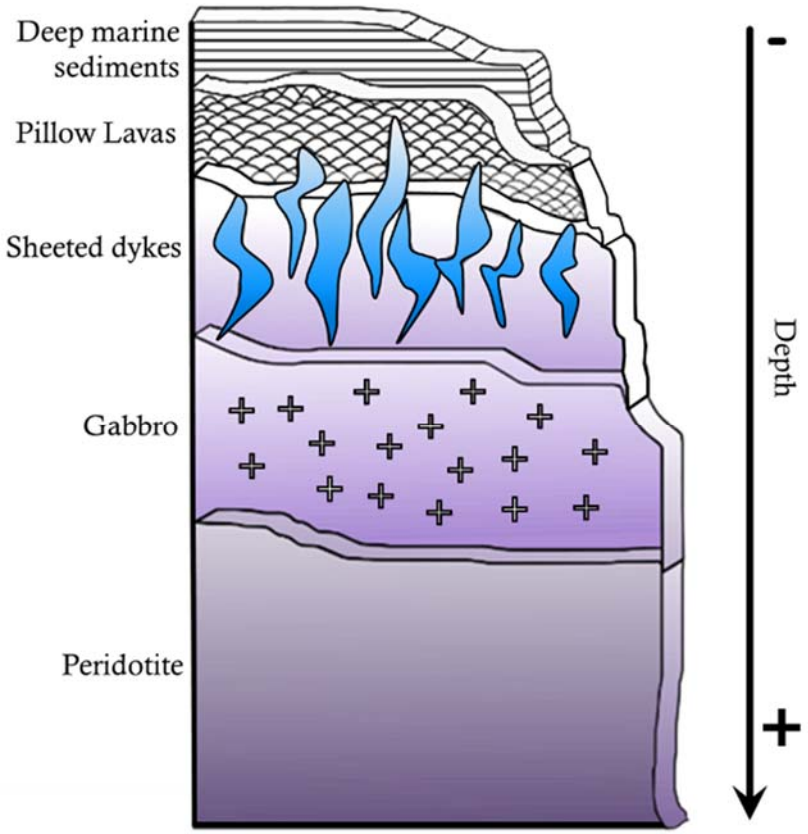

Figure 2. Idealized stratigraphic sequence of an ophiolite, with upper mantle peridotites at the bottom.

Oceanic mantle can also be sampled as ophiolitic peridotites. Ophiolites represent sections of the oceanic lithosphere that have been obducted onto the continental crust, most frequently at destructive plate margins. The stratigraphic sequences observed in ophiolites (**Fig. 2**) correspond to sequences observed at mid-ocean ridges with the peridotite section at the bottom of the sequence. In contrast to abyssal peridotites, ophiolites allow for easy access to mantle lithologies and structure over a >3 billion year range of Earth's history. Ophiolite sequences also permit sampling of different rocks from the oceanic mantle, and provide an opportunity for field-based locations and observations to be paired with geochemical investigations. However, during the obduction process, ophiolite assemblages commonly undergo metamorphism and low-temperature alteration due to exhumation processes and seawater infiltration, respectively. Many ophiolites also record the effects of

supra-subduction zone (SSZ) processes, such as fluid-assisted melt extraction and metasomatism (Bu̇chl et al., 2002; Dilek & Furnes, 2011; O'Driscoll et al., 2012).

Here we report major and trace element data, including the abundances of the highly siderophile elements (HSE: here includes Os, Ir, Ru, Pt, Pd, and Re) as well as Os isotopic data, for peridotites and pyroxenites from two ophiolite complexes: the ~497 Ma Leka Ophiolite Complex (LOC), Norway and the ~1.95 Ga Jormua Ophiolite Complex (JOC), Finland; thought to sample the DMM associated with early Paleozoic (Iapetus) and Paleo-Proterozoic oceanic lithospheres, respectively. The primary focus of this study is to investigate chemical and isotopic heterogeneities in the mantle sections of these ophiolites at different length scales (kilometer-scale, meter-scale, and centimeter-scale) through grid sampling. Grid sampling methods allow for spatially controlled field-based observations of mantle samples to be linked with petrologic and geochemical studies. Heterogeneities within these mantle sections are key in assessing the chemical structure of these oceanic mantle sections, focusing on mantle history (partial-melting, melt-rock interactions) and subsequent processes that acted on these rocks. Additionally, comparison of these two ophiolites from different times, compared with data from more recent ophiolites, will enable monitoring of changes in the DMM through the latter half of Earth history.

1.2. Highly Siderophile Elements

Due to their general resistance to ophiolite modification processes, such as melt infiltration and fluid transport (Büchl et al., 2002), HSEs are useful tools for investigating upper mantle processes acting on peridotite samples. During mantle melting, the contrasting compatibilities of the highly compatible Os, Ir, and Ru (Ir-group platinum-group elements, or I-PGE), as compared to the slightly compatible to moderately incompatible Pt, Pd (Pt-group PGEs, or P-PGE), and Re make HSE particularly sensitive tracers of melt-depletion and melt-rock interactions (Allégre and Luck, 1980; Alard et al., 2000; Pearson et al., 2004; Rudnick and Walker, 2009). However, metasomatic processes tend to strongly affect the P-PGE and can even modify the relative and absolute abundances of the I-PGE (Lorand et al., 2013).

The utility of HSEs is enhanced by their association with the Re-Os ($^{187}Re \rightarrow {}^{187}Os + \beta^-$; $t_{1/2} \approx 41.6$ Ga) radiogenic isotope system (Walker et al., 1989). The difference between bulk partition coefficients of Re and Os forms the basis of the Re-Os chronometer. During partial melting of mantle peridotites, the moderately incompatible behavior of Re, but compatible behavior of Os, typically results in the formation of a melt with high Re/Os and a residue with low Re/Os, relative to the original mantle source. Residual rocks that have experienced significant melt removal, evolve to less radiogenic $^{187}Os/^{188}Os$, compared to mantle evolving along a chondritic growth trajectory typical of the bulk mantle. Based on this, minimum Re-depletion (T_{RD}) model ages can be calculated for refractory samples (Walker et al., 1989). These model ages are made with the assumption that all Re originally present in the sample was removed at the time of initial melting. T_{RD} model ages were previously defined in an attempt to overcome the problem of excess Re in peridotitic mantle xenoliths caused by infiltration of Re enriched host magmas. Rhenium addition at

the time of xenolith capture, often causes Re-Os mantle model ages (T_{MA}; (Allégre and Luck, 1980); analogous to Sm-Nd T_{CHUR} and T_{DM} model age calculations (DePaolo and Wasserburg, 1976)) to overestimate the time of melt depletion. To account for Re contamination during eruption, the Os isotopic compositions of the sample and chondritic reference in the T_{RD} equation (Walker et al., 1989), are calculated back to the emplacement age of the xenolith host. Afterwards, the T_{RD} calculation is performed.

At high degrees of melt extraction, the Re concentrations of melt residues will approach zero, resulting in $T_{RD} = T_{MA}$. When melt extraction is less extreme, and leaves the residual mantle peridotites with a non-negligible concentration of Re, or if Re was introduced to the sample long prior to transport to the surface, T_{RD} model ages will be less than T_{MA}, and underestimate the timing of melt depletion in the sample (Carlson and Moore, 2004; Carlson, 2005).

Eq. 1. $$T_{RD} = 1/\lambda \times \ln \left[\frac{^{187}Os/^{188}Os_{chond} - {}^{187}Os/^{188}Os_{sample(EA)}}{^{187}Re/^{188}Os_{chond}} + 1 \right]$$

Rhenium-depletion models ages can be applied to mantle peridotites using the equation above (**Eq. 1**) with the eruption age (EA) representing the $^{187}Os/^{188}Os$ ratio of the sample, at the time of the accepted age of the ophiolite (LOC ~497 Ma; JOC ~ 1.95 Ga). The Os isotopic composition of the samples is then matched to a chondritic mantle reference value (Shirey & Walker, 1998).

T_{RD} model ages are resistant to high-temperature, open-system behaviors because the system is based on the removal of the parent isotope Re, rather than the ingrowth of the radiogenic daughter Os. These ages can be interpreted as the minimum estimate for the true melt depletion age for a sample, and can be useful for constraining the timing of initial melting events in small portions of the mantle (Rudnick & Walker, 2009).

2. SAMPLES

2.1. Regional geology

2.1.1. Leka

The National Geological Monument of Norway, the Leka Ophiolite Complex (LOC), located on the island of Leka (Dahl et al., 2011; ~90 km^2), Nord Trøndelag, at ~65ºN (**Fig. 3**), is a well-preserved, well-exposed section of early Paleozoic (Iapetus) oceanic lithosphere. The LOC is one of the most completely preserved ophiolites in the Scandinavian Caledonides (Prestvik, 1972) and contains all of the principle components of

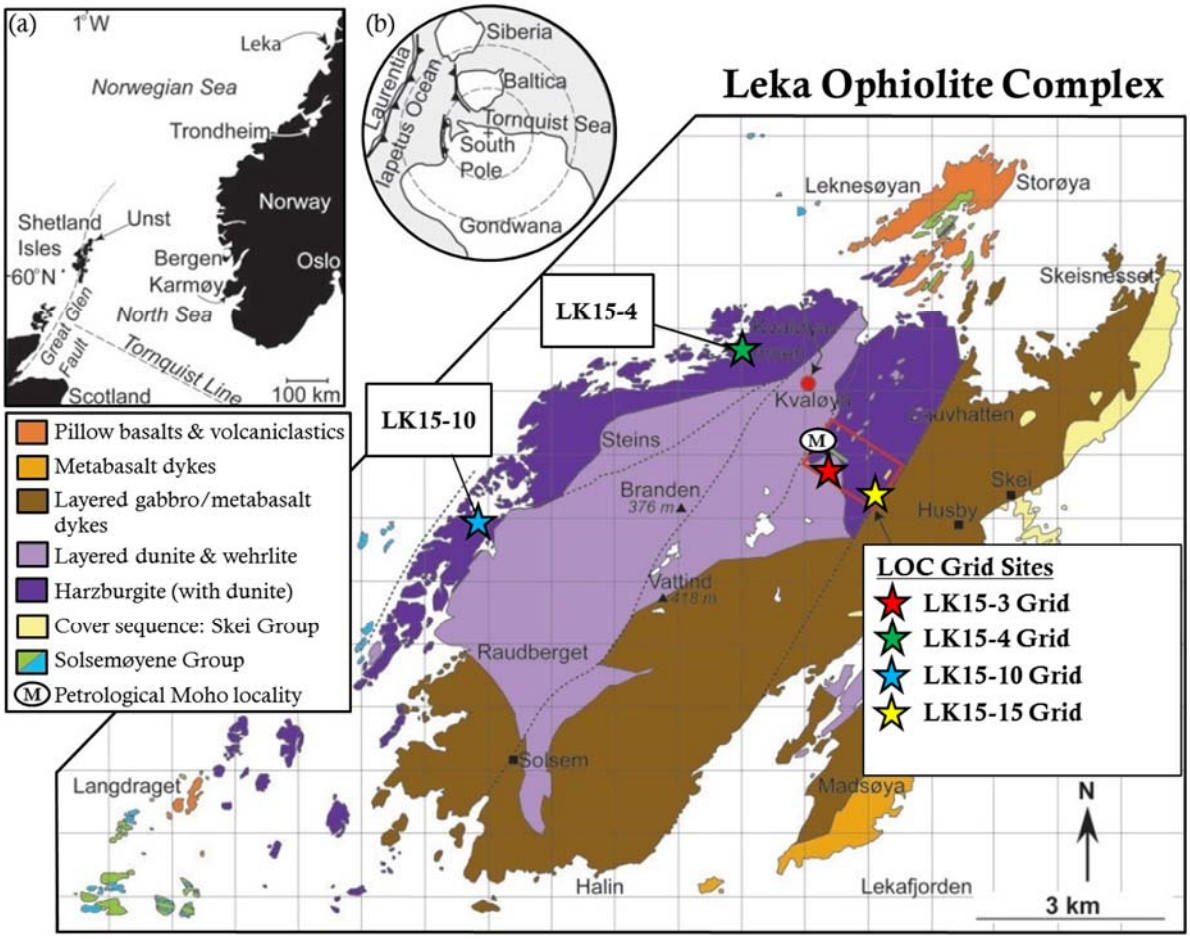

Figure 3. Sketch map illustrating the regional (geographical) and tectonic setting for the Leka Ophiolite Complex. The harzburgite unit (with dunite) comprises the mantle section. The layered dunite and wehrlite is the lower crustal layered series, or dunite transition zone. The dashed lines in the main panel represent faulted contacts. Stars represent approximate areas of grid sampling in the lower crustal Kvaløya section and the mantle section at Kvaløya-moen (adapted from O'Driscoll et al., 2015).

a classic *Penrose* ophiolite sequence (**Fig. 2**). These units are present within various blocks separated by faults.

The depleted upper mantle complex of the LOC was dubbed 'mantle tectonite' by Furnes et al. (1988). The unit is comprised of harzburgite with minor dunite and crops out over the entire northwestern part of the island, becoming progressively richer in dunite eastward where it begins to transition into the lower crustal 'layered series' (Furnes et al., 1988) of dunite and wehrlite. The petrological Moho is exposed ~2 km west of Lauvhatten (**Fig. 3**) and is defined here as the boundary between the mantle and lower crust, or the base of the Moho transition zone. The upper mantle section manifests dunite in the form of lenses and sheets that are typically oriented parallel to the Moho, and are described in detail by Maaløe (2005). The sequence contains numerous podiform chromitite (≥60% Cr-spinel by volume; O'Driscoll et al., 2015), as well as layers of pyroxene-rich rocks. Websterite and reddish-weathered orthopyroxenite have also been found as pods, lenses, and as meter-thick channels to centimeter-thick veins in both dunite and harzburgite.

Layered gabbros are featured in the southern part of the island and form a tectonic contact with the harzburgite upper mantle complex near Lauvhatten. The LOC gabbro sequences were described in detail by Furnes et al., (1988). Gabbros in the sequence are layered on three scales (>100 m, 10-50 m, and 30-10 cm) with ultramafic units as well as cyclic units of dunite-wehrlite-gabbro. Furnes et al., (1988) described the clinopyroxene and olivine of the gabbros as totally altered to uralitic amphibole and serpentine, respectively. The plagioclase is saussuritized. Despite the heavy alteration, the gabbroic texture is still preserved (Furnes et al., 1988). Upwards in the sequence the layering grades into a finely laminated and vari-textured metagabbro apparent near Madsøya (**Fig. 3**).

Metabasaltic dikes, interlayered with the dunite/wehrlite are located in the southwest and first appear in the upper part of the laminated/vari-textured variety of metagabbro sequence (Furnes et al., 1992). The metabasaltic dikes were described by Furnes et al., (1992) as irregular and become more consistent in form and trend higher in the stratigraphy. The dike length is typically in the tens of meters, while thickness varies from a few centimeters to over 10 m (Furnes et al., 1988). Metabasaltic dike and layered gabbro sequences both feature minor intrusions of quartz-keratophyre and plagiogranite ranging from (millimeter thick) veins to bodies >100m in diameter (Furnes et al., 1988).

Pillow basalts and volcaniclastics crop out at three localities within the LOC; Madsøya, Langdraget, and on the nearby island of Storøya off the northern coast. While their separation prohibits the observation of their stratigraphic relations, Furnes et al. (1988) suggested that the time sequences for the lavas (from oldest to youngest) are Madsøya, Langdraget, Storøya.

The time of formation for the mafic and ultramafic complexes of the LOC is constrained to 497±2 Ma, from U-Pb dating of zircons in associated trondhjemite (Dunning and Pedersen, 1998), while obduction likely occurred during the Taconic-Grampian orogeny (~470 Ma; Titus et al., 2002). The mantle rocks of the LOC are thought to reflect multiple stages of melt depletion, melt migration, and metasomatic processes that acted upon the oceanic mantle through time, with a final fluid-assisted melt extraction in a supra-subduction zone (SSZ) setting prior to obduction (Furnes et al., 1988, 1992).

2.1.2. Jormua

The Jormua ophiolite complex (JOC) is a well-preserved section of early-Proterozoic oceanic lithosphere located in the northernmost section of a chain of ophiolitic rocks found in northeastern Finland (Tsuru et al., 2000; ~20 x 40 km^2 area). The JOC also contains all of the major components of a *Penrose*-definition ophiolite: (1) tectonite peridotites; (2) cumulate gabbros; (3) a sheeted dyke complex; (4) a unit of massive and pillow lavas. However, all portions are partially dismembered. Detailed petrological descriptions of each rock type are provided in Kontinen (1987) and Peltonen et al. (1996; 1998). The peridotitic mantle section of the JOC has been previously described as heavily serpentinized and metamorphosed, with no primary minerals preserved, with the exception of some partly recrystallized chromite grains (Peltonen et al., 1996).

The JOC is bordered by Archean craton on the east, a Proterozoic Svecofennian island arc collage to the west (2.1 to 1.9 Ga), with a narrow sliver of Archean craton between the JOC and Sveconfennides (Peltonen et al., 1996). U-Pb dating of zircons from an associated gabbroic dike suggest the age of JOC continental rifting within an Archean craton to be constrained to 1953±2 Ma (Peltonen et al., 1996). The JOC was later obducted and emplaced into the current location during collision between the Archean craton and the Svecofennian island arc, ~50 Ma after rifting initiation (Peltonen et al., 1998).

The Jormua complex is divided into three tectonic blocks largely composed of serpentinite (20 × 40 km^2 area) termed the Antinmäki, Hannustranta, and Lehmivaara blocks (Tsuru et al., 2000) (**Fig. 4**). Peltonen et al., (1996; 1998) suggested that the three tectonic blocks of the JOC form a composite body representing portions of a tectonic setting related to continental break-up. The eastern Antinmäki block represents Early

Proterozoic oceanic lithosphere and resembles a typical ophiolite, with enriched (E)-MORB sheeted dikes, gabbros, pillow lavas, mantle harzburgites/serpentinites, and tectonites with podiform chromitites. The western Hannustranta block represents ancient subcontinental lithospheric mantle (SCLM), absent of oceanic crustal rocks, and instead features mantle tectonics and serpentinites extensively veined by a suite of alkaline (hornblendite-garnetite-carbonatite veins and clinopyroxene cumulate) dikes. Zircon dating of the clinopyroxene cumulate dikes that intrude the western Hannusranta

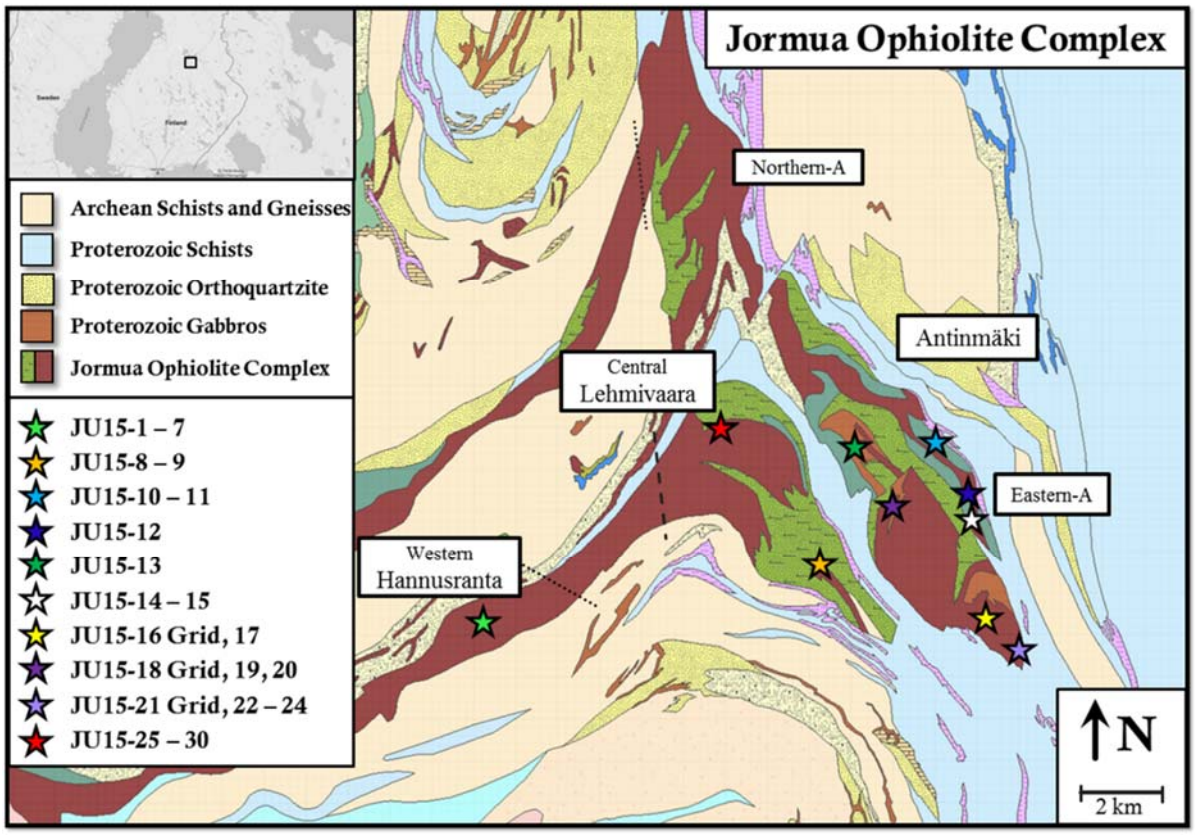

Figure 4. Geologic map of the Jormua Ophiolite Complex. (JOC). The JOC is divided into three tectonic blocks: The easternmost Antinmäki block is commonly associated with the occurrence of crustal units and is divided into the northern and eastern sections (Peltonen et al., 1998). The two slivers that extending to the southwest are the divided into the central Lehmivaara block and the western Hamusranta block (Tsuru et al., 2000). The bold dashed line indicates the approximate location of the tectonic boundary between the Archean craton and the Proterozoic Svecofennian arc complex (Peltonen et al., 1998). The two dotted lines indicate the divides between the three blocks (Tsuru et al., 2000). Stars represent approximate areas of grid and random sampling in the respective blocks (Map adapted from Geological Survey of Finland).

peridotites yield $^{207}Pb/^{206}Pb$ ages between 3106±3 and 2718±12 Ma and suggest that most of JOC subcontinental mantle peridotites are Archean (Peltonen et al., 2003). The Lehmivaara block is thought to represent a transition between these two types of lithosphere (Peltonen et al., 1996), and is largely comprised of serpentinite. Because of its age and exposed mantle section, data for the JOC may shed light on the secular evolution of the upper mantle and ophiolite forming processes over the past two billion years.

2.2. Sample method and descriptions

The ultramafic samples studied here (**Fig. 5**) were selected from more than 100 rocks collected during July, 2015. The aims of the sampling campaign for this study at both the LOC and JOC were twofold: to assess kilometer scale heterogeneity through sampling of different portions of the upper mantle, as well as to investigate small-scale (e.g., meter scale) chemical and isotopic heterogeneities. To assess small-scale heterogeneities, grid sampling, a technique new to these complexes, was conducted at four locations in the LOC (**Fig. 3**), and three locations in the Antinmäki block in the JOC (**Fig. 4**). Grid sizes were 3 m x 3 m for the LOC (**Fig. 6**) and one location for the JOC. Two grid locations in the JOC were 1.5 m x 1.5 m. The JOC grids were limited in size due to limited outcrop exposure. Grids were divided into nine 0.5 - 1 m^2 squares and one sample per lithology was taken, if possible, from the center of each square.

Most LOC samples were collected in the northern harzburgite mantle section containing abundant dunite pods and channels, as well as from just below the petrological Moho, ~2 km west of Lauvhatten (**Fig. 3, 6A**). Some LOC mantle peridotites also hosted pyroxenite in the form of centimeter-thick veins to meter-thick dikes, and included orthopyroxenites and websterites. Pyroxenite veins usually strike parallel to each other and to the layering **(Fig. 6C**), but it's not uncommon to observe them cross cutting each other. The predominant lithologies for LOC grid sampling were harzburgite, followed by dunite and pyroxenite (**Fig. 6E**), while lithologies for JOC grid sampling were mostly serpentinite/ harzburgite (**Fig. 6F**). In addition, random sampling of the mantle was conducted around the grid locations, as well as in the central Lehmivaara and western Hannusranta blocks of the JOC. Minor sampling of the other ophiolite components was conducted as well at both

complexes. GPS data for all samples and field descriptions are provided in the supplementary tables.

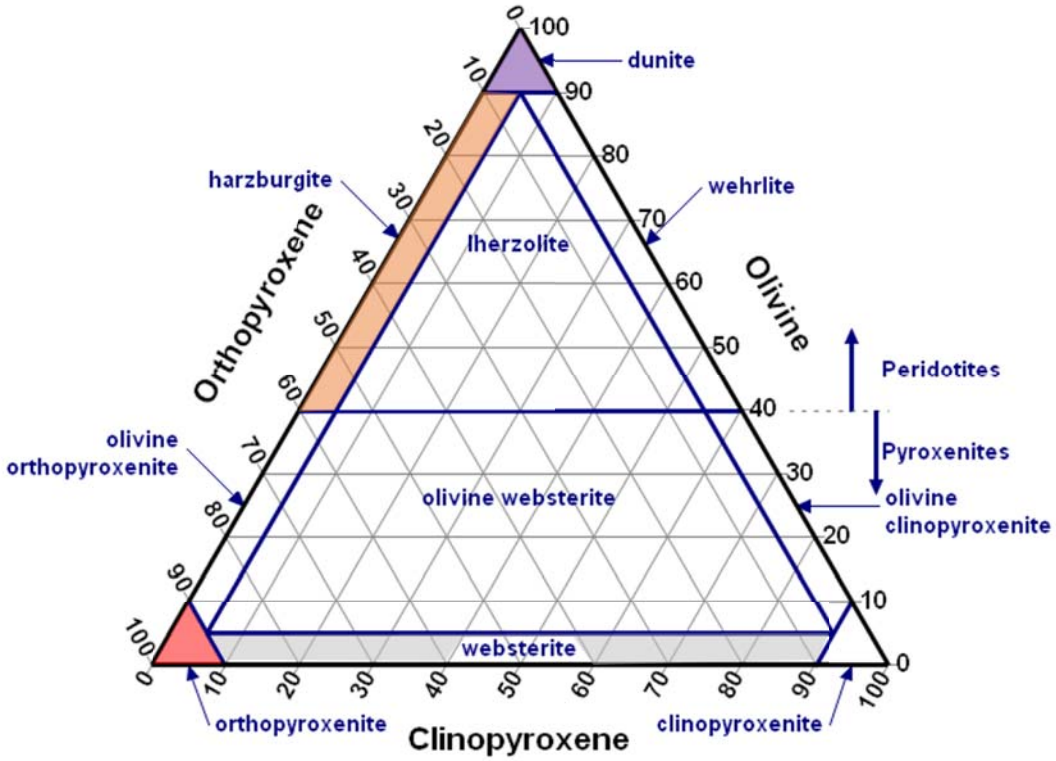

Figure 5. Ternary plot displaying the petrological definition of ultramafic rocks examined in this study (from Winter, 2010). Highlighted areas indicate lithologies observed in this study.

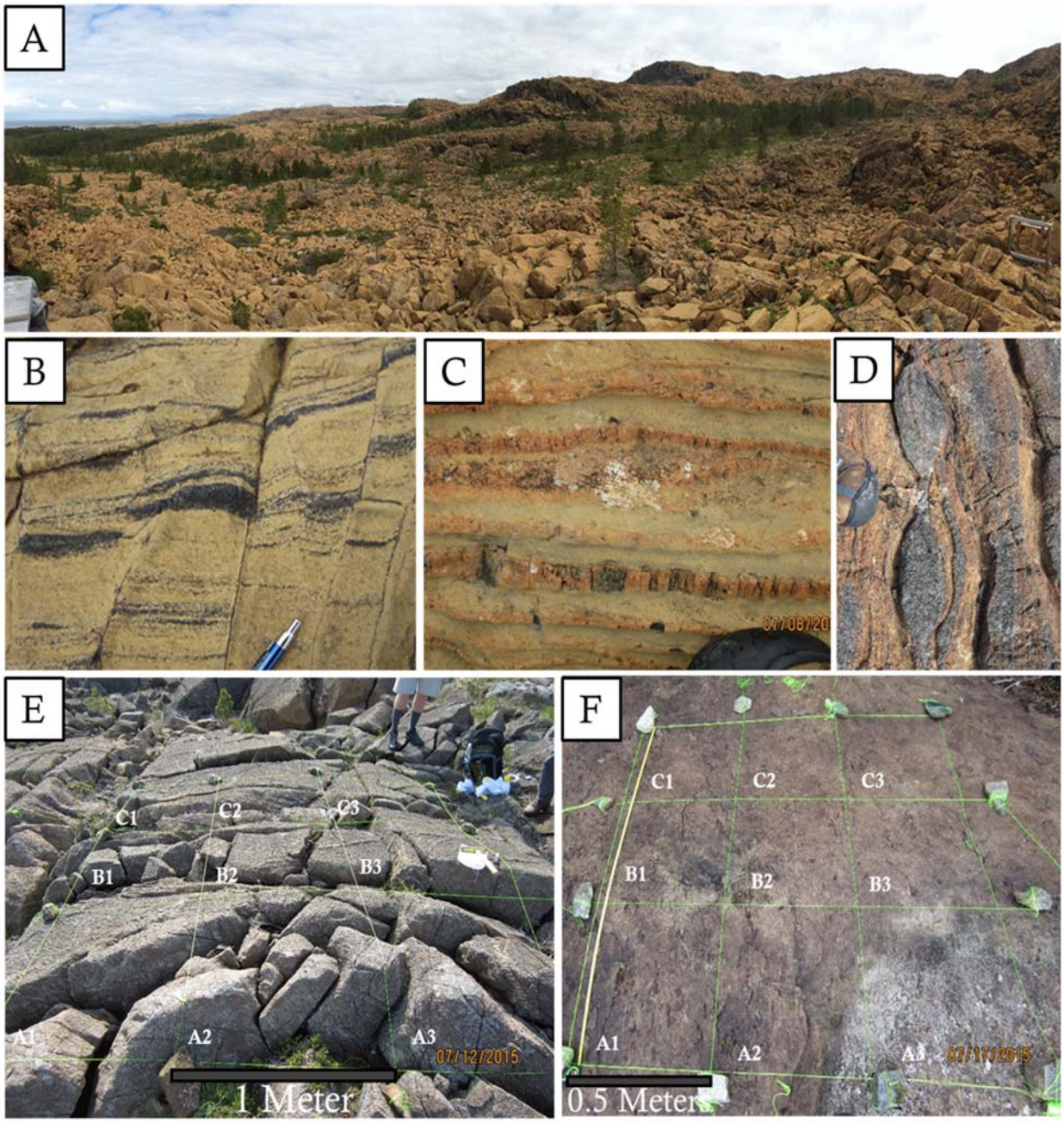

Figure 6. Field Photographs of LOC and JOC mantle and lower crustal lithologies. **A**. Photo taken at the petrological Moho displaying the excellent exposure of the LOC mantle section. Picnic table/viewing area marking the Moho is seen on the far left. **B**. Multiple chromitite seams (black) in dunite running horizontal with multiple vertical faults. Pen for scale. **C**. Multiple weathered orthopyroxenite seams in dunite. Top of boot for scale. **D**. Layered harzburgite-wherlite, the structure of the wherlite resembles partial boudinage. Top of boot for scale. **E**. Example of grid sampling method for LOC LK15-15 harzburgite grid shown in **Fig. 3** by a yellow star. Grid dimensions are 3 m x 3 m and divided into 9 x 1 m^2 grid squares. **F**. Example of grid sampling method for JOC JU15-18 harzburgite/ serpentinite grid shown in **Fig. 4** by a purple star. Grid dimension are 1.5 m x 1.5 m due to exposure limitations. Drill cores were taken from each JOC grid square.

2.2.1. Leka grids

The two LOC grids examined in detail by this study are LK15-4 and LK15-10 from the northern harzburgite mantle section of Leka. They are shown in **Fig. 3** by green and blue stars, respectively. The LK15-4 grid location (**Fig. 7A**) is a 3 m x 3 m square located in Kvaløya-moen and samples 7 harzburgites, 1 harzburgite hosting a ~1 cm orthopyroxenite

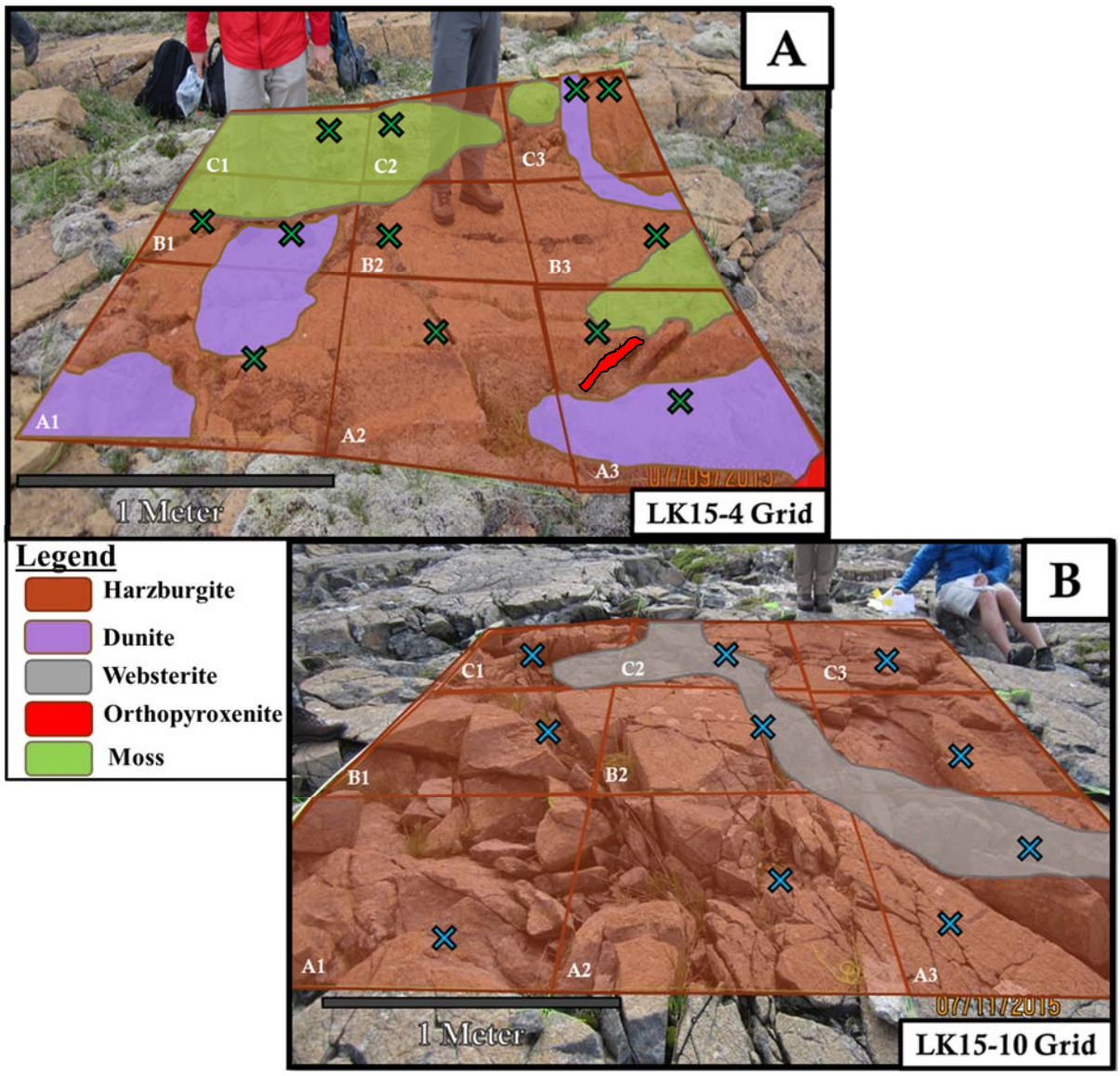

Figure 7. (left) 3 m x 3 m LOC grids located in the harzburgite mantle section in northern Leka, Norway. Grids are divided into 9 1 m^2 grid squares. **LK15-4** (**A**) and **LK15-10** (**B**) are shown in **Fig. 3** by the **green** and **blue** stars respectively. Colored Xs indicate approximate sample locations within each labeled grid square.

vein (LK15-4 A3 Harz), 3 dunites, and 1 harzburgite/dunite contact (LK15-4 C3 Dun/Harz). The LK15-10 grid location (**Fig. 7B**) is a 3 m x 3 m square located west of Steins, approximately 6 km southwest of LK15-4 in Kvaløya-moen. The LK15-10 grid samples are predominately harzburgite (n = 9), but 1 sample from a ~0.5 m websterite channel running diagonally through the grid space is also examined.

Samples from grid LK15-3 are also partially examined in this study. Grid LK15-3 is located in the harzburgite mantle section of Leka near the petrological Moho, and is shown in Fig. 3 by the red star. The LK15-3 grid location (Fig. 7C) is a 3 m x 3 m square and samples 9 harzburgites and one ~0.5 m orthopyroxenite channel, adjacent to the grid.

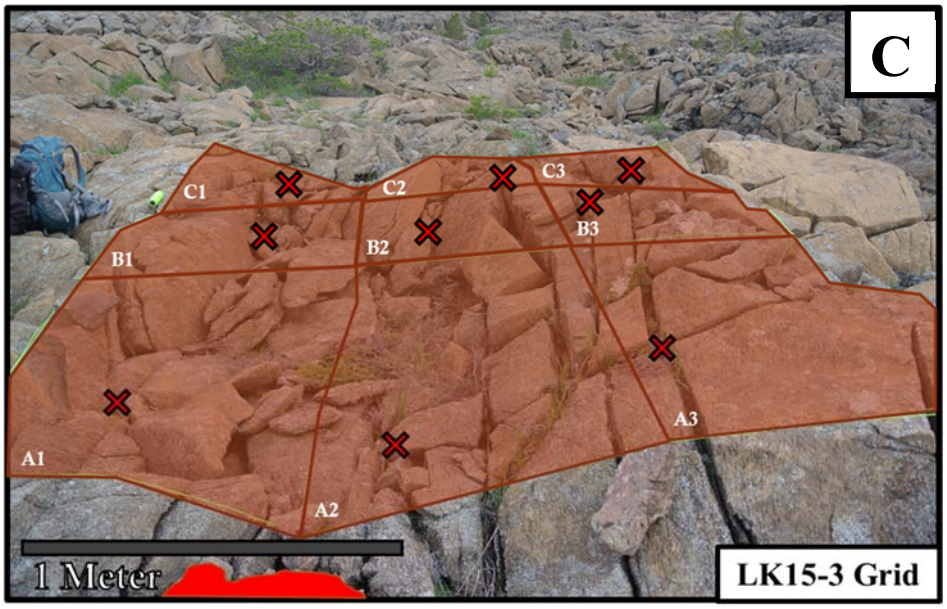

Figure 7C. (right) 3 m x 3 m LOC grids located in the harzburgite mantle section in northern Leka, Norway. Grids are divided into 9 1 m^2 grid squares. **LK15-3 (C)** is shown in **Fig. 3** by the **red** star Colored Xs indicate approximate sample locations within each labeled grid square.

2.2.2. LOC orthopyroxenite subdivision

To investigate the role of pyroxenites in inducing large isotopic changes at a small scale in peridotites (Borghini et al., 2011; Rampone et al., 2011; Rampone & Hofmann, 2012), 2 harzburgites hosting >1 cm orthopyroxenite veins were sampled from grid location LK15-4 and at location LK15-9, both located in the LOC harzburgite mantle section at Kvaløya-moen (**Fig. 3**). Each harzburgite sample was sub-divided into 1 cm slabs parallel to the hosted orthopyroxenite vein (**Fig. 8**). Each sub-division was later processed and analyzed separately to study the effects of orthopyroxenite vein formation on their host harzburgites, at the cm-scale.

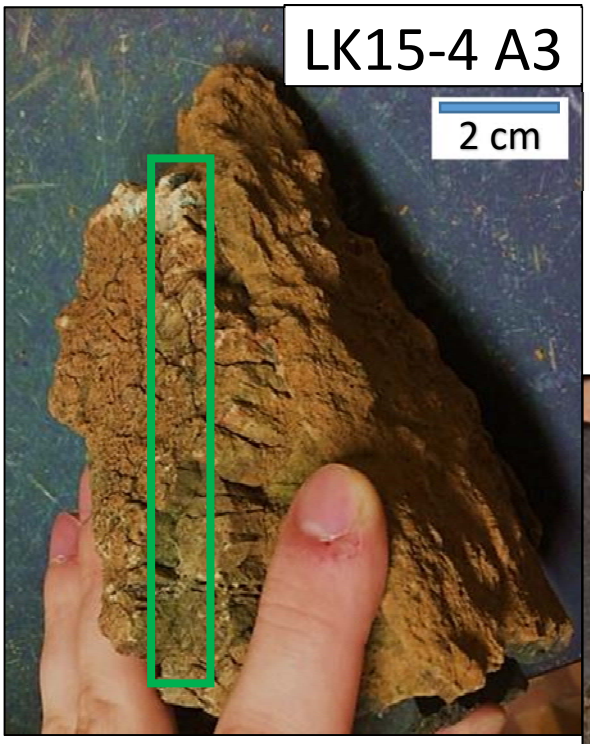

Figure 8. Sample photos of LOC orthopyroxenite bearing harzburgites from the harzburgite mantle section at Kvaløya-moen. Colored boxes indicate the approximate location of the orthopyroxenite vein.

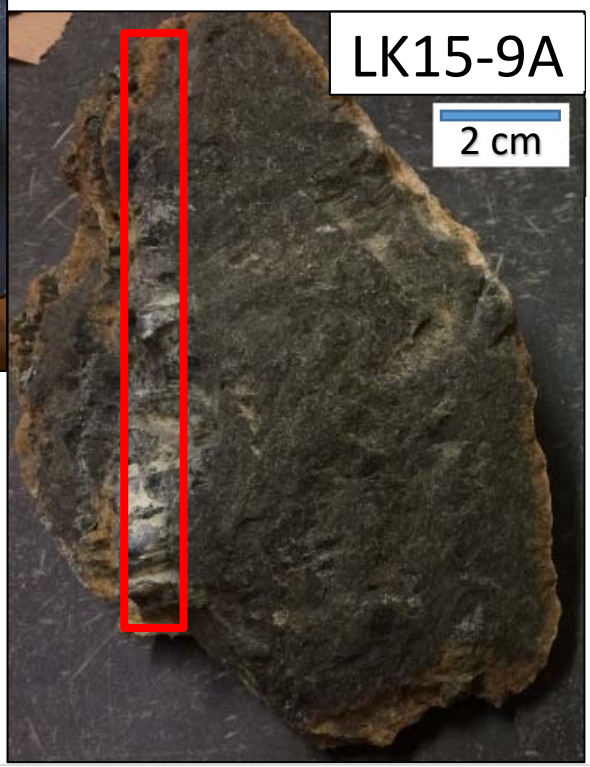

2.2.3. Jormua grids

The two JOC grids examined in detail by this study are JU15-16 and JU15-18 from the Antinmäki block. Their locations are shown in Fig. 4 by yellow and dark purple stars, respectively. The JU15-16 grid location (**Fig. 9A**) is a 3 m x 3 m square sampling 9 harzburgites drill cores. The JU15-18 grid location (**Fig. 9B**) is a 1.5 m x 1.5 m square located ~3 km northwest of JU15-16, and also samples 9 harzburgite drill cores. Additionally, the JU15-18 grid squares hosts a chromite seam that is sampled in grid square B2.

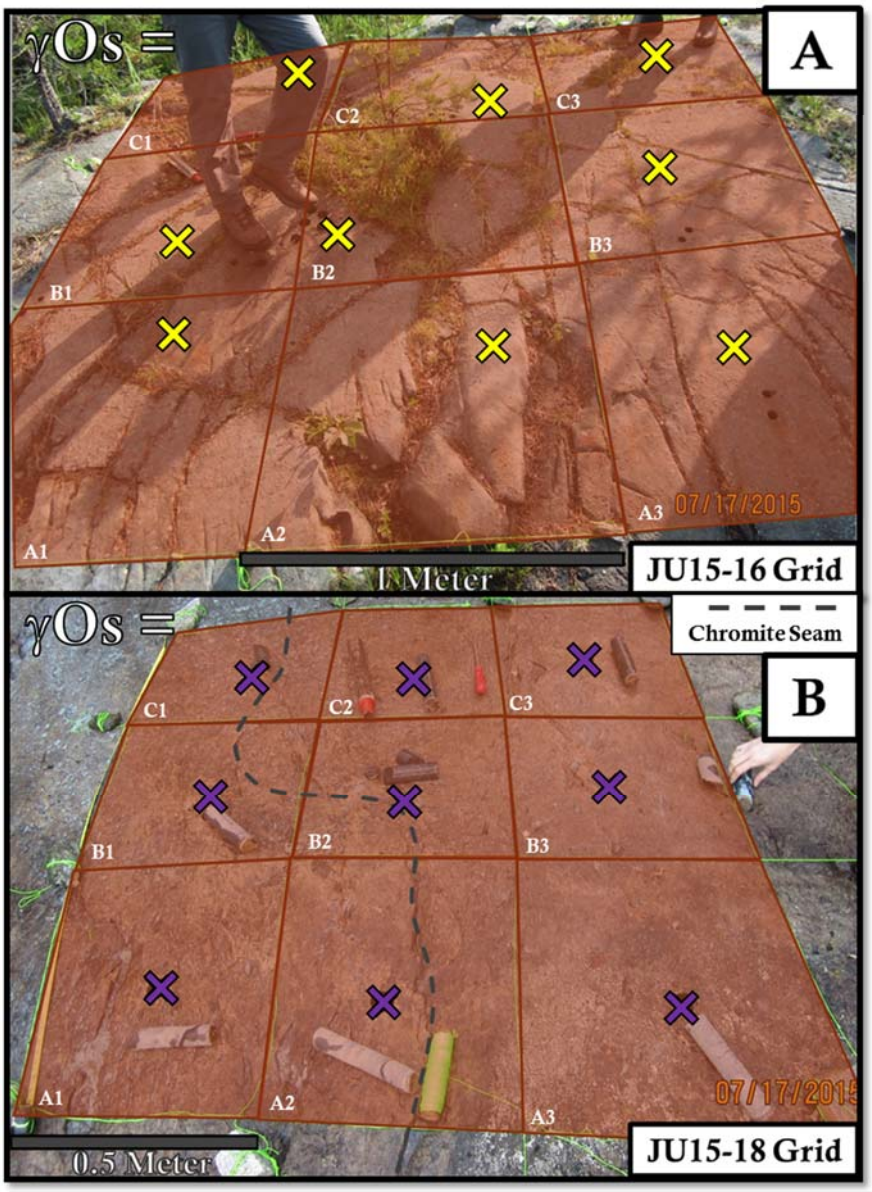

Figure 9. 3 m x 3 m and 1.5 m x 1.5 m JOC grids located in the eastern Antinmäki block near Kajaani, Finland. Grids are divided into 9 0.5-1 m^2 grid squares. **JU15-16** (**A**) and **JU15-18** (**B**) are shown in **Fig. 4** by the **yellow** and **purple** stars respectively. Colored Xs indicate approximate sample locations within each labeled grid square.

3. Analytical methods

3.1. *Sample preparation*

Samples were cut using a rock saw with a diamond studded blade and water as lubricant, in order to remove weathered surfaces. Rock billets were cut during this process for thin sections as well. Sawn surfaces were sanded using 120 grit sandpaper in order to remove contaminants introduced during cutting. Sanded rock slabs were then processed into cm-sized chips using a ceramic jaw crusher.

The chips were powdered, ~30 g at a time, using a ceramic swing mill shatterbox, and ground more finely using a ceramic disk mill, reducing the grain size to ~10 microns. Both powdering devices were cleaned with quartz sand and rinsed with distilled water prior to the processing of each sample to reduce previous contaminants. The overall weight of each sample processed was around 90 grams in order to ensure a representative sampling of the rock, with ~1.5 g of powder used for each analysis. Because HSE in terrestrial rocks are often hosted in trace phases, including sulfides and alloys, rather than major silicates, HSE can be heterogeneously distributed within a sample. This "nugget-effect" can lead to poor measurement reproducibility with smaller sample sizes (Meisel et al., 2001).

3.2. Major and trace element analysis

Whole-rock major element concentrations were obtained by X-ray fluorescence (XRF) analysis using a *PANalytical 2404* X-ray fluorescence vacuum spectrometer at Franklin and Marshall College, Lancaster, PA, following methods outlined in Boyd and Mertzman (1987) and Metzman (2000). Samples were heated to determine loss on ignition (LOI) prior to the rock powder being mixed with lithium tetraborate ($Li_2B_4O_7$), placed in a platinum crucible and heated with a Meker burner until molten. The molten material was transferred to a platinum casting dish and quenched. This procedure produces a glass disk that is used for XRF analysis. Typical accuracy of the analyses was ~1% for major elements for concentrations >0.5%. Major and minor elements in concentrations <0.5% had an accuracy of ~5%. Working curves for each element were determined by analyzing geochemical rock standards outlined in Abbey (1983), Govindaraju (1994), and Mertzman (2000). The compositions of Fe^{3+} and Fe^{2+} were calculated from the total measured FeO based on stoichiometry (Droop, 1987). Reproducibility (2σ) of major elements, based on recent repeated analyses of samples were: 1.32% for SiO_2, 1.80% for Al_2O_3, 0.87% for Fe_2O_{3T}, 0.96% for MgO, 0.10% for CaO.

Whole-rock trace element abundances were measured at Scripps Institution of Oceanography (SIO) using methods outlined in Day et al., (2014) and O'Driscoll et al., (2015). Samples were analyzed together with peridotite and basalt rock standards (BHVO-2, BCR-2, BIR-1a, HARZ-01), as well as total-procedural blanks. In brief, 100 mg sample powders were digested in a 1:4 mixture of concentrated Optima-grade HNO3:HF for >72 h at 150ºC on a hotplate. After drying down and sequential HNO_3 dry downs to break down fluorides, clear sample solutions were diluted by a factor of 5000 in 2% HNO_3 and doped

with a 1 ppb In solution, in order to monitor instrumental drift. Due to the low rare earth element (REE) abundances in some peridotites in the LOC, a concentrated solution diluted by a factor of 1000 was measured specifically for the REE. Sample and standard solutions were measured in standard mode on a Thermo Scientific iCAP Qc quadrupole inductively coupled plasma mass spectrometry (ICP-MS) system at SIO. Reproducibility (2σ) of laboratory standards was generally ~2-4%.

3.3. Electron microprobe analysis

30 micron thick thin sections were made and selected relict olivines, where present, (n=5 per section, 2 points per grain) were analyzed using the *JXA-8900 SuperProbe* electron probe microanalyzer (EPMA), at the University of Maryland, for major/minor element data for LOC peridotites. Operating conditions for olivine analysis were as follows: accelerating voltage of 15 kV, beam current of 50 nA, 10 μm beam diameter, peak/background times for Ni, Cr, Ca, Fe of 30.5 seconds and for Ti, Mn, Al, Mg, and Si of 20.5 seconds.

The primary standards used for olivine analyses were as follows: San Carlos Olivine (Fe, Mg, Si, and Ni), Bushveld Chromite (Cr), Illmenite (Mn), and Kakanui Hornblende (Ca, Al, and Si). Statistical uncertainties (2σ), due to counting statistics were 1.5% for FeO, 0.5% for MgO, 23% for MnO, 13% for NiO, 0.7% for SiO_2. Concentrations for CaO, TiO_2, Cr_2O_3, and Al_2O_3 were generally below detection limits. Peridotites from the JOC contain no relict olivines, due to serpentinization.

3.4. Re-Os isotopic and HSE analysis

Chemical separation of Os and the other HSE was conducted at the Isotope Geochemistry Laboratory (IGL), University of Maryland, College Park, MD (USA), using methods outlined in Becker et al., (2006) and O'Driscoll et al., (2015). Between 0.75-1.5 g of whole rock powder, 5 mL of 2x Os-purged conc. HNO_3 1x Quartz Distilled (QD) 1 x Teflon Distilled (TD), 4mL conc. HCl 1xQD 1xTD, and appropriate amounts of mixed ^{185}Re-^{190}Os and ^{99}Ru, ^{105}Pd, ^{191}Ir, and ^{194}Pt spikes were sealed in double internally-cleaned 25 mL PyrexTM borosilicate glass Carius tubes (Shirey and Walker, 1995). Sealed tubes were heated to ~265°C for >72 h. After digestion, Os was extracted from the acid solution using CCl_4 solvent extraction and back-extracted into HBr (Cohen and Waters, 1996). Osmium was then purified via micro-distillation technique (Birck et al., 1997). Rhenium, Ru, Ir, Pt, and Pd were sequentially separated and purified using anion exchange chromatography using pre-cleaned AG 1x8 (100-200 mesh) anion exchange resin, following a modified protocol of Rehkämper & Halliday (1997). Average total procedural blanks (n=7) were (in pg) 1.4±0.7 Os, 4.5±4.2 Re, 13.2±7.6 Ru, 0.2±0.1 Ir, 225±77 Pt, and 4.3±3.2 Pd. Total analytical blank (TAB) for dunites and harzburgite constituted less than 0.1% for Os, <1.0-64.0% for Re (average ~10%), <1.0 % for Ru, <0.1% for Ir, <12.5% for Pt, and <1.0% for Pd of the total element analyzed. High blank contributions for Re of as much as 64% is due to the very low concentrations of Re in some LOC and JOC peridotite samples. While modified cleaning techniques for borosilicate Carius tubes (Puchtel et al., 2008) were used to lower blanks for Pt, high-Pt blank contributions is likely from contributions from the tubes during sample digestion.

Purified Os was analyzed by negative thermal ionization mass spectrometry (N-TIMS) using an electron multiplier (SEM) detector of a *ThermoFisher Triton*® mass spectrometer at the IGL, University of Maryland. External precision for $^{187}Os/^{188}Os$ for measurements of 0.35-0.7 ng loads of UMCP Johnson-Matthey Os laboratory standard, using electron multiplier, was ±0.05% (0.11373±6; n=15, 2σ). Rhenium, Pd, Pt, Ir, and Ru concentrations were determined using a Nu Plasma MC-ICP-MS, in a static mode using faraday cups or ion-counter detectors. Isotopic mass-fractionation was monitored and corrected for by alternating samples and standards. Internal precision (2σ) for isotope ratios of standards was better than ±2% for Re, Ir, Pt, Pd and Ru. Reproducibility (2σ) for Os concentration and $^{187}Os/^{188}Os$ isotopic composition via TIMS, was 38 to 56% and to 0.25 to 0.41%, respectively. Reproducibility (2σ) for HSE concentrations using MC-ICP-MS, based on repeat analyses of 4 samples were: 3.3 to 66% for Re, 3.6 to 70% for Ru, 2.1 to 18% for Ir, 4.4 to 77% for Pt, and 1.0 to 83% for Pd. The poor reproducibility for HSE concentrations is most likely due to the heterogeneous distribution of the HSE hosted in sulfides in the peridotite samples, termed "the nugget effect" (Meisel et al., 2001), coupled with incomplete homogenization of processed sample powders.

4. Results

4.1. Major elements

4.1.1. Leka peridotites and pyroxenites

Major element data for LOC samples are presented in **Table 1**. The LOC harzburgites and dunites have compositions that are similar to previously published data on LOC peridotites (e.g., Maaløe, 2005; O'Driscoll et al., 2015). The compositions of the peridotites are also similar to other lapetus oceanic mantle peridotites from the ~492 Ma Shetland Ophiolite Complex (SOC, O'Driscoll et al., 2012), and plot within a compositional range common to abyssal peridotites, and peridotites associated with other ophiolites (**Fig. 10A and B**). The LOI for the LOC samples is between 3.5 and 11.8 wt %; while averaged LOI of peridotites from grid location LK15-4 (10.2 wt %), is higher than averaged LOI of peridotites from the LK15-10 grid (8.3 wt %), ~6 km away (**Fig. 3**). Whole-rock (WR) concentrations of Al_2O_3 (anhydrous corrected, wt %) range between 0.2 and 1.6 wt % for all LOC samples. WR concentrations of LOC harzburgites show general negative correlations of Al_2O_3 and SiO_2 with MgO (**Fig. 10A and B**). Lower Al_2O_3 and higher MgO concentrations observed in LOC peridotites, relative to primitive mantle (PM) estimates (McDonough & Sun, 1995), are broadly consistent with prior melt depletion (**Fig. 10A**). Averaged Mg# ((Mg/(Mg+Fe))*100) of grids LK15-4 and LK15-10 are 91.3 and 91.7, respectively.

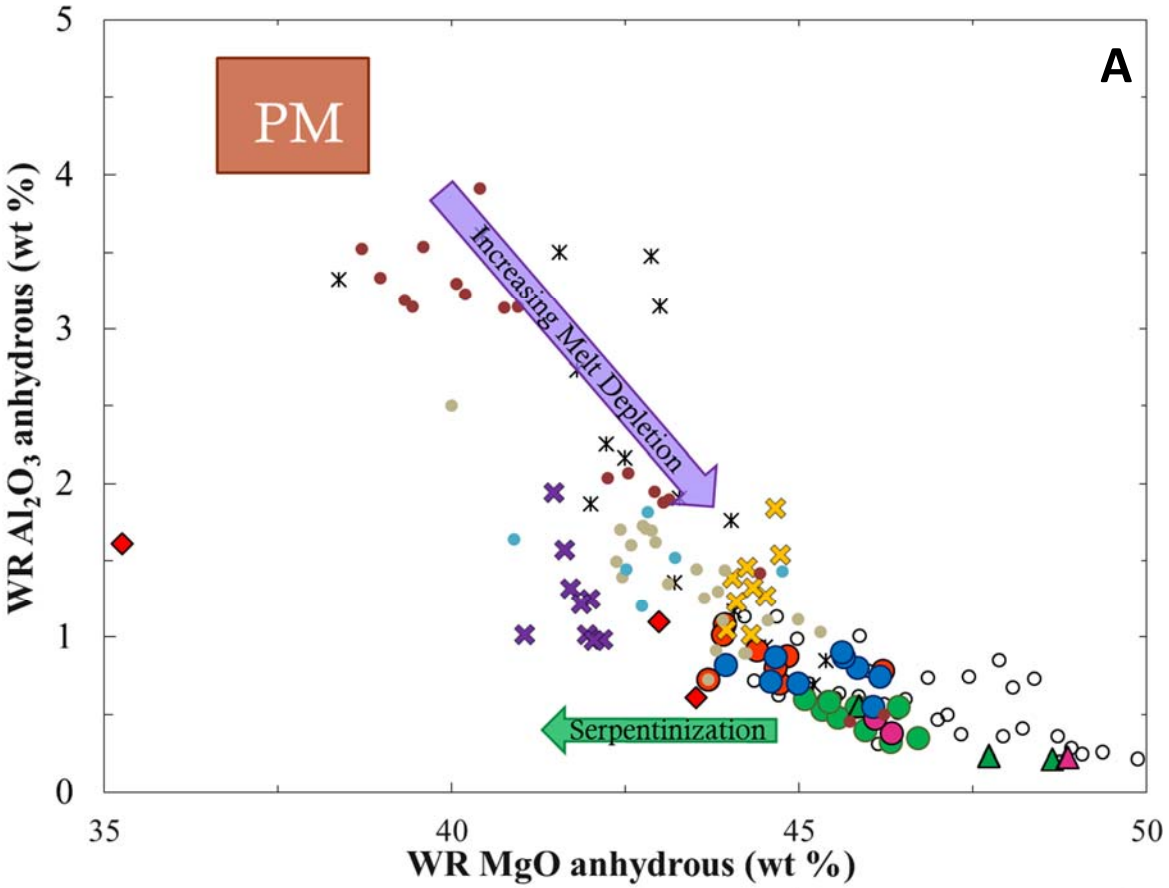

Figure 10. Plots of whole-rock XRF major element data; **A**. Al_2O_3 vs MgO **B**. SiO_2 vs MgO (all values plotted wt % anhydrous). Shown for comparison are whole rock data for Leka peridotites (O'Driscoll et al., 2015), Jormua serpentinites (Peltonen et al., 1998), Horoman peridotites (Saal et al., 2000), peridotites from the Taitao ophiolite (Schulte et al., 2009), abyssal peridotites (Brandon et al., 2000), and Primitive Mantle (**PM**) estimates (McDonough and Sun, 1995). Shown in **A** are general trends for the effects of peridotite melt depletion (**purple**) and serpentinization (**green**).

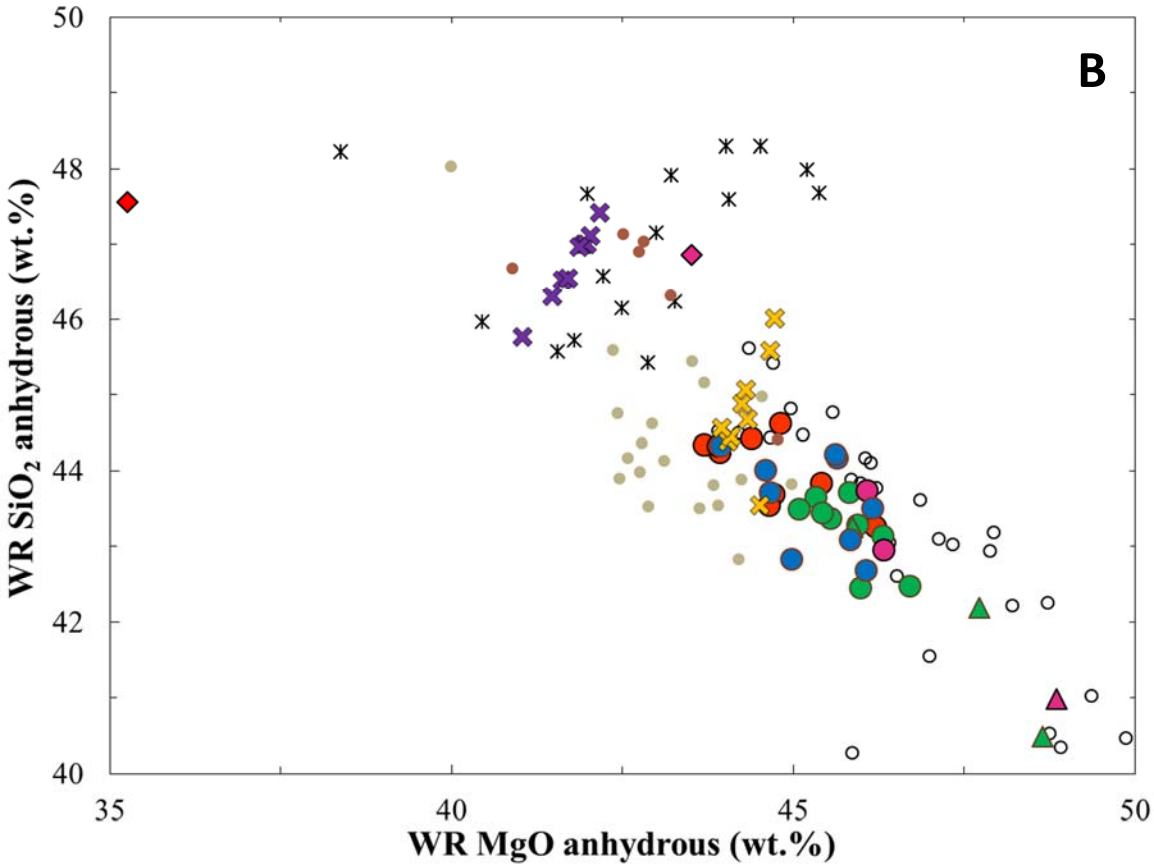

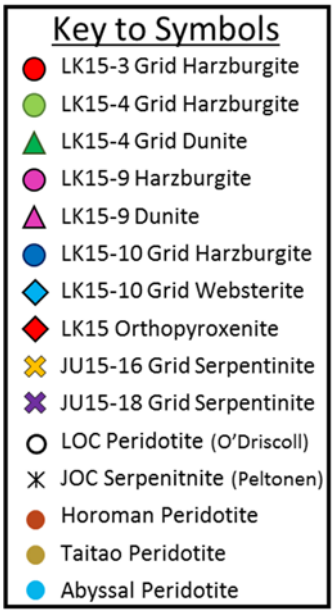

Figure 10. Plots of whole-rock XRF major element data; **A**. Al_2O_3 vs MgO **B**. SiO_2 vs MgO (all values plotted wt % anhydrous). Shown for comparison are whole rock data for Leka peridotites (O'Driscoll et al., 2015), Jormua serpentinites (Peltonen et al., 1998), Horoman peridotites (Saal et al., 2000), peridotites from the Taitao ophiolite (Schulte et al., 2009), abyssal peridotites (Brandon et al., 2000), and Primitive Mantle (**PM**) estimates (McDonough and Sun, 1995). Shown in **A** are general trends for the effects of peridotite melt depletion (**purple**) and serpentinization (**green**).

4.1.2. Jormua serpentinites

Major element data for JOC samples are presented in **Table 1**. The JOC serpentinites have compositions that are similar to previously published data on JOC peridotites (e.g., Peltonen et al., 1998; Tsuru et al., 2000). JOC samples also plot within a compositional range, common to abyssal peridotites, and peridotites associated with other ophiolites (**Fig. 7A**). The LOI for all JOC samples fall between 11.0 and 11.4 wt %. Whole-rock (WR) concentrations of Al_2O_3 (anhydrous corrected, wt %) range from 1.0 to 1.9 wt % for all JOC samples. WR concentrations of JOC serpentinites show general negative correlations of Al_2O_3 and SiO_2 with MgO (**Fig. 10A and B**). However, serpentinites from individual grid locations (e.g., JU15-16 and JU15-18) show positive correlations of SiO_2 with MgO. Samples from grid location JU15-16 also show a positive correlation of Al_2O_3 with MgO, while JU15-18 grid samples show a negative correlation for these elements.

As with Leka peridotites, lower Al_2O_3 and higher MgO concentrations observed in JOC serpentinites, relative to primitive mantle (PM) estimates (McDonough & Sun, 1995), are broadly consistent with prior melt depletion (**Fig. 10A**). Plotted values of Al_2O_3 and MgO (anhydrous corrected, wt %) for JOC grid locations JU15-16 and JU15-18 (**Fig. 10A**), show depletions in MgO of JU15-18 samples compared to JU15-16 samples (~3 km away; **Fig. 4**), yet display similar ranges of Al_2O_3. Averaged Mg# of grids JU15-16 and JU15-18 are 91.1 and 89.9, respectively.

4.2. Minor and trace elements

4.2.1. Leka peridotites and pyroxenites

Lithophile, trace element data for LOC samples are presented in **Table 2**. Primitive mantle normalized (McDonough & Sun, 1995) trace element abundances for LK15-4, LK15-10, and LK15-3 grid samples, are shown in **Fig. 11A, B, and C** respectively. In general, LOC samples are depleted in all incompatible trace elements relative to PM estimates, except for: B, Cr, and Ba, with enrichments in W for LK15-10 grid samples. LOC samples are also depleted in Ti, Pb, and Th (relative to other trace elements). Many LOC harzburgites and dunites exhibit U-shaped rare earth element (REE) patterns with negative gradients from light REE (LREE) to middle REE (MREE) and positive gradients from MREE to heavy REE (HREE). This is more pronounced in the LK15-4 grid samples. Dunites in LK15-4 show greater overall enrichment in HREE relative to LREE in comparison to most harzburgites (**Fig. 11A**). PM-normalized REE values of LK15-10 grid samples (1 to 10^{-2} x PM; **Fig. 11B**), are in general, nearly an order of magnitude higher than LK15-4 grid samples (~10^{-1} to 10^{-3} x PM; **Fig. 11A**) and show overall flatter normalized REE patterns. Several harzburgites in both LK15-4 and LK15-10 grids, exhibit significant positive Eu anomalies, despite having no plagioclase in the LOC rocks. PM-normalized REE values of LK15-3 grid samples (~1 to 10^{-2} x PM, **Fig. 11C**) show broadly homogeneous REE patterns with positive gradients from LREE to HREE.

4.2.2. Jormua serpentinites

Trace element data for JOC samples are presented in **Table 2**. Primitive mantle normalized (McDonough & Sun, 1995) trace element abundances for JU15-16 and JU15-18 grid samples, are shown in **Fig. 11D and E**, respectively. In comparison to LOC samples, JOC serpentinites show less variability between samples at individual grid

locations. Samples from grid location JU15-16 are in general, depleted in incompatible trace elements relative to PM estimates (**Fig. 11D**). Most serpentinites from JU15-16, however, are enriched in Li and B, yet have variable depletions in Rb, Cs, and Pb (**Table 2** and **Fig. 11D**). Additionally, JU15-16 serpentinites show fractionation of Cu between samples (some enriched, some depleted). Some samples from LOC grid location LK15-10, display similar trends of Cu between samples (**Fig. 11B**), but not as pronounced as JU15-16 samples. Most JU15-16 grid samples are characterized by HREE enrichment, relative to LREE, and all are depleted relative to PM estimates (<1 to $>10^{-1}$ x PM). JU15-16 serpentinites also show both significant positive and negative Eu anomalies.

Unlike JU15-16 grid samples, samples from grid location JU15-18 are in general, more enriched in incompatible trace elements relative to JU15-16 grid samples (**Fig. 11E**). JU15-18 serpentinites show variable depletions in Sr as well as normalized concentrations of Ba that range from enriched to depleted. Trace element data for grid sample JU15-18 B2 show strong enrichments in Ti, Zr, Nb, Hf, Ta, and U; and depletions in Cr, Co, Nu, and Cu, relative to other JU15-18 grid serpentinites. REE concentrations of JU15-18 serpentinites are enriched relative to primitive mantle (~10 to 1 x PM), and exhibit overall negative gradients from LREE to HREE, atypical of serpentinized peridotites. The REE patterns displayed by JU15-18 samples suggest that these samples do not represent simple melt residues.

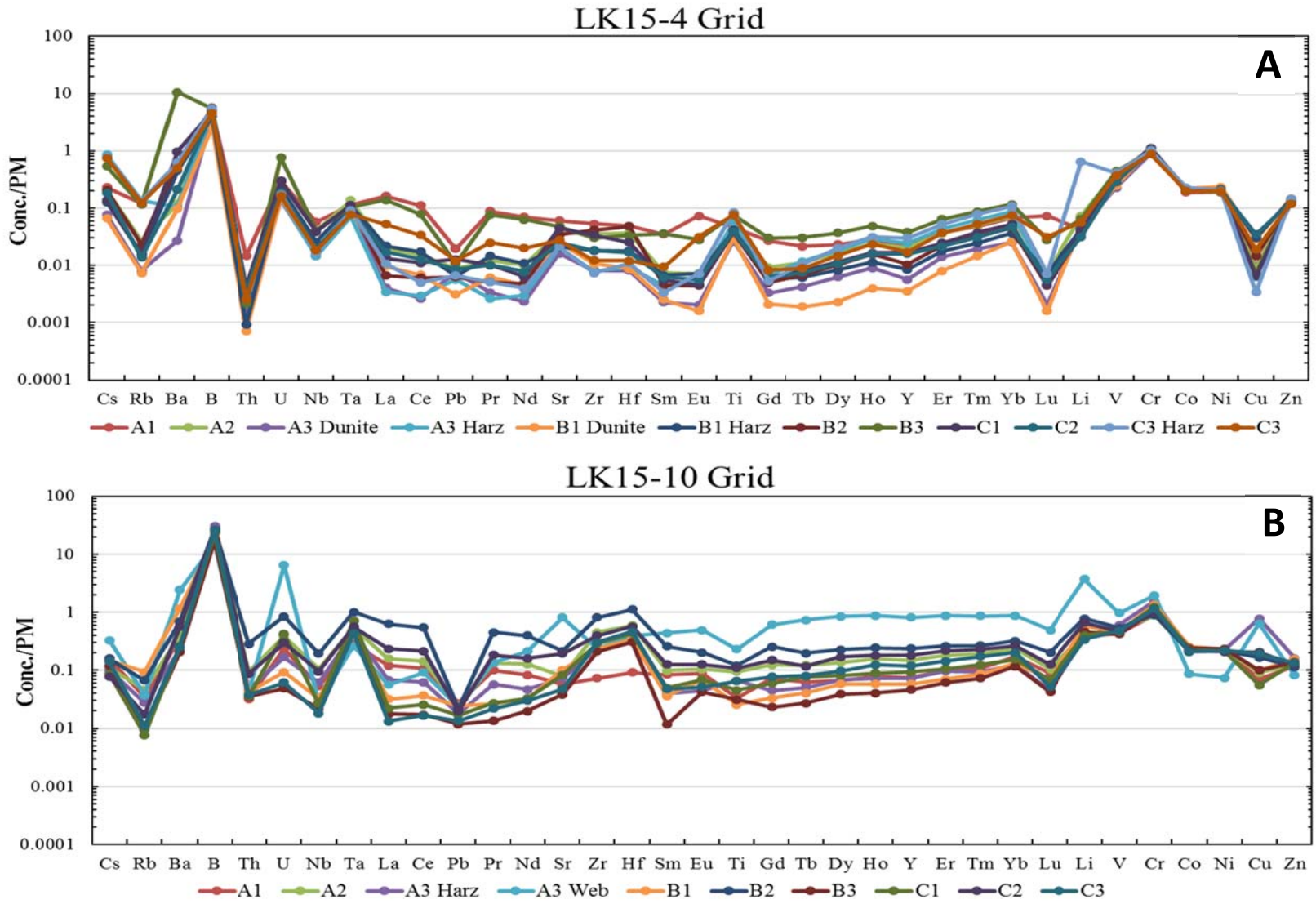

Figure 11. (A) Primitive mantle normalized trace element patterns for LOC LK15-4 grid peridotites. (B) Primitive mantle normalized trace element patterns for LOC LK15-10 grid peridotites. Normalization values from McDonough & Sun (1995).

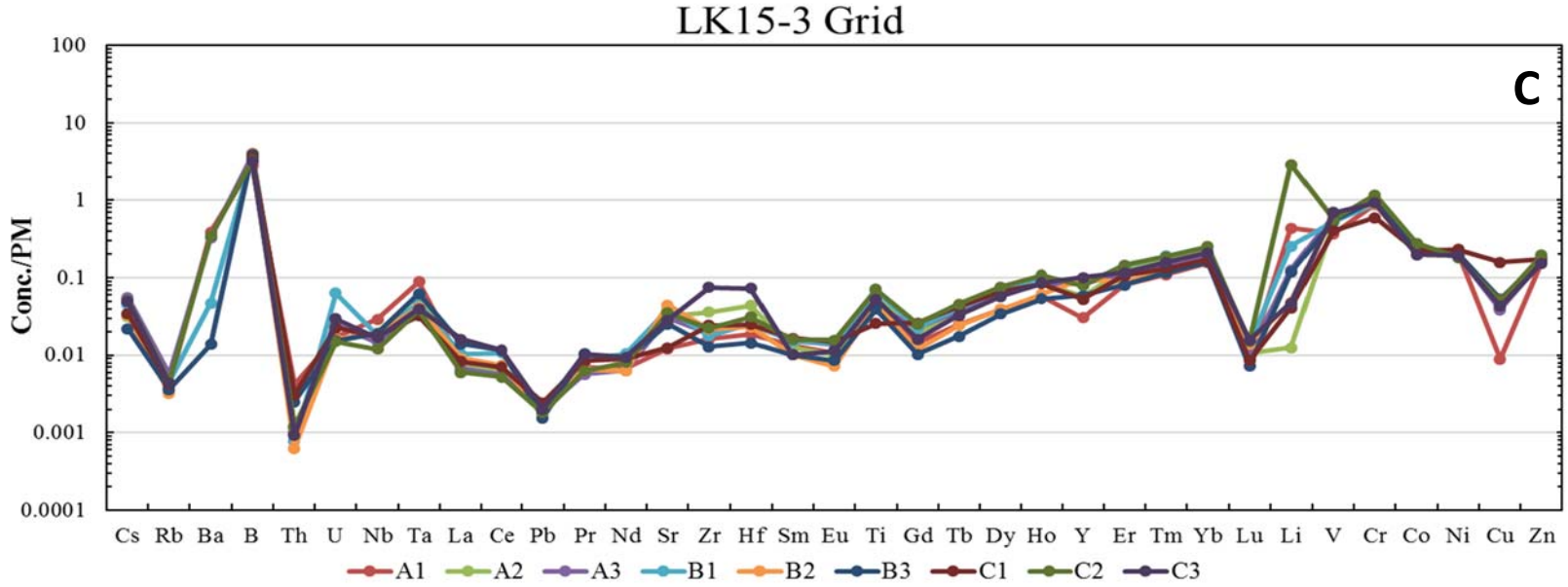

Figure 11. (C) Primitive mantle normalized trace element patterns for LOC LK15-3 grid peridotites. Normalization values from McDonough & Sun (1995).

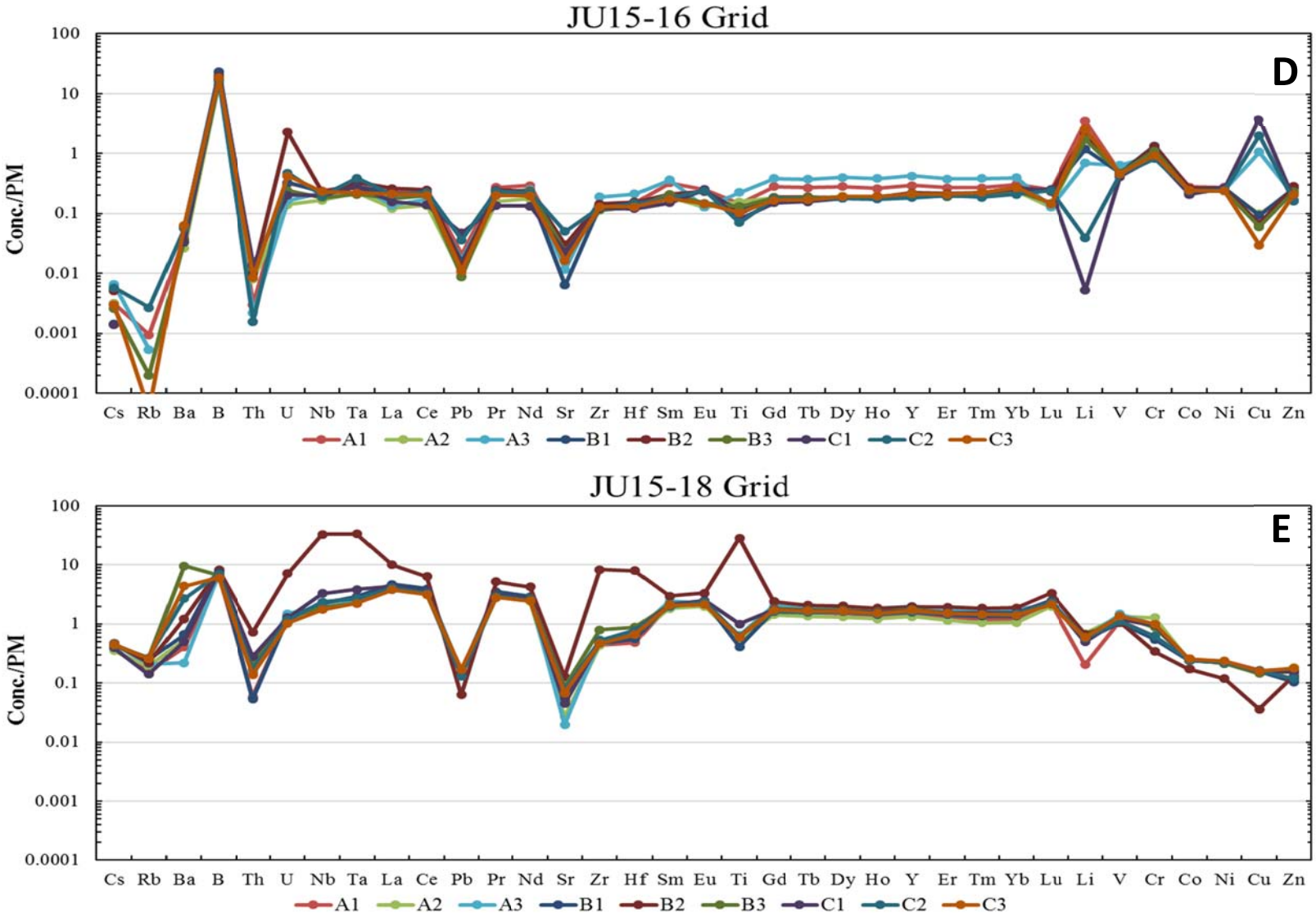

Figure 11. (D) Primitive mantle normalized trace element patterns for JOC JU15-16 grid serpentinites. (E) Primitive mantle normalized trace element patterns for JOC JU15-18 grid serpentinites. Normalization values from McDonough & Sun (1995).

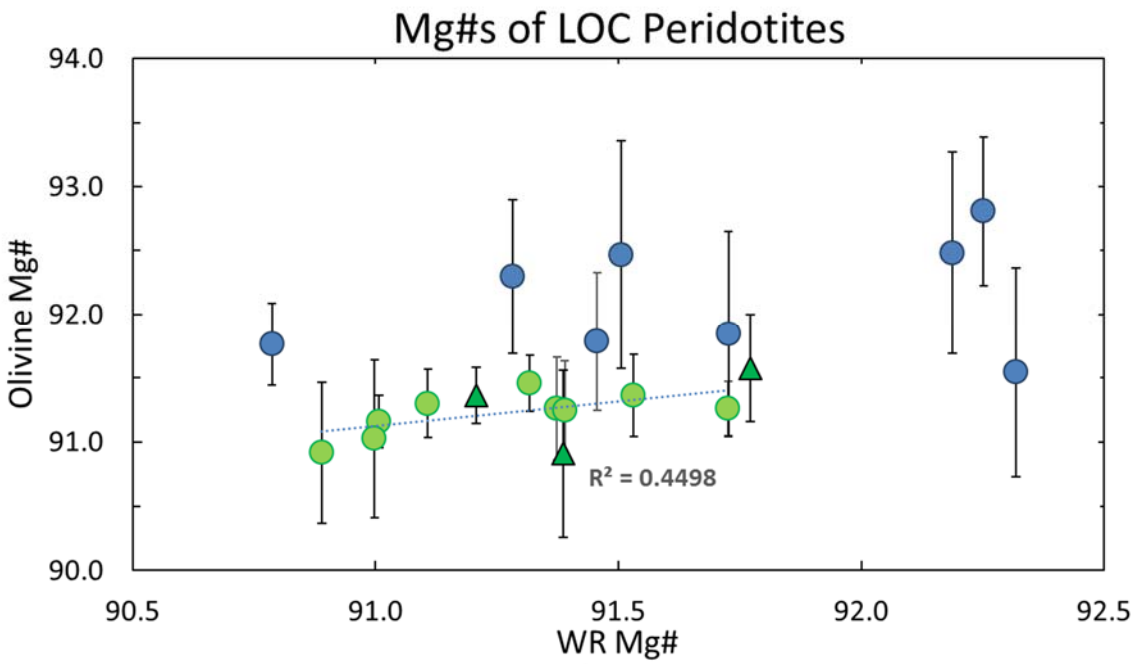

Figure 12. Plot of averaged Mg# in relict olivine grains vs. Mg# of whole rock LOC peridotite. Y-axis error bars show Mg# variation (2SD) among olivine grains within each sample. Symbols for LK15-4 and LK15-10 grid samples are the same as previous plots.

4.3. Olivine compositions

Averaged electron microprobe data for olivines in LOC peridotites are shown in **Table 3**. With the exception of LK15-10 C2, all of the harzburgites and dunites contain relict olivine grains with overall low degrees of serpentinization (20-40%). LK15-10 samples show greater variation (2SD) between individual olivine grains in all major elements in comparison to LK15-4 samples. The Mg# of olivine grains vary from 90.9 to 92.8 within the two grids. There are weak positive correlations between the average Mg# of olivine grains and the WR Mg# (r^2 = 0.45) (**Fig. 12**) for LK15-4 harzburgites. No relict olivine grains are preserved for JOC serpentinites.

4.4. HSEs and Re-Os isotopic systematics

4.4.1. Leka peridotites and pyroxenites

The HSE concentration data for LOC samples are provided in **Table 4**. The average abundances for LOC harzburgites for Os, Ir, Ru, Pt, Pd, and Re are 4.1, 3.0, 4.9, 9.3, 6.0, and 0.03 ppb, respectively (n = 23). Average LOC harzburgite abundances are in good agreement with previously analyzed LOC harzburgites (O'Driscoll et al., 2015). Current estimates for PM HSE abundances are (in ppb; 2SD) 3.9 ± 0.5 Os, 3.5 ± 0.4 Ir, 7.0 ± 0.9 Ru, 7.6 ± 1.3 Pt, 7.1 ± 1.3 Pd, and 0.35 ± 0.6 Re (Becker et al., 2006). PM-normalized HSE abundances for LOC peridotites and pyroxenites are plotted in **Fig. 13A-D**, and are compared with previously analyzed peridotites from the Kvaløya-moen locale (O'Driscoll et al., 2015). Most HSE patterns for LOC peridotites are flat or have depletions relative to PM in the typically incompatible elements Pd and Re.

The LOC dunites from grid location LK15-4 exhibit HSE patterns and concentrations similar to harzburgites from that location (**Fig. 13A**). Dunite sampled from a 0.5 m - thick channel (LK15-9C; **Fig. 13C**) are depleted in all of the HSE (10^{-1} to 10^{-2} x PM) and have the lowest Pt and Pd of all LOC samples examined (~0.1 ppb).

The two LOC orthopyroxenites are characterized by flat HSE patterns for the I-PGE (Os, Ir, and Ru) and hump-shaped patterns for the P-PGE (Pt and Pd, plus Re), with enrichments in Pt (94.2 and 187.4 ppb) and Pd (47.1 and 80.8 ppb) (**Table 4**; **Fig. 13D**). The HSE patterns of these orthopyroxenites show similar patterns to previously analyzed LOC orthopyroxenites (O'Driscoll et al., 2015). The HSE pattern of the websterite channel from grid location LK15-10, exhibits lower concentrations relative to PM of I-PGE (10^{-1} to 10^{-2} x PM), and hump-shaped patterns and concentrations of P-PGE, similar to LOC orthopyroxenites.

Figure 13. Primitive mantle normalized (from Becker et al., 2006) HSE patterns for: (**A**) LK15-4 grid harzburgites and dunites, with a highlighted field for LOC peridotites from Kvaløya-moen, analyzed in O'Driscoll et al., (2015). Subchondritic γOs sample, LK15-4 A3 Harz, is highlighted in red. (**B**) LK15-10 grid harzburgites (the highlighted field is for LK15-4 grid peridotites from (**A**)). (**C**) LK15-9 non-grid, harzburgites and dunites. (**D**) LOC orthopyroxenite, websterite (with highlighted fields for LK15-4 and LK15-10 grid peridotites from (**A**) and (**B**), respectively). Grid locations are shown in **Fig. 3**, indicated by the colored stars. Symbols are the same as previous figures.

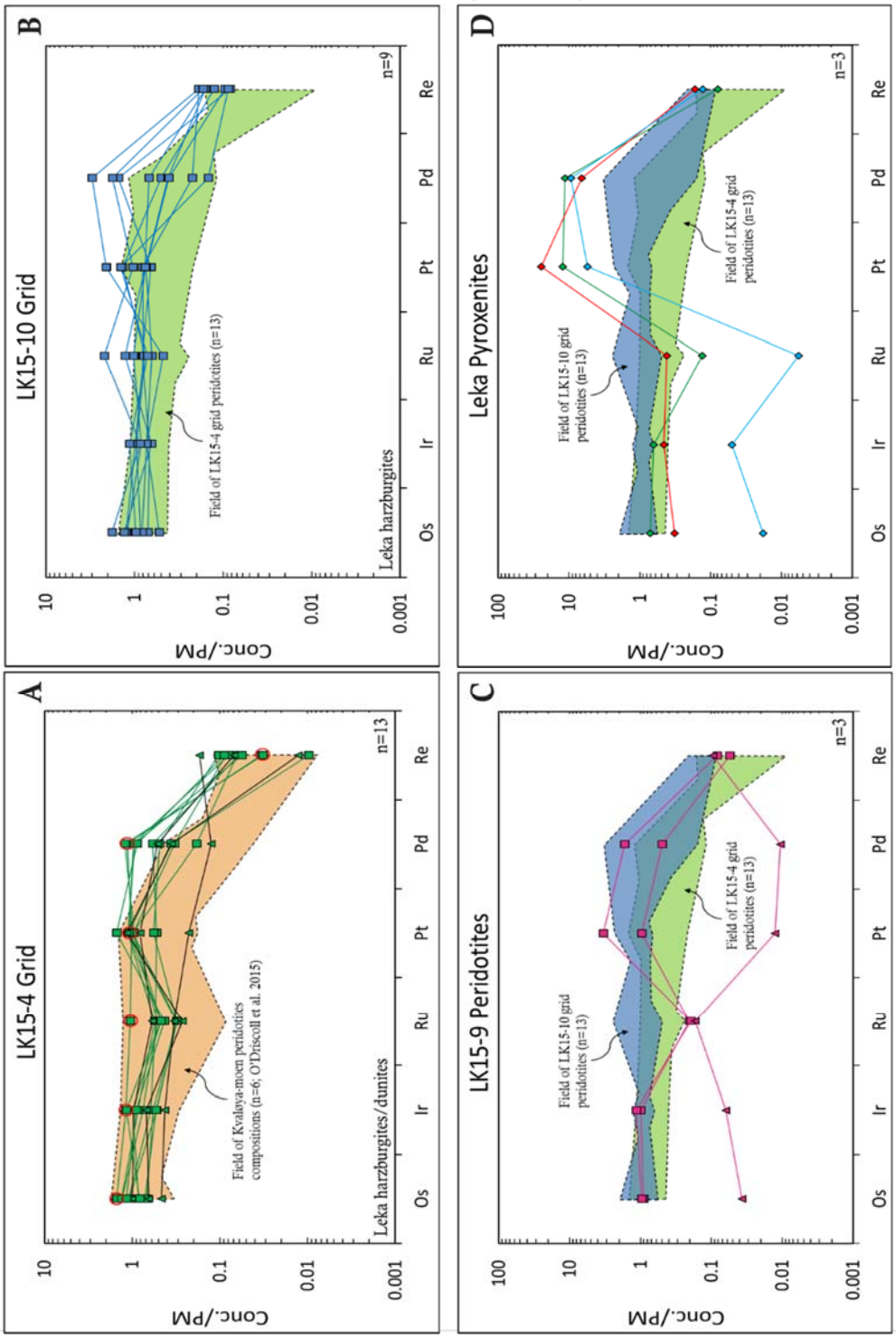

Rhenium-Osmium isotopic data for all of the LOC samples are provided in **Table 4**. The $^{187}Re/^{188}Os$ ratios for harzburgites range from 0.005 to 0.156 (average $^{187}Re/^{188}Os = 0.042$, including duplicate analyses; n = 23); all are subchondritic (<0.4). The $^{187}Re/^{188}Os$ ratios of LOC dunites (most are from the LK15-4 grid area) are on average, higher and show more variation than adjacent harzburgites, ranging from 0.009 to 1.125 (average $^{187}Re/^{188}Os = 0.331$; n = 4). The two orthopyroxenites (LK15-4 A3(2) and LK15-3 Ortho) analyzed have $^{187}Re/^{188}Os$ ratios of 0.048 and 0.223. The observed ratios of these analyzed orthopyroxenites are lower than previously analyzed LOC orthopyroxenites by O'Driscoll et al., (2015) of 0.555 and 1.25. LK15-4 A3(2) ($^{187}Re/^{188}Os = 0.048$), an orthopyroxenite vein hosted in harzburgite, has the lowest $^{187}Re/^{188}Os$ (0.048) of all LOC orthopyroxenites analyzed.

On a plot of $^{187}Re/^{188}Os$ versus $^{187}Os/^{188}Os$, most LOC samples plot near a 497 Ma chondritic reference isochron (**Fig. 14A and B**). To describe the Os isotopic composition at a specific time, the term $\gamma Os_{(T)}$ is used, which describes the percentage difference between the Os isotopic composition of a sample at any time (T) and a chondritic reference value at that time:

Eq. 2. $$\gamma Os = \left[\frac{^{187}Os/^{188}Os_{\text{sample (T)}}}{^{187}Os/^{188}Os_{\text{chond(T)}}} - 1\right] x\ 100$$

Samples with positive $\gamma Os_{(T)}$ are described as enriched or suprachondritic and imply long-term elevated $^{187}Re/^{188}Os$. Samples with negative $\gamma Os_{(T)}$ are described as depleted or subchondritic and imply long-term lowered $^{187}Re/^{188}Os$ (Shirey and Walker, 1998).

Samples from grid location LK15-4 generally have suprachondritic initial $\gamma Os_{(497\ Ma)}$ values and plot above the 497 Ma reference isochron. By contrast, samples from grid location LK15-10 have initial $\gamma Os_{(497\ Ma)}$ values ranging from chondritic (e.g., A3) to

subchondritic (e.g., C1) and plot on or below the 497 Ma reference isochron. For most samples, age corrections to obtain initial ratios are minor (**Table 4**), due to low Re/Os of LOC samples.

Initial $\gamma Os_{(497\ Ma)}$ values for harzburgites from grid location LK15-4 (**Fig. 3; map**) range from +2.2 to -2.1 (**Table 4**), while harzburgites from grid location LK15-10 range from +0.4 to -1.5. These values are shown in grid format in **Fig. 15A and B**. Replicate analyses of subchondritic sample LK15-4 A3 (Harz) (-2.1 and -1.9), are reproducible within analytical uncertainty (±0.2). It is noteworthy that sample LK15-4 A3 (Dunite), collected in the same 1 m^2 grid square as LK15-4 A3 (Harz), exhibits a suprachondritic $\gamma Os_{(497\ Ma)}$ of +1.5. By contrast, adjacent dunites and harzburgites collected in other LK15-4 grid squares, B1 and C3, show $\gamma Os_{(497\ Ma)}$ values that fall within uncertainty of each other (**Table 4**; **Fig. 15A**).

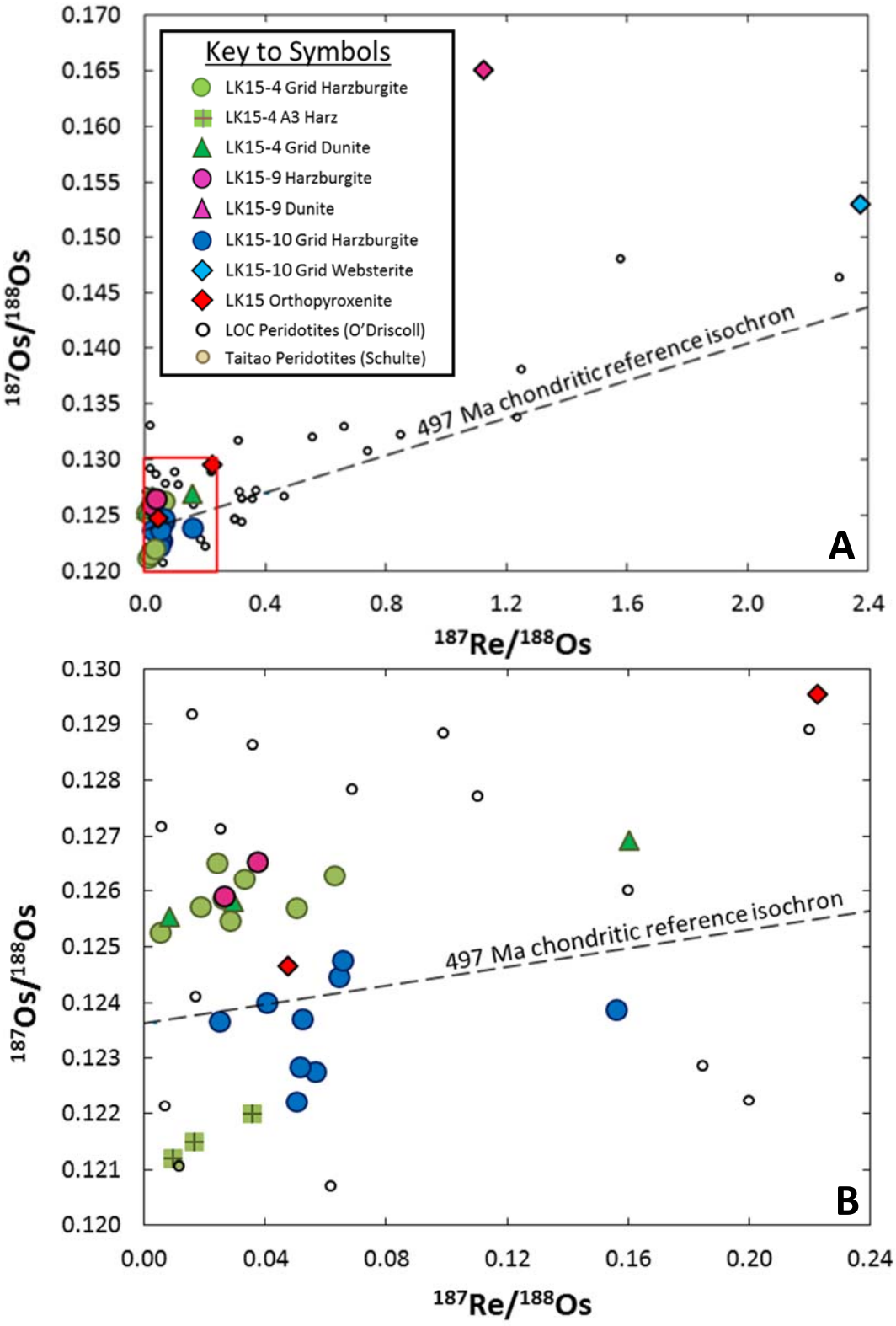

Figure 14. Plots of $^{187}Re/^{188}Os$ vs $^{187}Os/^{188}Os$ for LOC harzburgites, dunites, orthopyroxenites, and websterites with a reference isochron of 497 Ma shown, calculated from chondritic values of Shirey & Walker (1998). The red box in (a) outlines low $^{187}Re/^{188}Os$ - $^{187}Os/^{188}Os$ samples shown in (b). In (b), squares with crosses indicate subchondritic harzburgites from grid square LK15-4 A3. Data from a previous LOC study (O'Driscoll et al., 2015) are included for comparison.

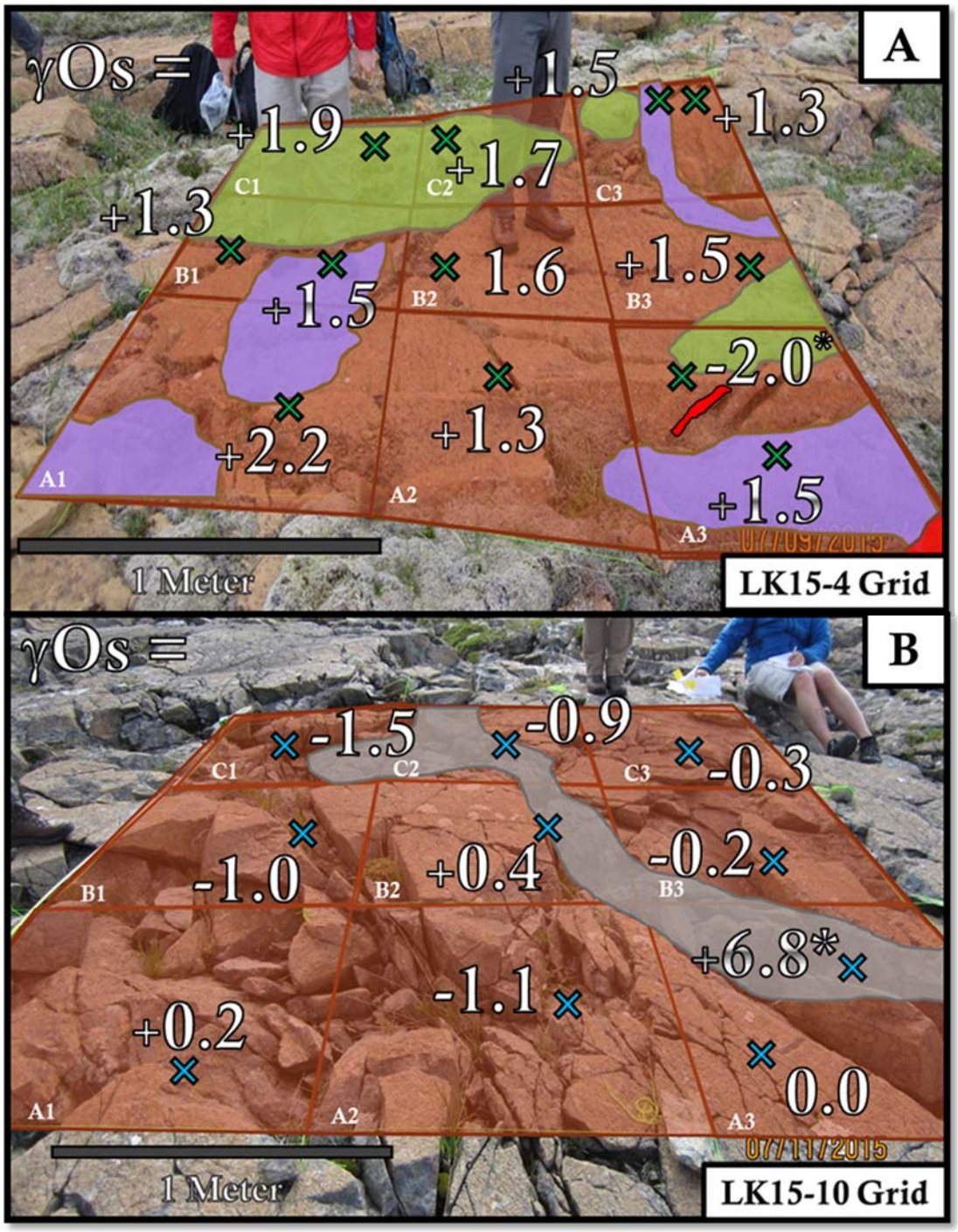

Figure 15. (left) 3 m x 3 m LOC grids located in the harzburgite mantle section in northern Leka, Norway. Grids are divided into 9 1 m^2 grid squares. **LK15-4** (**A**) and **LK15-10** (**B**) are shown in **Fig. 3** by the **green** and **blue** stars respectively. Colored Xs indicate approximate sample locations within each labeled grid square. Initial γOs values for samples are shown adjacent to Xs and are calculated for 497Ma. Uncertainties on $\gamma Os_{(497\ Ma)} = \pm 0.2$

4.2.2. Jormua serpentinites

The HSE concentration data for JOC samples are provided in **Table 4**. The average abundances for JOC serpentinites for Os, Ir, Ru, Pt, Pd, and Re are 3.6, 3.7, 9.0, 5.5, 2.9, 0.09 ppb, respectively (n = 26). PM-normalized HSE abundances for JOC serpentinites are plotted in **Fig. 16A and B**. Most patterns for JOC peridotites are flat or have depletions relative to PM in the typically incompatible elements Pt, Pd, and Re. HSE abundances for grid location JU15-16 are slightly enriched in Os, Ir, Ru, Pt, and Pd, relative to grid JU15-18 (~3 km away; **Fig. 4**), yet heavily depleted in Re (10^{-1} to 10^{-2} x PM) compared to JU15-18 serpentinites (~0.5 x PM).

Rhenium-Osmium isotopic data for all of the JOC samples are provided in **Table 4**. The $^{187}Re/^{188}Os$ ratios for JOC serpentinites range from 0.012 to 0.739 (average $^{187}Re/^{188}Os$ = 0.168; n = 26); most serpentinites are subchondritic (<0.4), with the exception of samples JU15-18 A1, A3, B1, and B3, from grid location JU15-18 (averaged grid $^{187}Re/^{188}Os$ = 0.491; n= 9). By contrast, JU15-16 grid serpentinites (~3 km away; **Fig. 4)** exhibit much lower $^{187}Re/^{188}Os$ ratios (average $^{187}Re/^{188}Os$ = 0.028, including duplicate analyses; n = 10).

On a plot of $^{187}Re/^{188}Os$ versus $^{187}Os/^{188}Os$, most JOC samples plot above or below a 1.95 Ga chondritic reference isochron (**Fig. 17**). Samples from grid location JU15-16 generally have subchondritic initial $\gamma Os_{(1.95\ Ga)}$ values (-0.7 to -3.0) and plot below the 1.95 Ga reference isochron. In comparison, serpentinites from grid location JU15-18 show a much wider range with initial $\gamma Os_{(1.95\ Ga)}$ values, ranging from +8.3 to -3.3, with suprachondritic (e.g., B2 and B3), chondritic (e.g., A3 and C1), to slightly subchondritic (e.g., A1 and C2) initial values. Initial $\gamma Os_{(1.95\ Ga)}$ values for all JOC grid-sampled serpentinites are shown in grid format in **Fig. 18**.

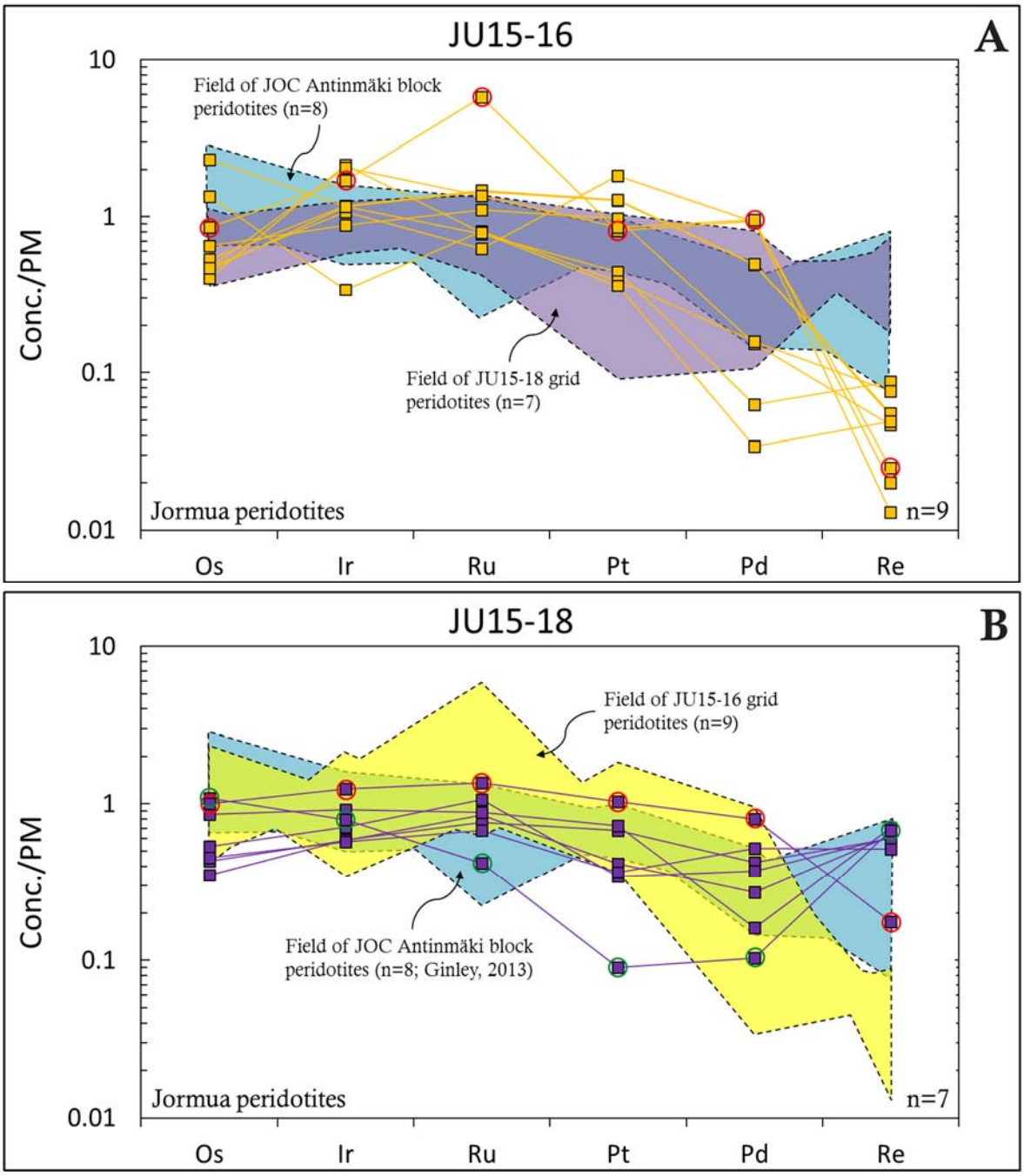

Figure 16. Primitive mantle normalized (from Becker et al., 2006) HSE patterns for Jormua peridotites (**A**) JU15-16 grid peridotites, the highlighted **purple** field is for JU15-18 grid peridotites from (**B**). (**B**) JU15-18 grid peridotites, the **yellow** field is for JU15-16 grid peridotites from (**A**)). Suprachondritic γOs sample, JU15-18 B2 (+8.3), is circled in **red**, while subchondritic γOs sample, JU15-18 C2 (-3.3), is circled in **green**. Grid locations are shown in **Fig. 4**, indicated by the colored stars. The highlighted **blue** field on both plots are non-grid JOC peridotite compositions from the Antinmäki block.

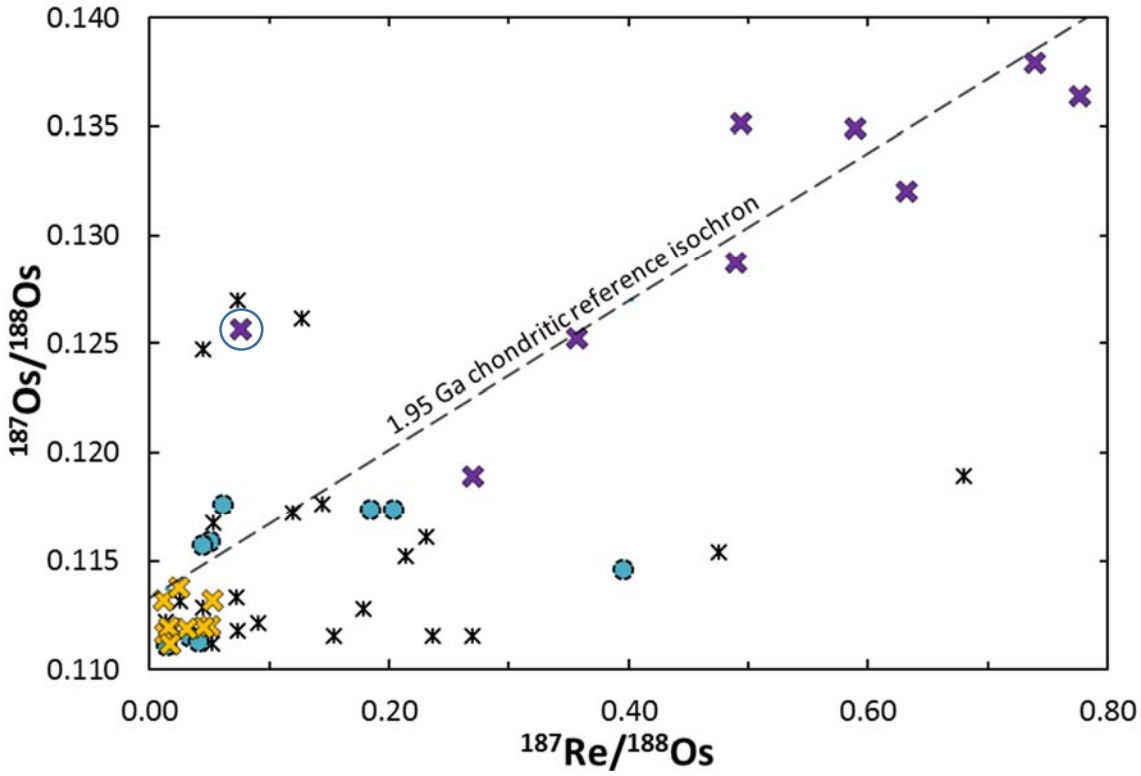

Figure 17. Plots of $^{187}Re/^{188}Os$ vs $^{187}Os/^{188}Os$ for JOC serpentinites with a reference isochron of 1.95 Ga shown, calculated from chondritic values from Shirey & Walker (1998). Data from a previous JOC study (Tsuru et al., 2000) are included for comparison. Suprachondritic γOs sample JU15-18 B2 is circled in blue.

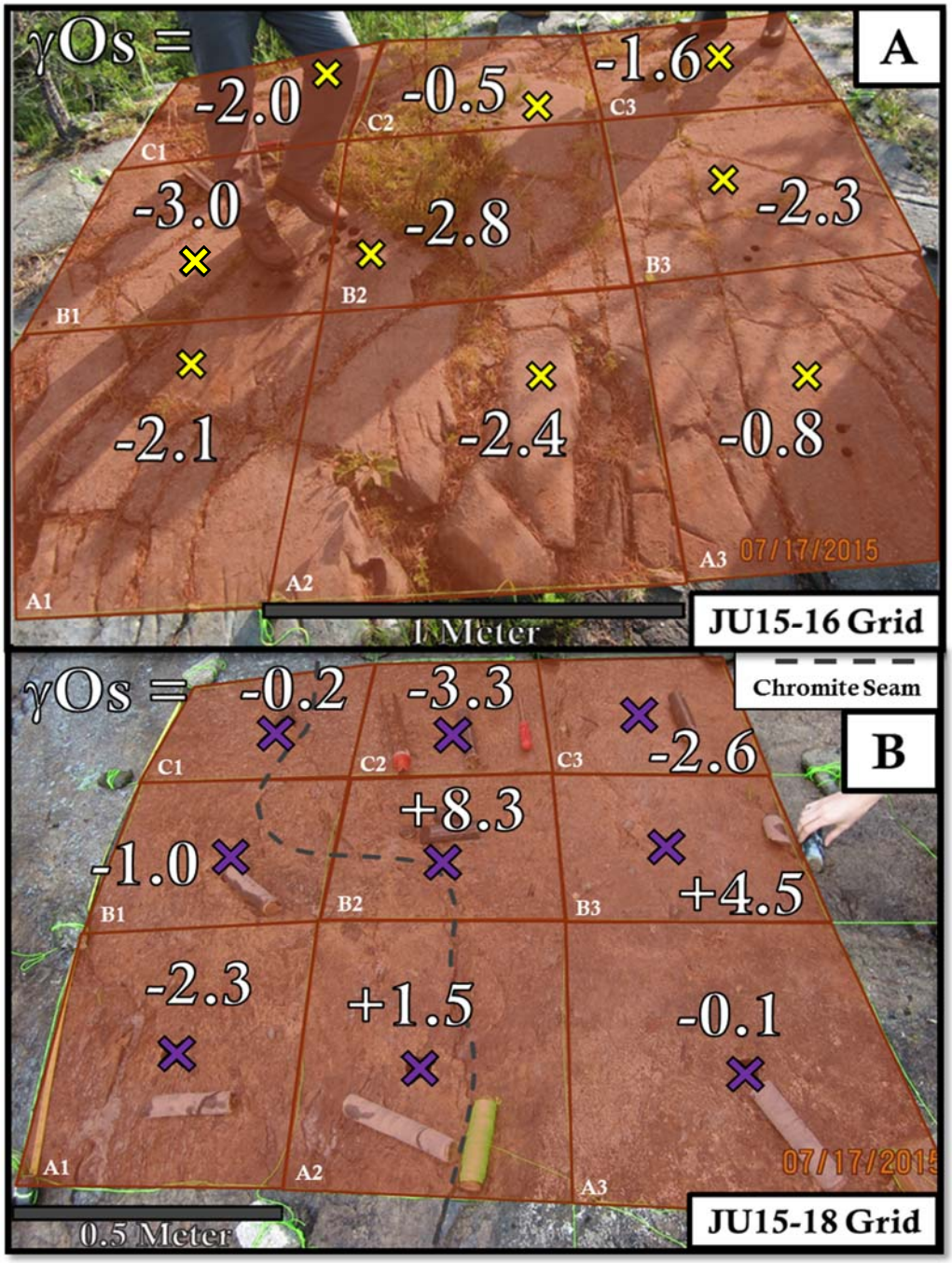

Figure 18. 3 m x 3 m and 1.5 m x 1.5 m JOC grids located in the eastern Antinmäki block near Kajaani, Finland. Grids are divided into 9 0.5-1 m^2 grid squares. **JU15-16** (**A**) and **JU15-18** (**B**) are shown in **Fig. 4** by the **yellow** and **purple** stars respectively. Colored Xs indicate approximate sample locations within each labeled grid square. Initial γOs values for samples are shown adjacent to Xs and are calculated for 1.95 Ga. Uncertainties on $\gamma Os_{(1.95\ Ga)} = \pm 0.2$.

5. Leka Discussion

5.1. Melt depletion in LOC peridotites

5.1.1. Major and trace element data

Leka ophiolite complex peridotites are characterized by low Al_2O_3, relative to estimates for the PM and DMM (**Fig. 10A**). In previous studies (Snow and Dick, 1995), low Al_2O_3 in oceanic peridotites has been interpreted to be a result of pervasive marine weathering and partial melting. Pervasive marine weathering of peridotites is often accompanied by high degrees of serpentinization and major losses in MgO. For LOC peridotites, marine alteration as an explanation for low WR Al_2O_3 is unlikely, as neither of these features are observed. Whole-rock concentrations of Al_2O_3 and MgO, are instead interpreted to be dominated by melt depletion. Consistent with this interpretation, they plot on a general melt depletion trend (**Fig. 10A**). Based on this trend, the lower concentrations of Al_2O_3 and higher concentrations of MgO, provide evidence for higher degrees of melt depletion in LK15-4 samples, relative to LK15-10 samples. However, the MgO concentrations in LK15-4 and LK15-10 show considerable overlap despite differences in Al_2O_3 concentrations. This could be a result of slight MgO loss as a result of higher degrees of serpentinization (i.e., higher bulk-rock LOI) in LK15-4 samples, relative to LK15-10 samples.

Leka ophiolite complex peridotites from the LK15-4 grid are also characterized by linear trends between some major and trace elements, such as Al_2O_3 vs. V (R^2 = 0.92; **Fig. 19**). In previous studies (Azimow, 1999; Takazawa et al., 2000; Le Roux et al., 2007; Van Acken et al., 2008; Schulte et al., 2009), such trends have commonly been attributed to either variable extents of partial melting, or mixing between depleted and enriched materials, which can occur via refertilization. Refertilization refers to the process where melt is reintroduced to previously melt-depleted peridotite, and can result in the creation of hybrid rocks (e.g., Saal et al., 2001; Takazawa et al., 2000; Le Roux et al., 2007; and Van Acken et al., 2008). Evidence for refertilization in mantle rocks can include, linear trends between major elements such as, Mg or Al, and some minor elements, including Ti (Bodinier et al., 2008). Samples from grid location LK15-4 also show a positive linear trend between Al_2O_3 and Ti (R^2 = 0.64; **Fig. 20**), but a weak correlation between MgO and

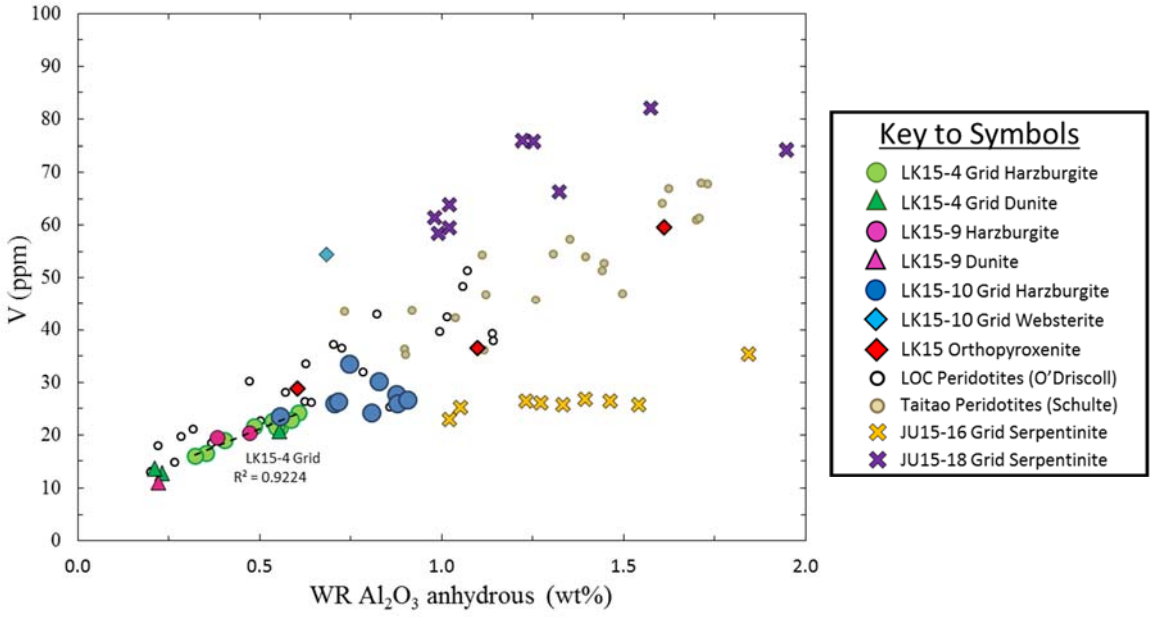

Figure 19. Plot of Al_2O_3 (anhydrous wt%) vs V for LOC peridotites/pyroxenites and JOC serpentinites. Data from a previous LOC study (O'Driscoll et al., 2015) and the Taitao ophiolite (Schulte et al., 2009) are included for comparison. The R^2 values is calculated using least-squares regression in Microsoft Excel.

Ti (R^2 = 0.35; Supp). The linear trends between Al_2O_3 vs Ti and V indicate that refertilization or partial melting, may have played a role in the history of LK15-4 grid samples.

In contrast to LK15-4 samples, peridotites from grid LK15-10 do not show any obvious correlations between V and Al_2O_3 (**Fig. 19**), or Ti and MgO or Al_2O_3 (**Fig. 20**; Supplementary). The lack of correlation between these elements in LK15-10 grid samples, suggests that LK15-10 samples were not strongly affected by refertilization processes. However, based on the significant Al-depletion present in all LOC peridotite samples, the dominant compositional control on LOC peridotites was likely variable extents of melt

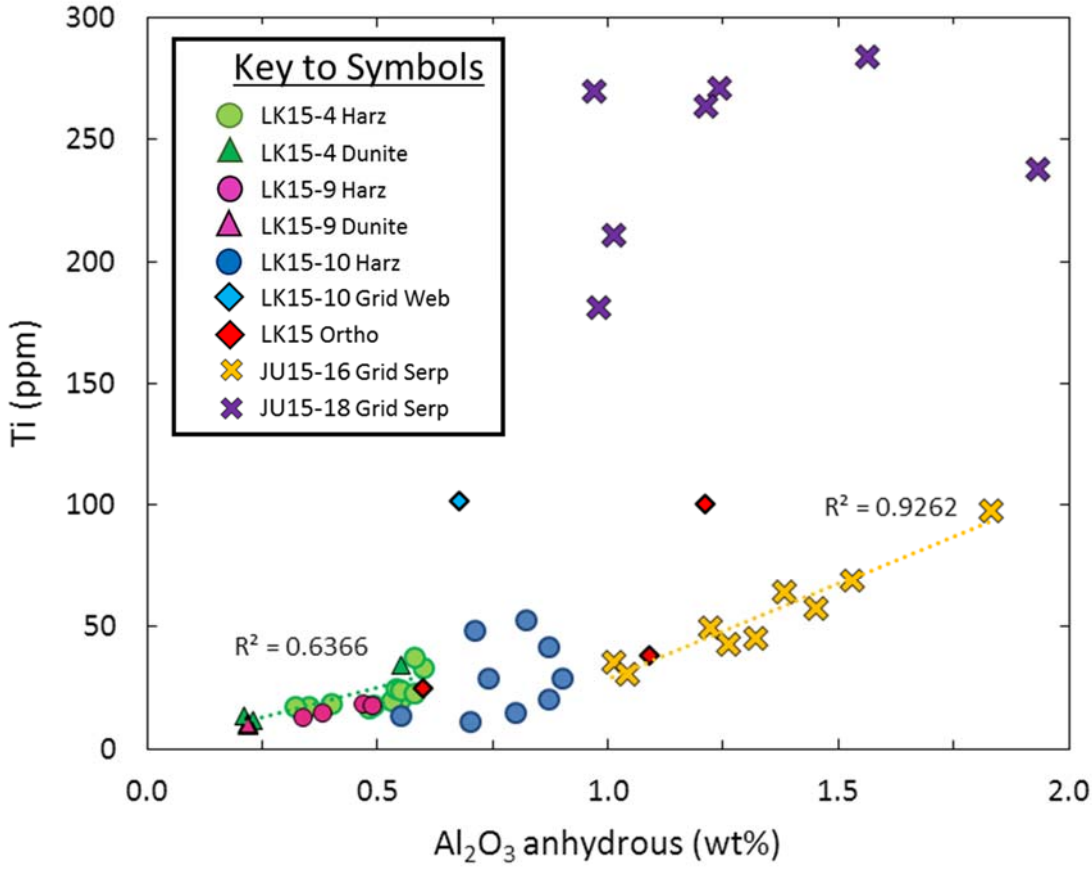

Figure 20. Plot of Al_2O_3 (anhydrous wt%) vs Ti for LOC peridotites/pyroxenites and JOC serpentinites. The R^2 values is calculated using least-squares regression in Microsoft Excel.

depletion. We conclude that the low Al_2O_3 in LOC peridotites requires at least one stage of partial melting and melt removal.

To assess the conditions during mantle melting of different oceanic peridotites, Pearce & Parkinson (1993) used trace elements with different compatibilities, and demonstrated that a bivariate plot of Ti vs. Yb can be used to assess whether melting occurred in the garnet or spinel stability fields. In the spinel stability field, both Ti and Yb are highly incompatible, whereas if mantle melting occurs in the presence of garnet, extraction of Yb into the melt is suppressed relative to Ti, and Yb behaves instead as only a moderately incompatible element. Pearce & Parkinson (1993) and Parkinson & Pearce (1998) also used bivariate plots of V vs. Yb in order to assess oxygen fugacity conditions during mantle melting. In mid-ocean ridge settings (~QFM – 1 (quartz-fayalite-magnetite buffer)), V behaves as a moderately incompatible element. However, under the more oxidizing conditions during SSZ melting (~QFM + 1), V acts as a highly incompatible trace element.

Plots of Ti vs. Yb and V vs. Yb for LOC peridotites are shown in **Fig. 21A** and **21B**, respectively. Concentrations of Ti vs. Yb, and the trends they form (**Fig. 21A**), indicate that most LOC harzburgites underwent high degrees of partial melting (>20%). This conclusion is consistent with the major element data (**Fig. 11**). Additionally, these trends imply that melt extraction occurred in the absence of garnet for grid LK15-4 samples, supporting a shallow-level of SSZ-related melting. This observation is shared by previous work on LOC peridotites (O'Driscoll et al., 2015). Harzburgites from grid location LK15-4 show compositions that are typical for high degrees of melting (~23-26%) Higher enrichment of Ti in LK15-4 peridotites, relative to LK15-10, may reflect mantle melting in the presence of amphibole. Pearce and Parkinson (1993) noted that Yb and Ti

concentrations during mantle melting in the presence of amphibole has the opposite effect to the presence of garnet, whereby amphibole preferentially retains Ti relative to Yb.

By comparison, LK15-10 grid samples are distinct from LK15-4 grid samples, with characteristics suggestive of lower degrees of melt extraction (~18-24%), between the garnet and spinel melting fields. This indicates that LK15-10 harzburgites melted at slightly higher pressures than the LK15-4 harzburgites (**Fig. 21A**).

Concentrations of V vs. Yb for samples in both grids (**Fig. 21B**) indicate that LOC peridotites underwent melt depletion under relatively oxidizing conditions (between QFM and QFM+1), consistent with SSZ melting. Based on the observations and geochemical data for trace elements Ti, V, and Yb, we conclude that SSZ melting likely played a role in the history of at least some of the mantle peridotites of the LOC.

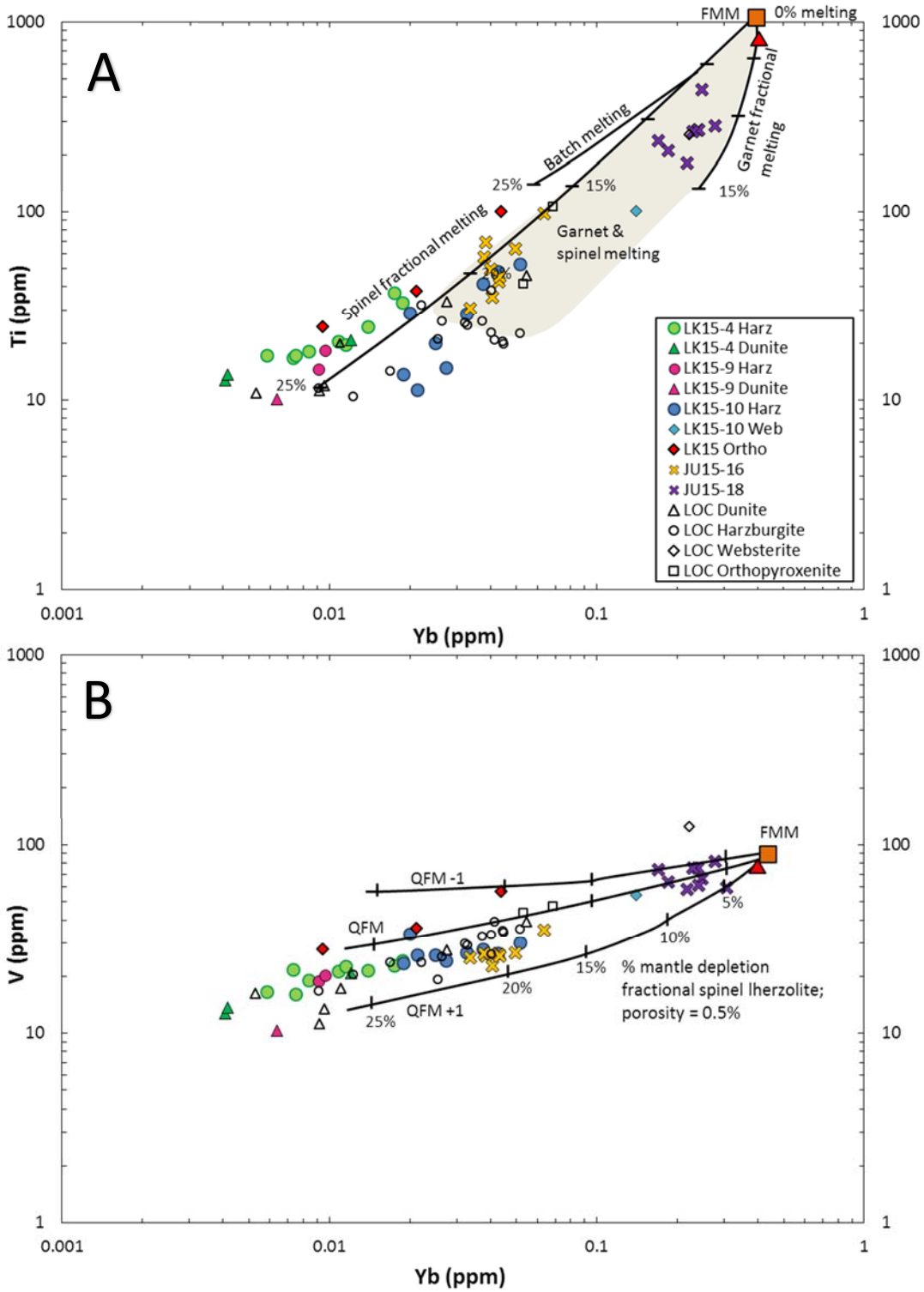

Figure 21. Plots of Ti vs Yb (A) and V vs Yb (B) for LOC peridotites and JOC serpentinites. Figure is adapted from O'Driscoll et al., 2015. (A) Batch and fractional melting curves are from Pearce & Parkinson (1993) and the shaded grey area is from Parkinson & Parkinson (1998) depicts melting in the presence of garnet. (B) The modelled melt extraction and oxygen fugacities (quartz-magnetite-fayalite (QFM) buffer) are from Pearce & Parkinson (1993) and Parkinson & Pearce (1998). The tick marks in both plot represent 5% melt removal increments. The theoretical composition of fertile MORB mantle is shown as FMM (Pearce & Parkinson, 1993). A calculated bulk value for DMM (Salters & Stracke, 2004) and data from a previous LOC study (O'Driscoll et al., 2015) are included for comparison, and are titled "LOC -".

5.1.2. HSE abundances

Before assessing the effects of mantle melt extraction on the absolute and relative abundances of HSE in LOC samples, it is important to determine whether serpentinization has modified the HSE. During serpentinization, absorption of large amounts of water causes density changes in peridotites and concurrent volume increases, which can cause dilution of HSE concentrations. However, several prior studies have concluded that the relative abundances of the HSE are little affected by processes involving aqueous fluids, including serpentinization (Rehkämper et al., 1999a; Büchl et al., 2002; Van Acken et al., 2008; and Liu et al., 2008). These studies have suggested that the stability results from the fact that the sulfide hosts of the HSE in peridotites tend to remain stable under the highly reducing conditions commonly associated with serpentinization evident in both abyssal and ophiolite peridotites (Snow & Reisberg, 1995; Snow and Schmidt, 1998; Liu et al., 2009; and Schulte et al., 2009).

Peridotites from the LOC exhibit low degrees of serpentinization when compared to mantle peridotites from many other ophiolite complexes (e.g., Jormua**; Fig. 22**), as well as abyssal peridotites. Leka ophiolite complex harzburgites and dunites typically contain abundant relict olivine grains (up to 60-70%) with only modest degrees of serpentinization. Furthermore, the HSE patterns of LOC harzburgites and dunites display no obvious trends that correlate with degree of serpentinization (e.g., HSE vs. bulk-rock LOI). However, on a plot of bulk-rock LOI vs initial $\gamma Os_{(497\ Ma)}$, values of LOC peridotites (**Fig. 23**) show a positive correlation ($R^2 = 0.71$), where all but one sample (LK15-4 A3 (Harz)) with bulk-rock LOI $\geq$ 9 wt%, have initial γOs values $\geq 1.3 \pm 0.2$, while peridotites with bulk-rock LOI $\leq$ 9 wt%, have initial γOs values $\leq 0.4 \pm 0.2$. This weak trend could indicate that LOC

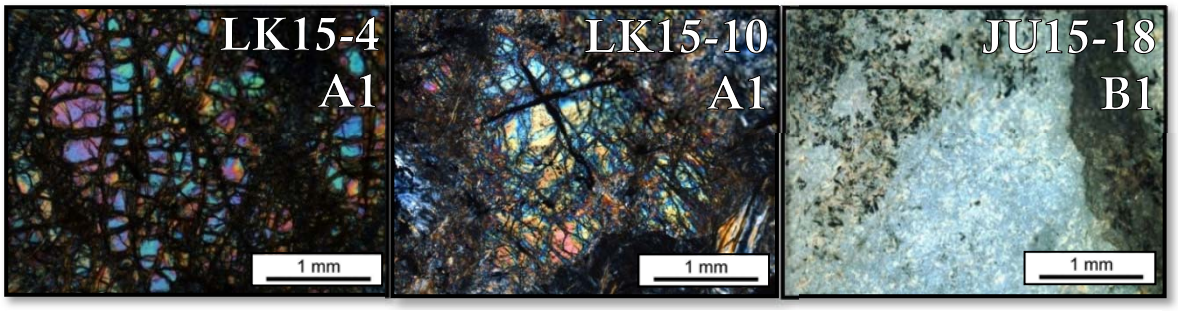

Figure 22. Thin section photo of olivines within LK15-4 A1 and LK15-10 A1 in cross polarized light. A thin section photo of highly serpentinized JU15-18 B1 from the JOC is shown for comparison.

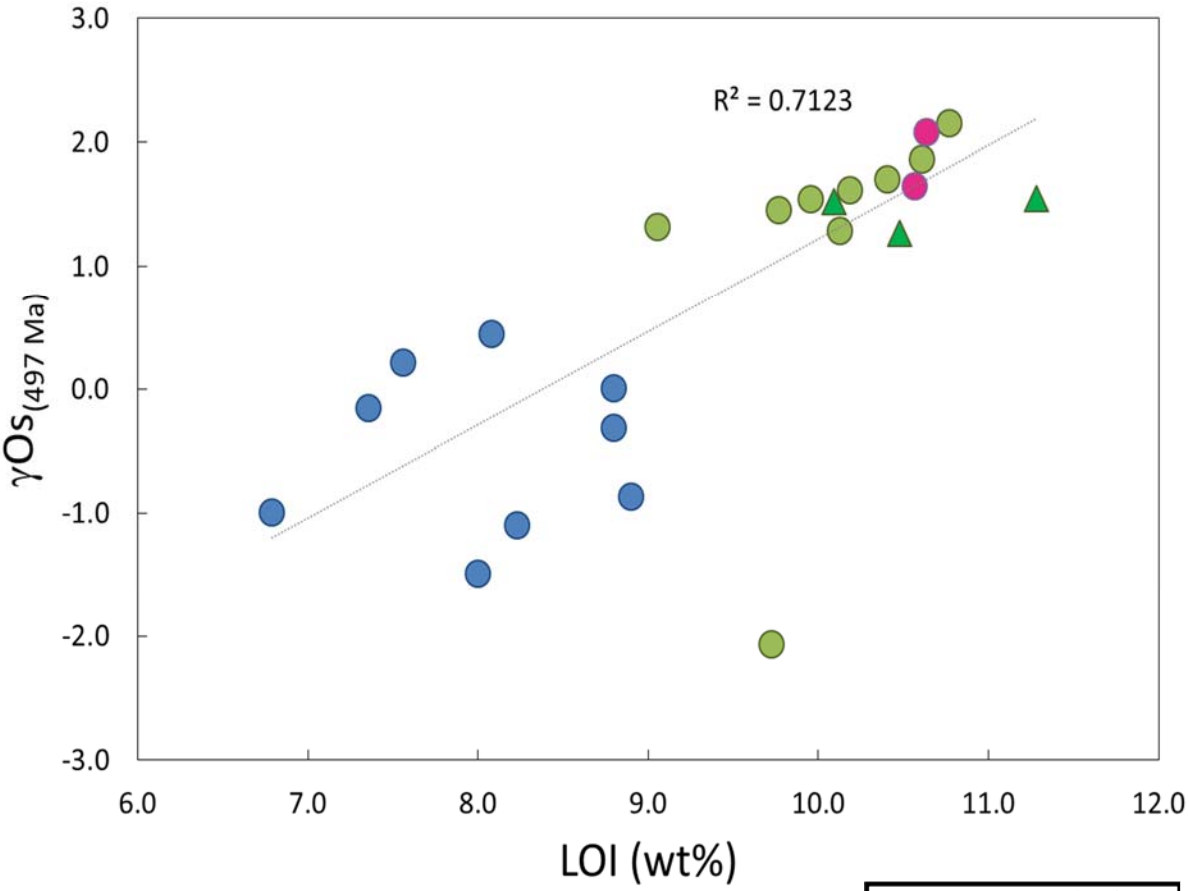

Figure 23. Plot of LOI vs initial γOs $_{(497\ Ma)}$ for LOC harzburgites and dunites. Uncertainties on γOs $_{(497\ Ma)}$ = ±0.2. The R^2 value is calculated using least-squares regression in Microsoft Excel.

samples with high bulk rock LOI (i.e., higher degrees of serpentinization), gained radiogenic Os during serpentinization, or via water-rock interactions with highly radiogenic seawater (Sharma et al., 1997; Levasseur et al., 1998; Burton et al., 1999; and Lassiter et al., 2014). Alternatively, this trend could simply reflect different serpentinization histories of two peridotite populations (LK15-4 and LK15-10) with different initial $\gamma Os_{(497\ Ma)}$. Seawater modification of Os isotopic compositions of peridotites is difficult to envision as LOC peridotites (~4 ppb) have much higher Os concentrations than seawater (8-10 fg/g; Sharma et al., 2000). In order to significantly elevate the $^{187}Os/^{188}Os$ ratios of LOC peridotites, the seawater/rock ratio must exceed ~100 (Büchl et al., 2002), which is not consistent with the low degree of serpentinization observed in LOC peridotites. In addition, bulk-rock LOI displays no obvious correlation with soluble minor or trace elements (e.g., Ba). Furthermore, data from previous studies on the LOC (O'Driscoll et al., 2015) do not show any obvious correlation between initial $\gamma Os_{(497\ Ma)}$ and LOI. Based on these observations, we conclude that the effects of serpentinization on the relative abundances of the HSE in LOC peridotites were minimal. The HSE concentrations and initial $\gamma Os_{(497\ Ma)}$ of these samples were either established in the mantle, or by processes other than serpentinization.

The relative HSE abundances in LOC harzburgite samples range from generally chondritic to variably depleted in the incompatible HSE (Pt, Pd, and Re) (**Fig. 13**). The types of HSE patterns present in these harzburgites are similar to those previously reported for LOC samples (O'Driscoll et al., 2015), and are also similar to harzburgites and lherzolites from the spatially and temporally associated Shetland Ophiolite Complex (SOC, O'Driscoll et al., 2012). The LOC harzburgite HSE patterns are also similar to those of

harzburgites from younger ophiolites including the ~90 Ma Troodos ophiolite, Cyprus (Büchl et al., 2002), and the ~6 Ma Taitio ophiolite, Chile (Schulte et al., 2009). Additionally, HSE patterns for LOC harzburgites resemble patterns commonly observed in abyssal peridotites (Liu et al., 2009), and harzburgites from orogenic massifs (e.g., Becker et al., 2006; Luguet et al., 2007; and Lorand et al., 2008).

Plots of Os/Ir, Ru/Ir, Pt/Ir, Pd/Ir, and Re/Ir versus Al_2O_3 (wt%, anhydrous corrected) for LOC harzburgites (**Fig. 24a,b,c,d,e**) examined by this study overlap with previously published data for the LOC (O'Driscoll et al., 2015) and show considerable overlap with peridotites from the Shetland (O'Driscoll et al., 2012) and Taitao (Schulte et al., 2009) ophiolites, as well as with abyssal peridotites from the Gakkel Ridge (Lui et al., 2009). The similarities between the HSE patterns of LOC peridotites and what is presumed to be oceanic mantle from different tectonic settings, suggests that overall HSE abundances of LOC harzburgites were unaffected by SSZ processes.

Plots of initial γOs vs Al_2O_3 (wt% anhydrous) (**Fig. 24f**) show that the Os isotopic compositions of LOC harzburgites fall within a range defined for the oceanic mantle by previous studies of ophiolite and abyssal peridotites. The average initial $\gamma Os_{(497\ Ma)}$ value for LOC harzburgites in this study of $+0.3 \pm 1.4$ (1σ SD, n =28) is nearly identical to the average initial $\gamma Os_{(497\ Ma)}$ value of LOC harzburgites reported by O'Driscoll et al. (2015) of $+0.2 \pm 2.0$ (n = 16). O'Driscoll et al. (2015) concluded that the harzburgitic rocks of the LOC appeared to be ~2% more radiogenic than estimates for modern oceanic mantle, based on a filtered (>2 ppb Os) global average for modern abyssal peridotites, and projected back to 497 Ma. Additionally, LOC harzburgites were also found to be more radiogenic than averaged harzburgite compositions from the Taitao ophiolite (-2.2 ± 2.4; n = 22; Schulte et

al., 2009) and Os-Ir-Ru alloy grains from the Josephine ophiolite (~-1.4 ± 6.5; n = 825; Meibom et al., 2002; Walker et al., 2005), but remarkably similar to other well-characterized ophiolites, including the SOC (-0.4 ± 2.4, n = 11; O'Driscoll et al., 2012) and Troodos (+0.3 ± 3.4, n = 14; Büchl et al., 2002; 2004). The offset in Os isotopic composition of previously studied LOC harzburgites was suggested to reflect a minor degree (~2%) of global-scale Os isotopic heterogeneity in the oceanic mantle, with SSZ processes having little effect on I-PGE and Os isotopic compositions (O'Driscoll et al., 2015). While the average initial $\gamma Os_{(497\ Ma)}$ values for the LOC in this study, broadly match values reported by previous studies, it is noteworthy that average initial $\gamma Os_{(497\ Ma)}$ values for individual grid sites differ significantly, implying that the Os isotopic composition of LOC peridotites in individual locations in the mantle may be a result of local (km) scale processes, rather than global-scale heterogeneity.

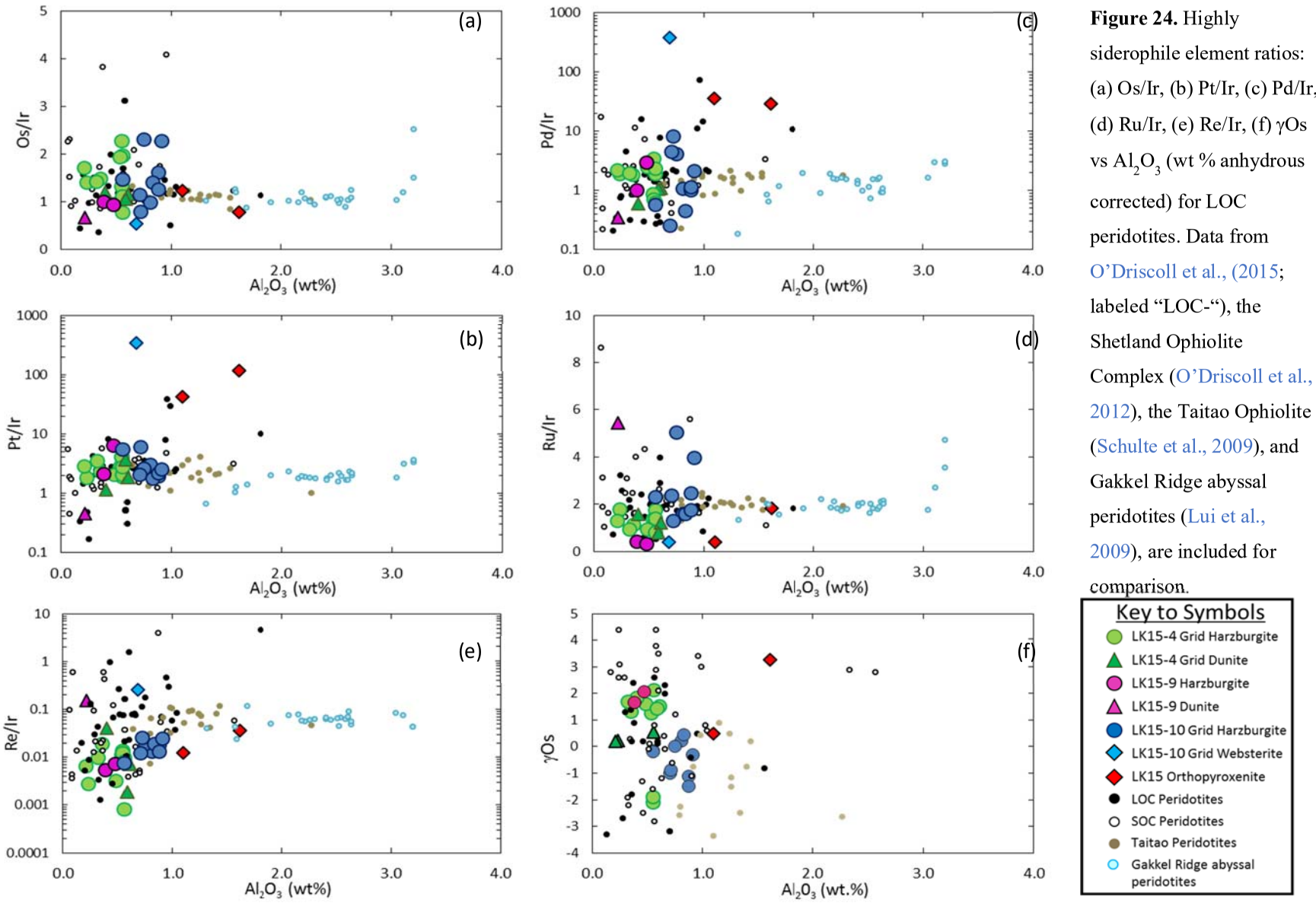

Figure 24. Highly siderophile element ratios: (a) Os/Ir, (b) Pt/Ir, (c) Pd/Ir, (d) Ru/Ir, (e) Re/Ir, (f) γOs vs Al_2O_3 (wt % anhydrous corrected) for LOC peridotites. Data from O'Driscoll et al., (2015; labeled "LOC-"), the Shetland Ophiolite Complex (O'Driscoll et al., 2012), the Taitao Ophiolite (Schulte et al., 2009), and Gakkel Ridge abyssal peridotites (Lui et al., 2009), are included for comparison.

5.1.3. Timing of melt depletion

A study of LOC harzburgites and dunites by O'Driscoll et al. (2015) reported a moderate spread in calculated initial Os isotopic compositions for the LOC suite. Initial $\gamma Os_{(497Ma)}$ values for LOC peridotites from this study and O'Driscoll et al. (2015) are shown in **Fig. 25**. Most of the samples have initial $\gamma Os_{(497Ma)}$ values similar to the chondritic reference at 497 Ma, suggestive of melt depletion around the time of ophiolite formation (~497 Ma). Averaged initial $\gamma Os_{(497Ma)}$ values for peridotites from grid locations LK15-4 (average $\gamma Os_{(497Ma)} = +1.3$) and LK15-10 (average $\gamma Os_{(497Ma)} = -0.4$), however, are distinct from each other. This observation may suggest a complex melting history for the LOC mantle section on a regional scale.

In some modern ophiolites, negative correlations of Os isotopic composition in WR samples and Mg# in olivine grains present in these rocks, and positive correlations of WR Os isotopic composition and Al_2O_3 (wt%, anhydrous), have suggested that Os isotopic compositions reflect primary Re/Os fractionation in the mantle by variable extents of partial melting at one time (i.e., Taitao ophiolite complex, Schulte et al., 2009). A plot of whole rock $\gamma Os_{(497\ Ma)}$ versus olivine Mg# (**Fig. 25A**), reveals a broad correlation for peridotites from the LK15-4 and LK15-10 locales ($r^2 = 0.42$, omitting sample LK15-4 A3 (Harz)), and shows that all but one of the samples (LK15-4 A3 (Harz)), with high Mg#, have lower initial $\gamma Os_{(497\ Ma)}$ values. This negative correlation could suggest that variability in the Os isotopic compositions of LOC peridotites are reflective of primary Re/Os fractionation (similar to the Taitao complex). However, LK15-4 and LK15-10 grid samples are distinct, and do not individually define good correlations. Furthermore, LOC samples are characterized by a broad negative correlation between WR initial $\gamma Os_{(497\ Ma)}$ values and

Al_2O_3 (a common indicator of melt depletion), unlike the broad positive correlations present in Taitao samples (**Fig. 25B**). However, similar to the trends presented in **Fig. 25A**, LK15-4 and LK15-10 grid samples are distinct, and do not individually define good correlations. These observations more likely imply modification of the Os isotopic composition of the LOC peridotites at these grid locations post melt depletion, or that melt depletion occurred just prior to ophiolite formation, so no systematic changes in Os isotopic composition accompanied changes in Re/Os.

Rhenium-depletion (T_{RD}) model ages of LOC peridotites show Re-depletion in some LOC peridotites occurred at least 500 Ma prior to the accepted age of the ophiolite (**Table 4**), which is significantly less time than the ~6 Ma Taitao ophiolite, which showed evidence for melt depletion ~1.6 Ga, before the formation of that ophiolite. We conclude, based on plots of WR initial γOs vs Mg# (olivine) and WR Al_2O_3 that, unlike for Taitao (Schulte et al., 2009), the Os isotopic compositions of LOC samples are not dominated by a single, ancient melting event.

Assuming the olivines in these samples are primary, their Mg# also suggest that LK15-10 samples experienced higher degrees of melt depletion, relative to LK15-4 samples. This is contrary to whole-rock major (**Fig. 10**) and trace element data (**Fig. 21**), which show evidence for higher degrees of melt-depletion in LK15-4 samples, relative to LK15-10. This difference could imply that the WR major and trace element compositions of LK15-10 samples were later enriched by a process following initial melt depletion (e.g., metasomatism), while the olivine compositions remained essentially unaffected. An alternative is that the melt processes which affected Al_2O_3 (hosted mainly by spinel and pyroxenes) and trace elements in LK15-4 peridotites had little effect on the Mg# of the

olivines. A third alternative is that, the olivines present in LOC rocks are not primary, and were formed during a later process. LOC olivines are characterized by low concentrations of CaO (~0.01 wt%), typical of metamorphic olivines (Evans and Trommsdorff, 1974). However, LOC olivines do not have the typical features of recrystallized olivine (e.g., inclusion of secondary minerals, dendritic crystals, clusters of subhedral–euhedral crystals, and randomly oriented crystals). While the compositions of olivines vary from rock to rock due to variable degrees of melt-depletion, concentrations of FeO and MnO for olivines are distinct between harzburgite samples from the LK15-4 and LK15-10 grid sites. Average FeO and MnO (wt%; 2SD) for LK15-4 olivines are 8.5 (±0.4) and 0.12 (±0.01), respectively. By comparison, average FeO and MnO (wt%; 2SD) for LK15-10 olivines are 7.8 (±0.8) and 0.25 (±0.12), respectively. Low abundances of FeO and high concentrations of MnO in LK15-10 olivines, relative to LK15-4 olivines, is consistent with serpentinized olivines (Evans and Trommsdorff, 1974; Trommsdorff et al., 1998). These observations may indicate the compositions of LK15-10 olivines were altered by secondary processes.

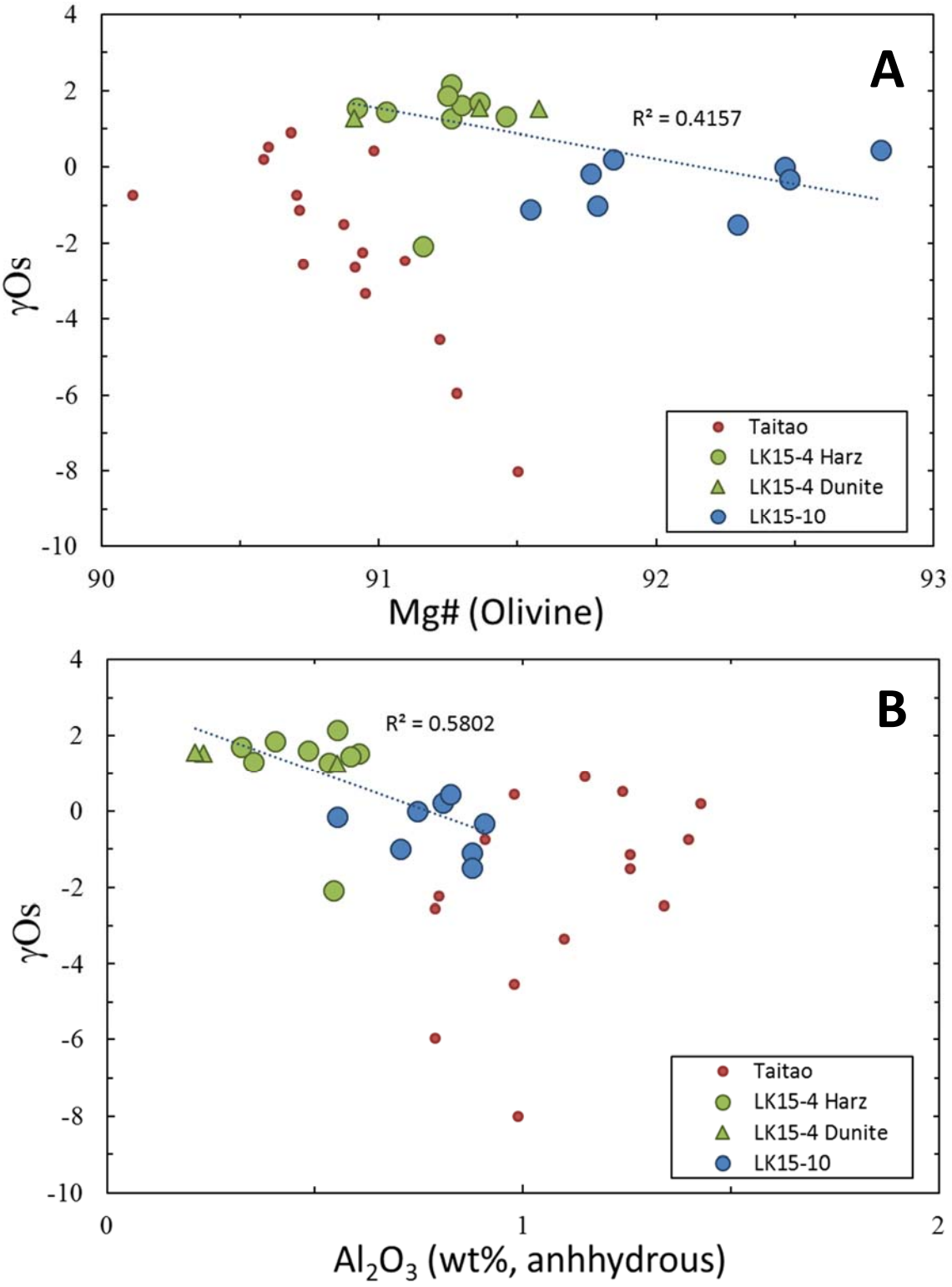

Figure 25. Plot of initial γOs $_{(497\ Ma)}$ values vs Mg# in relict olivine grains (**A**) and Al_2O_3 (wt%, anhydrous; **B**) for LOC harzburgites. Taitao ophiolite data shown for comparison (Schulte et al., 2009). The R^2 values are calculated using least-squares regression in Microsoft Excel.

The initial $\gamma Os_{(497\ Ma)}$ value of one harzburgite sample, LK15-4 A3 (Harz) (γOs = -2.0; based on repeat analyses; n = 3), in the Kvaløya-moen area of the NW portion of Leka, differs from adjacent harzburgites (average γOs = 1.6; n = 11). Additionally, the major and trace lithophile element data for LK15-4 A3 (Harz) are similar to those of adjacent samples, and show no obvious correlation with typical indicators of melt depletion (**Fig. 25**). The depleted Os isotopic composition of LK15-4 A3 (Harz) suggests ancient melt depletion with long-term lowered Re/Os ratios. Re-depletion model ages (T_{RD}) for LOC samples are calculated using **Eq. 1**, with the eruption age (EA) representing the $^{187}Os/^{188}Os$ ratio at the time of the accepted age of the ophiolite (~497 Ma). The calculated T_{RD} model age of the average for this sample is ~1.0 Ga, or ~500 Ma prior to ophiolite formation. Three previously studied LOC harzburgites (one from the Kvaløya Moho locality and two from Kvaløya-moen) and one dunite (from below the petrological Moho, SE of Kvaløya),

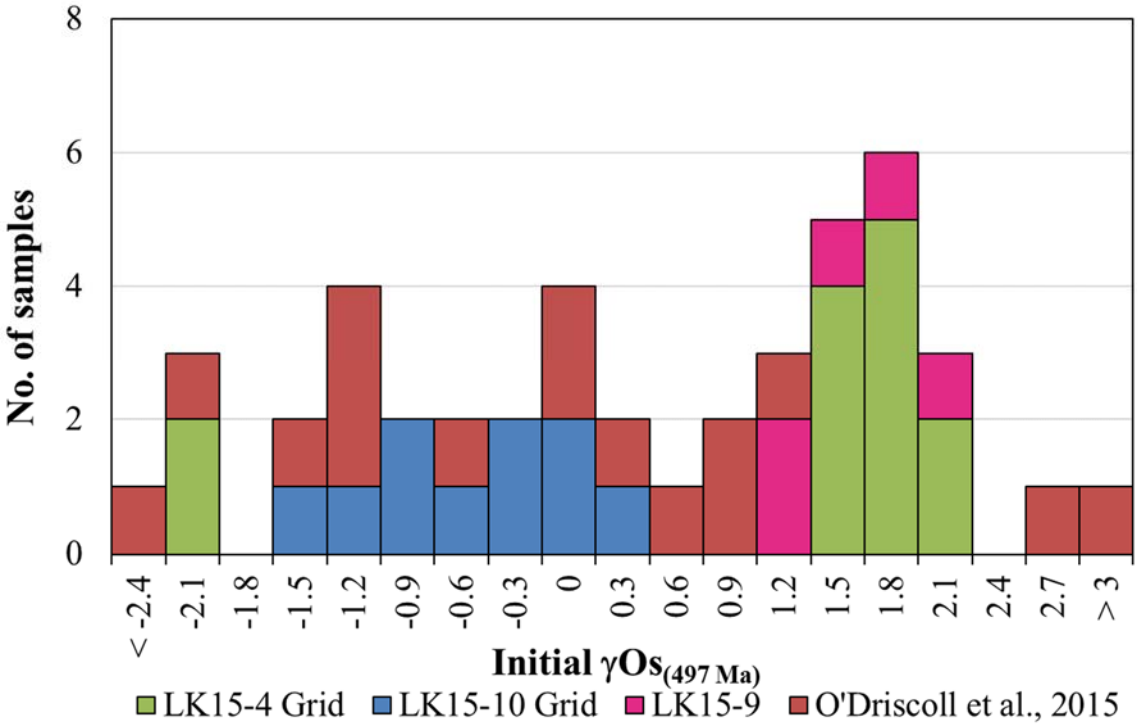

Figure 26. Histogram illustrating the distribution of initial $\gamma Os_{(497\ Ma)}$ values of LOC harzburgites (including replicates), including data from O'Driscoll et al., 2015 (n=15).

reported by O'Driscoll et al., (2015), also yield T_{RD} model ages of ~0.8 to 1.0 Ga. The depleted Os isotopic compositions in these samples provide evidence for the earliest stage of mantle melting recorded in the LOC, preceding ophiolite formation by as much as ~500 Ma. Additionally, the spatial distribution of these samples indicates that these ancient refractory domains are not restricted to a single location in the LOC mantle.

Previous studies of oceanic mantle materials show that samples with Os model ages ≥1 Ga older than the age of the ambient mantle, appear to be relatively common both regionally and globally. For example, some harzburgites from the nearby Shetland Ophiolite Complex (SOC; ~492 Ma) yield T_{RD} model ages of ~1.4 Ga (O'Driscoll et al., 2012). Globally, samples of peridotites and alloys from other ophiolites including the Taitao (Schulte et al., 2009), Troodos (Büchl et al. 2004), Oman (Hanghøjet al., 2010), and Josephine (Meibom et al., 2002) have yielded model ages extending back to the Archean. Ancient Os melt depletion ages have also been observed in abyssal and fore-arc peridotites (Parkinson et al., 1998; Esperanca et al., 1999; Brandon et al., 2000) as well as in oceanic mantle xenoliths from Hawaii (~2 Ga; Bizimis et al., 2007) and the Ontong Java Plateau (~1.7 Ga; Ishikawa et al., 2011). Collectively, these observations from the LOC and other mantle materials suggest that ancient refractory domains are a common feature in the oceanic mantle. The spatial constraints provided by grid sampling in this study, suggests that these domains are <1 m^3.

The Os isotope data for an LOC websterite LK15-10 Web, further support conclusions made by O'Driscoll et al., (2015) for at least one other major mantle melting event in the LOC suite. The trace element pattern (**Fig. 27**) and Os T_{MA} model ages of LK15-10 Web (T_{MA} = ~690 Ma), a ~0.5 m thick websterite dike within the LK15-10 grid square (**Fig.**

15B), broadly overlaps with the trace element pattern and T_{MA} model age of ~620 Ma presented by LK_12_14 (O'Driscoll et al., 2015), suggesting similar origins. For websterite samples, T_{MA} model ages are used because websterite samples do not have non-negligible concentrations of Re, and cannot be assumed to have lost all of their Re during melt depletion, unlike peridotites and mantle xenoliths with low Re/Os. This age broadly corresponds to the opening of the Iapetus Ocean (e.g., 620 – 550 Ma; Chew 1and Strachan, 2014).

Numerous samples in the LOC are characterized by modestly suprachondritic initial $\gamma Os_{(497Ma)}$ values, most notably samples from Kvaløya-moen, including grid location LK15-4 and sample LK15-9A (Average $\gamma Os_{(497\ Ma)} = +1.6$; n = 16). These suprachondritic initial γOs (497 Ma) values are either a result of primordial radiogenic heterogeneity, similar to conclusions by O'Driscoll et al. (2015), or a result of interaction with a more radiogenic Os melt (e.g., SSZ metasomatic processes, melt percolation, refertilization). As noted above, linear trends between Al_2O_3 vs Ti and V indicate that refertilization may have played a role in the history of LK15-4 grid samples, however, results presented in Section 5.2 suggest limited modification of Os isotopic composition by SSZ processes.

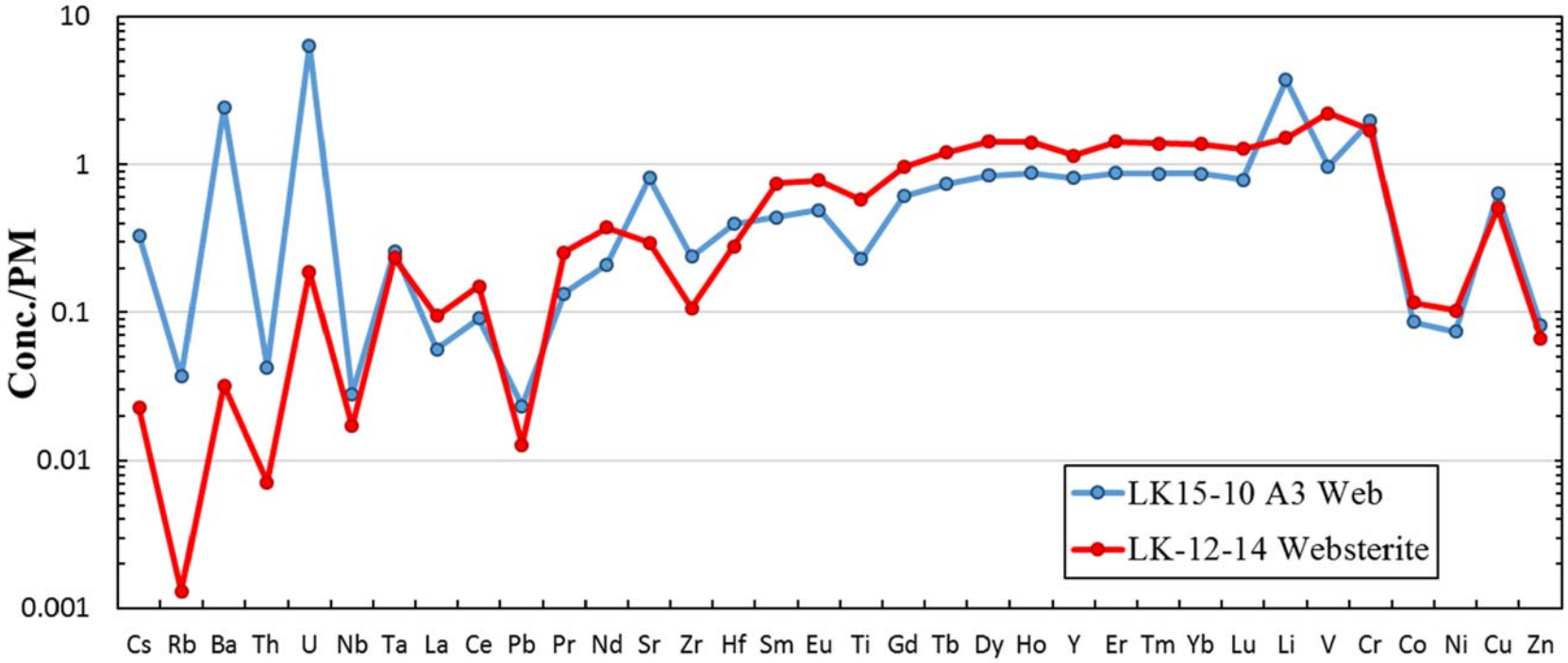

Figure 27. Primitive mantle normalized trace element patterns for LOC websterites. Sample LK-12-14 websterite is taken from O'Driscoll et al., 2015. Normalization values from McDonough & Sun (1995).

5.2. Small-scale heterogeneity in the LOC mantle

5.2.1. Cm-scale effects of orthopyroxenite veins in harzburgite

Based on field observations at Leka and the mapping of Maaløe (2005), orthopyroxenite comprises ~2–3 vol. % of the LOC mantle in the form of <1 cm veins to >1 m channels. The development of orthopyroxenite veins and channels is commonly attributed to reaction of peridotite with SiO_2-rich hydrous melts, derived from melting of eclogite or pyroxenite at moderate to high pressures (1–3.5 GPa and 1200–1550ºC; Kelemen, 1990). Orthopyroxene is produced by the reaction between olivine and siliceous melt at the higher H_2O activities typical of SSZ settings. As the melt intrudes, it equilibrates with the host peridotite, causing the magmas to become increasingly richer in silica, until they become saturated in orthopyroxene (Kelemen, 1990). Previous work by Rampone & Hofmann (2012) inferred that pyroxenite components are capable of inducing large isotopic changes on a local-scale in peridotites, based on observed Nd isotopic variations of pyroxenite bands in host peridotites from the External Liguride ophiolites, Italy (Rampone et al., 2011; Borghini et al., 2011; 2016).

Field-based and hand sample observations show that the harzburgite in grid square LK15-4 A3 (Harz), characterized by initial $\gamma Os_{(497\ Ma)} = -2.0$, hosts an orthopyroxenite vein (~1 cm thick), while other harzburgites in the LK15-4 grid are absent of any visible orthopyroxenite. It is important to assess whether the SSZ melt processes that formed the hosted orthopyroxenite vein also affected the geochemical and Os isotopic composition of its host harzburgite.

Analyses of harzburgite at ~1 cm intervals away from orthopyroxenite veins for LK15-4 A3 (Harz) and LK15-9A, show only small cm-scale Os isotopic variations in the harzburgite host rock (**Fig. 28**). Furthermore, major (e.g., Al_2O_3, SiO_2, and MgO), and

incompatible trace lithophile element (e.g., V, Ni, Co, Cr, REE) concentrations of the cm-subdivisions show no obvious correlation with distance from the orthopyroxenite vein (Supplementary Figures). The Os isotopic characteristics of the orthopyroxenites veins in LK15-4 A3 (Harz) and LK15-9A are characterized by more radiogenic compositions than the host harzburgite. The orthopyroxenite reaction products record the isotopic characteristics of the melt, or a mixture of the Os isotopic composition of the melt and its host harzburgite. Of greatest importance, the limited variations in isotopic and geochemical characteristics of harzburgite samples 1→ 6 cm away (**Fig. 28**), shows the reaction with the siliceous melt had limited effect on the host rock, even very close to the reaction zones.

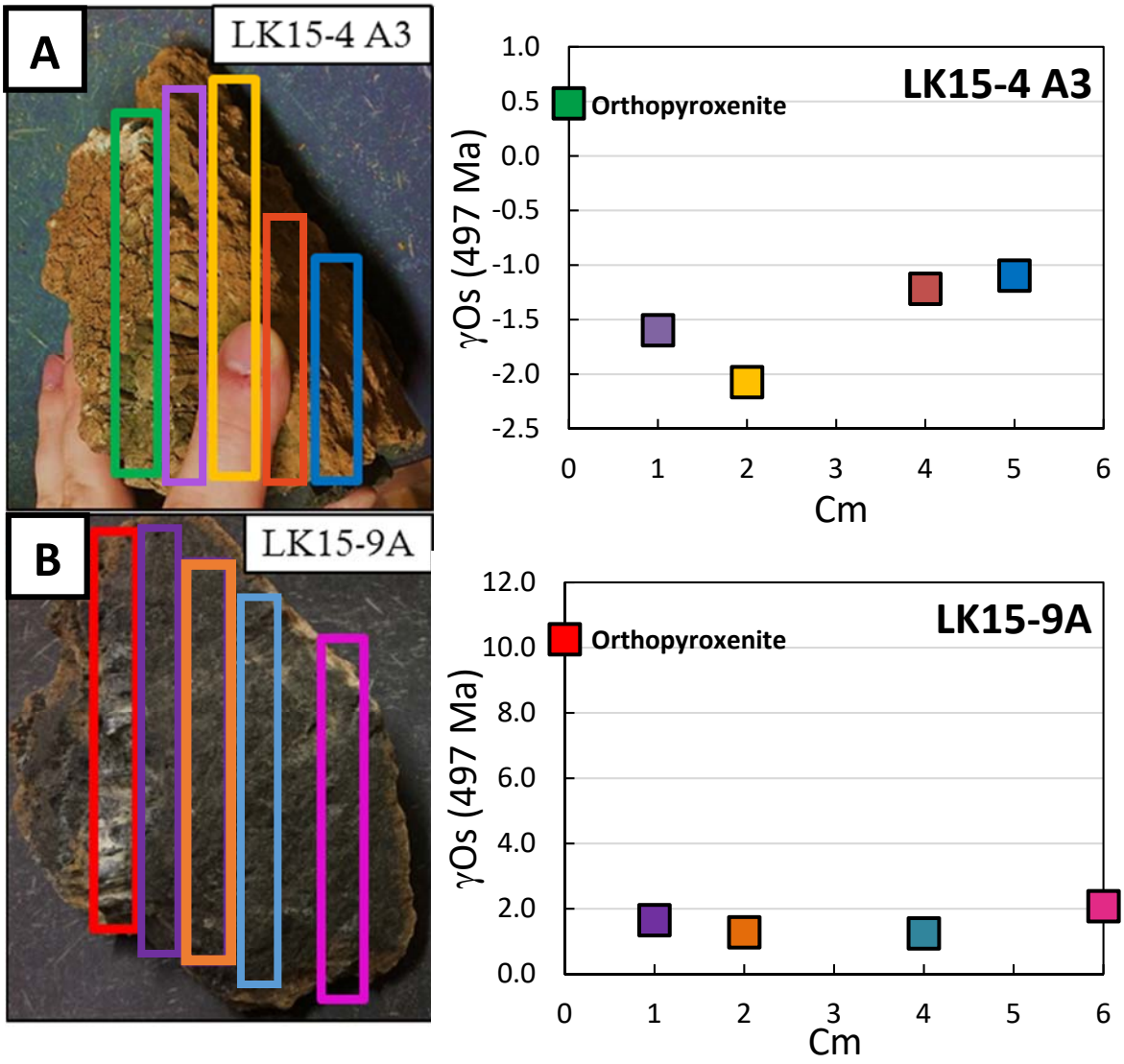

Figure 28. (right) γOs values of LOC orthopyroxenite (opx) bearing harzburgites. **A**. γOs values of LK15-4 A3 Harz subdivisions **B.** γOs values of LK15-9A subdivisions. Colored boxes on sample photos indicate the approximate location of the subdivision, and correspond to colored data points.

5.2.2. LK15-4 Grid

Major and trace element data, as well as Os isotopic compositions of LK15-4 grid harzburgites, show that these LOC peridotites are geochemically and isotopically similar (**Fig. 11A**; initial γOs = +1.3 to +2.2; excluding LK15-4 A3 (Harz)), at the meter scale, in the LOC mantle section at Kvaløya-moen. Initial $\gamma Os_{(497\ Ma)}$ values for most dunites and harzburgites collected within the same grid square are similar (**Fig. 15A**), within uncertainties (grid squares B1 and C3). However, the initial $\gamma Os_{(497\ Ma)}$ values of dunite within LK15-4 A3 (+1.5), is similar to most harzburgites from this grid, yet differs from the harzburgite collected in the same grid square (LK15-4 A3 (Harz); $\gamma Os_{(497Ma)}$ = -2.0). These observations indicate that the subchondritic, initial $\gamma Os_{(497\ Ma)}$ value of the LK15-4 A3 harzburgite, is not a result of interaction with the spatially associated dunite. It supports the concept that LK15-4 A3 (Harz) is a relic of an ancient melt depletion event. Dunites and harzburgites from grid squares of LK15-4 B1 and C3 are isotopically homogenous (**Fig. 15A**), as well as geochemically similar with comparable incompatible trace element concentrations and REE patterns (**Fig. 11A**). Dunite samples from grid squares A3 and C3 have comparatively flat HSE patterns that resemble harzburgite more than dunite, suggesting that these samples have inherited a harzburgite host-rock component. Examples of 'dunitized' harzburgite, that contain components of harzburgite host-rock, and dunites that have inherited a harzburgite component are common in the LOC (Maaløe, 2005; O'Driscoll et al., 2015).

Previous studies of LOC peridotites (O'Driscoll et al., 2015) observed that LOC dunites on average, are characterized by more radiogenic Os isotopic compositions than adjacent harzburgites. The similar Os isotopic compositions of adjacent dunites and harzburgites

within grid squares LK15-4 B1 and C3, coupled with similar incompatible trace element compositions, might also suggest that LK15-4 dunites inherited their host-harzburgite composition. Alternatively, dunites and harzburgites could have been homogenized during dunite/harzburgite formation, or during a later process. The relative LREE enrichments in some LK15-4 grid peridotites (A1, B3, and C3; **Fig. 11A**) suggest that these samples are not solely the result of melt depletion.

5.2.3. LK15-10 Grid

Within the LK15-10 grid suite, REE patterns (**Fig. 11B**) range from LREE-enriched (e.g., C3) to LREE-depleted (e.g., B2). Relative enrichments/depletions in LREE suggest that these samples are not solely the result of melt depletion. The REE patterns of some LK15-10 harzburgites instead likely reflect the product of variable interactions with a LREE-enriched melt (e.g., mafic melt), through metasomatism related to SZZ processes (Allégre & Turcotte, 1986; Snow et al., 1994; Sharma & Wasserburg, 1996; Liu et al., 2009; Warren et al., 2009). Previous studies of the Leka ophiolite complex by Furnes et al. (1992), showed that representatives of the first phases of magmatic development in the LOC (e.g., Island Arc Tholetiite (IAT) and metaboninites), displayed evidence of having been derived from a mantle source that may have been metasomatically contaminated by continentally-derived material during subduction related processes, based on similar Nd isotopic compositions. However, Nd isotopic compositions for LOC peridotites have not yet been studied to test this possibility with respect to these samples.

Initial γOs values (**Fig. 15B**) as well as incompatible trace element data (**Fig. 11B**) show modest meter scale heterogeneity between LK15-10 harzburgite samples. However, plots of REE ratios (e.g., La/Nd and La/Sm) vs Os isotopic composition (initial $\gamma Os_{(497\ Ma)}$) show no obvious correlations (Supplementary Figures). A previous study by Lorand et al. (2013), showed that metasomatic processes tend to strongly affect the P-PGE and can even modify the relative and absolute abundances of the I-PGE. Plots of Ir-normalized HSE concentrations vs Al_2O_3 (wt% anhydrous) (**Fig. 24**) show relative enrichments/depletions of Pd and Ru in LK15-10. However, similar to Os isotopic composition, HSE concentrations and ratios do not show any obvious correlations with REE ratios. This

implies that the processes responsible for modifying REE concentrations, are not likely responsible for the variations in HSE concentrations and in Os isotopic composition in LK15-10 samples.

The initial $\gamma Os_{(497\ Ma)}$ values for grid samples of LK15-10 harzburgite (**Fig. 15B**), do not show any spatial correlation with the suprachondritic Os (+6.3) websterite channel (LK15-10 Web), providing further evidence that pyroxenite formation (via SSZ metasomatic processes) does not affect the Os isotopic composition of adjacent harzburgites. We conclude, the variations in Os isotopic composition in LK15-10 samples reflect variable extents of partial melting at the meter-scale at some time prior to ophiolite formation.

6. Leka Summary

The excellent exposure of the mantle sections at the Leka ophiolite complex, provide an opportunity to study heterogeneities in the oceanic mantle at both the kilometer-scale, by sampling of different locations; to the small-scale, via meter-scale grid sampling and cm-subdivision of samples. By linking spatially controlled field-based observations of mantle samples, with petrologic and geochemical studies, we can assess the chemical structure of these oceanic mantle sections and the history of the processes that acted upon these rocks.

Grid sampling of two locations (LK15-4 and LK15-10) within the northern Leka harzburgite mantle section show kilometer-scale heterogeneity within the oceanic mantle as a result of variable melt-extraction as well as evidence of subsequent processes, which affected the geochemical and Os isotopic compositions of individual grid sites. The LK15-4 grid shows evidence high degrees of partial melting at shallow depths in the spinel stability field, as well as isotopic and geochemical homogenization of adjacent dunites and harzburgites. By comparison, the LK15-10 grid shows evidence for lower degrees of melt depletion at greater depths in the mantle where both garnet and spinel are stable. Rare earth element patterns and fractionation of HSE suggest that the LK15-10 grid location was subsequently affected by metasomatic processes. Both grid locations show that peridotites in the LOC are generally heterogeneous at the meter scale.

Similar to previous work on the LOC (O'Driscoll et al., 2015), ancient melt-depletion at (T_{RD}) ~ 1 Ga is captured in some LOC peridotites (e.g., LK15-4 A3 (Harz)). Grid sampling of adjacent harzburgites and dunites reveal that the geometry of these refractory domains can be constrained to be < 1 m^3.

The Os isotope data for an LOC websterite LK15-10 Web, further support conclusions made by O'Driscoll et al. (2015) for at least one other major mantle melting event in the LOC suite, T_{MA} = ~690 Ma. This age broadly corresponds to the opening of the Iapetus Ocean (e.g., 620 – 550 Myr; Chew and Strachan, 2014).

Two cm thick orthopyroxenite veins hosted by harzburgite near Kvaløya-moen, are more radiogenic than host harzburgites. The sharp gradations in initial $\gamma Os_{(497\ Ma)}$ values between the pyroxenites and harzburgites suggest vein formation had minimal impact on the Os isotopic characteristics of the host harzburgites.

Overall, the combined data set shows that the Paleozoic oceanic mantle represented in this suite of LOC peridotites, was affected by various processes, at different times. This cocktail of processes responsible for the geochemical and isotopic variations observed in these samples, is also likely manifested in the ambient, modern oceanic mantle.

7. Jormua Discussion

7.1. Melt depletion in JOC serpentinites

7.1.1. Major and trace element data

Similar to LOC peridotites, JOC serpentinites are characterized by low Al_2O_3 relative to estimates for the PM and DMM (**Fig. 10A**). The lower Al_2O_3 and higher MgO concentrations observed in JOC serpentinites are broadly consistent with a melt depletion history prior to ophiolite formation. However, while the concentrations of Al_2O_3 (anhydrous, wt%) between the two grid locations in the Antinmäki block (JU15-16 and JU15-18) are similar, serpentinites from the JU15-18 grid location show depletions in MgO relative to JU15-16 samples (~3 km away, **Fig. 4**). The depletions in MgO, yet similar ranges of Al_2O_3, suggest that the major element compositions of JU15-18 are not solely the result of melt depletion. Previous studies by Snow and Dick (1995), have suggested that high degrees of serpentinization, can result in major losses of Mg through the dissolution of brucite formed during serpentinization, and/or the direct incongruent dissolution of olivine and enstatite. While the JOC samples from both grid locations are heavily serpentinized and do not contain any relict olivine grains, the degree of serpentinization (e.g, bulk-rock LOI) are comparable between the two grids (JU15-16 and JU15-18; 11.0 to 11.4 wt%; respectively; Table 1). This observation could imply that the MgO depletions in JU15-18 samples are not solely caused by serpentinization.

On a plot of SiO_2 vs. MgO of JOC serpentinites (**Fig. 10B**) both JU15-16 and JU15-18 grid samples plot along a general melt depletion trend, consistent with data from other ophiolites (e.g. LOC and Taitao; O'Driscoll et al., 2015; Schulte et al., 2009) as well as abyssal peridotites (Brandon et al., 2000). Samples from the JU15-18 locale show strong positive correlations between SiO_2 and MgO ($R^2 = 0.98$). With the removal of one low

SiO_2 sample (JU15-16 B2), JU15-16 samples also show a positive correlation ($R^2 = 0.88$). These trends are consistent with removal of both SiO_2 and MgO, due to serpentinization (O'Hanley, 1996; Peltonen et al., 1998).

The JOC peridotites are also characterized by linear trends between some major and trace elements, such as Al_2O_3 vs V (**Fig. 19**). Serpentinites from grid locations JU15-16 and JU15-18 show positive correlations ($R^2 = 0.72$ and 0.50, respectively), although V concentrations of JU15-16 samples vary little, and the correlation for JU15-18 samples is weak. As noted above, such trends have been commonly attributed to variable extents of partial melting and refertilization (Azimow, 1999; Takazawa et al., 2000; Le Roux et al., 2007; Van Acken et al., 2008; Schulte et al., 2009). Evidence for refertilization in mantle rocks can include, linear trends between major elements (e.g., Mg or Al) and some minor elements (e.g., Ti) (Bodinier et al., 2008). Jormua samples from grid location JU15-16 show strong positive correlations between Al_2O_3 and Ti ($R^2 = 0.93$; **Fig. 20**), however the trend between MgO and Ti is weak ($R^2 = 0.38$; **Supplementary Figure**). The weak trends between MgO and Ti in JU15-16 grid samples could be the result of variable Mg loss during serpentinization. Samples from JU15-18 show no obvious correlation between Al_2O_3/MgO and Ti. We conclude, linear trends between Al_2O_3 and Ti, (possibly Al_2O_3 and V) indicate that refertilization may have played a role in the history of at least the JU15-16 serpentinites.

Plots of Ti vs. Yb and V vs. Yb for JOC serpentinites are shown in **Fig. 21A** and **21B**, respectively, to access the conditions of mantle melting. Bivariate plots of Ti vs. Yb have been demonstrated to be useful in assessing whether melting had occurred in the garnet-spinel stability field (Pearce & Parkinson, 1993). Bivariate plots of V vs. Yb have also been

used by Pearce & Parkinson (1993), as well as Parkinson & Pearce (1998), to assess oxygen fugacity conditions during mantle melting. Serpentinites from grid location JU15-16, show compositions that are typical for high degrees of melting (~20%) in the field that overlaps garnet and spinel stability. In addition, V and Yb concentrations suggest melting under relatively oxidizing conditions (between QFM and QFM+1), consistent with SSZ melting (O'Driscoll et al., 2015). By comparison, JU15-18 serpentinites show compositions consistent with lower degrees of melting (~5-12%), relative to JU15-16 samples. Bivariate plots of Ti vs. Yb suggest that JU15-18 samples also underwent melting in field that overlaps garnet and spinel stability, however, V vs. Yb compositions for samples in this grid site suggest melting under slightly more reducing conditions (between QFM-1 and QFM). Trace element data for V and Ti vs Yb, coupled with plots of MgO vs SiO_2 indicate that JU15-18 samples underwent much lower degrees of melt depletion, relative to JU15-16 samples, despite similar ranges of Al_2O_3 (anhydrous, wt%), a common indicator of melt depletion.

7.1.2. HSEs and Re-Os isotopic systematics

Primitive mantle-normalized HSE patterns of JU15-16 gird samples (**Fig. 16A**) show I-PGEs similar to PM values, although some samples are modestly enriched in Os, Ir, Ru, and Pt. All JU15-16 grid samples are characterized by depletions in Re. These depletions are characteristic of melt depletion, and consistent with the major and trace element evidence for prior melt depletion. The modest enrichments in some of the I-PGE may reflect primordial heterogeneity. By comparison, JU15-18 serpentinites show flat patterns across both the compatible I-PGEs (Os, Ir, Ru) and the moderately incompatible P-PGEs (Pt and Pd), as well as Re (**Fig. 16B**). These trends imply, that JU15-18 samples may have undergone low degrees of melt-extraction, consistent with the trace element evidence (**Fig. 21**).

Initial $\gamma Os_{(1.95\ Ga)}$ values for JU15-16 samples ranges from -3.0 to -0.5 and show very little variation (**Fig. 18A**) By comparison, JU15-18 samples show a much wider range of initial $\gamma Os_{(1.95\ Ga)}$ values, from -3.3 to +8.3 (**Fig. 18B**).

The initial Os isotopic compositions of JU15-16 samples are remarkably uniform. Plots of $^{187}Re/^{187}Os$ vs $^{187}Os/^{188}Os$ (**Fig. 17)** show that all JU15-16 samples have low Re/Os. The Re-Os systematics of these samples suggest they sample a subchondritic mantle, possibly representing the oceanic mantle at 1.95 Ga.

By comparison, samples from grid JU15-18, broadly plot along a reference isochron (**Fig. 17**), implying that the Re-Os isotopic ratios present in these samples are the result of variable Re/Os fractionation, around the time of the accepted age of the ophiolite. The cause of such fractionation, could be magmatic. However, the Re/Os ratios present in JU15-18 samples have higher than normal Re/Os ratios for typical melt removal. Instead,

these samples could reflect Re addition/loss at 1.95 Ga. This is addressed in greater detail in section **7.1.3.** Also, some samples (JU15-18 B2, B3, C2, and C3) plot well above or below the reference isochron. This is suggestive of more recent Re movement, as is discussed further in section **7.1.4.**

7.1.3. Evidence for Re addition/loss at 1.95 Ga in JU15-18

The variations in Re-Os isotopic systematics of many of the JU15-18 samples (**Fig. 17**) appear to be the result of variable amounts of Re gain/loss around the time of the accepted age of the ophiolite. Previous studies of the JOC have hypothesized that black schists that encircle the JOC, as well as gabbros and basalts that are integral parts of the ophiolite, could be possible sources of Re addition in JOC peridotites (Tsuru et al., 2000). The Re concentrations of the schists range from 10 to 20 ppb (Geological Survey of Finland, unpublished data), while the basaltic rocks of the JOC have concentrations of 0.4 to 1.2 ppb (Tsuru et al., 2000). Peltonen et al. (1996; 1998) interpreted the LREE-enriched patterns of peridotites from the eastern (Antinmäki) block, to be a result of metasomatic processes associated with gabbroic and basaltic dykes that are present in the eastern block. Evidence for this process was most clearly found in Sm-Nd isotope data, where the initial $^{143}Nd/^{144}Nd$ ratios of these residual peridotite samples closely resembled those of the gabbroic and basaltic dykes (Peltonen et al., 1996; 1998). Rare earth element patterns of JU15-18 samples (**Fig. 11E**), also show relative enrichment in LREE, implying that these samples have been affected by metasomatism, possibly associated with the Proterozoic gabbros (**Fig. 4; map**). Light rare earth element-enriched serpentinites in other ophiolite complexes, have also been previously attributed to intraplate metasomatism, including the Fawakhir ophiolite, Egypt (Hamdy et al., 2011), implying these processes are relatively

common in ophiolite mantle sections. Uranium-lead (U-Pb) dating of zircons from gabbroic dikes in the JOC yield an age of 1953±2 Ma (Peltonen et al., 1996), which may coincide with the age of metasomatism for JU15-18 samples. We conclude that the observations of Re addition/loss around 1.95 Ga in JU15-18 serpentinites, could have been the result of metasomatic processes by spatially associated, Re-enriched gabbros.

7.1.4. Evidence for recent Re mobility in JU15-18

As noted above, most JU15-18 grid samples plot close to the 1.95 Ga chondritic reference isochron, implying variable amounts of Re gain/loss around the time of the accepted age of the ophiolite. However, some samples (e.g., JU15-18 B2, B3, C2, and C3), plot well off the 1.95 Ga chondritic reference isochron (**Fig. 17**). These samples define highly variable calculated initial γOs values, and are most likely the result of recent addition/loss of Re. **Figure 29**, adapted from Tsuru et al., (2000), displays the hypothetical effect of various processes on Re-Os isotopic systematics. Tsuru et al. (2000), described

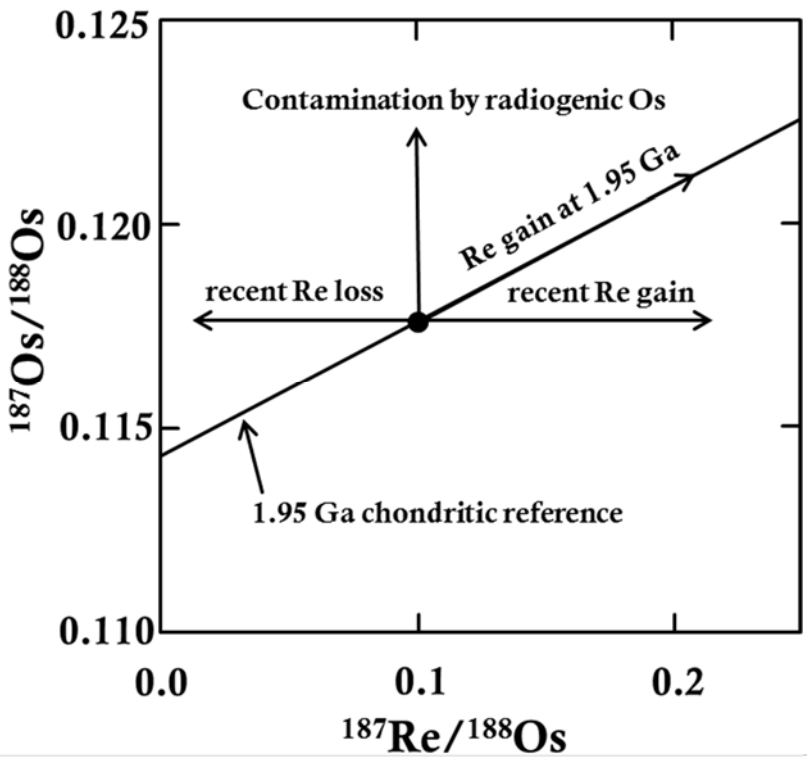

Figure 29. Adapted from Tsuru et al. (2000) showing the hypothetical effects of various processes on Re-Os isotope systematics. The closed circle shows a chondritic starting composition. Arrows define the vectors along which changes in isotopic composition and composition will take place.

weathering and ground water-rock interaction as the most likely process for Re mobilization. While there is no observed correlation between Os isotopic composition or Re vs. LOI (wt%), all of the samples that show evidence for Re-gain/loss (B2, B3, C2, and C3), have enriched Ba (a fluid mobile element; average $_{\text{B2, B3, C2, and C3}}$ = 10.8 ppb; n = 4), relative to other grid samples (average $_{\text{excluding B2, B3, C2, and C3}}$ = 1.1 ppb; n = 5) as well as minor enrichments in other fluid mobile elements (**Table 2; Fig. 30**; Harvey et al., 2006), including Sr. Enrichments in these fluid mobile elements may implicate water-rock interactions as a cause of recent Re mobilization in these JOC serpentinites. Furthermore, trace elements that are mobilized by silicate melts (e.g., Ta) show little variability between JU15-18 samples (**Fig. 11D and E**).

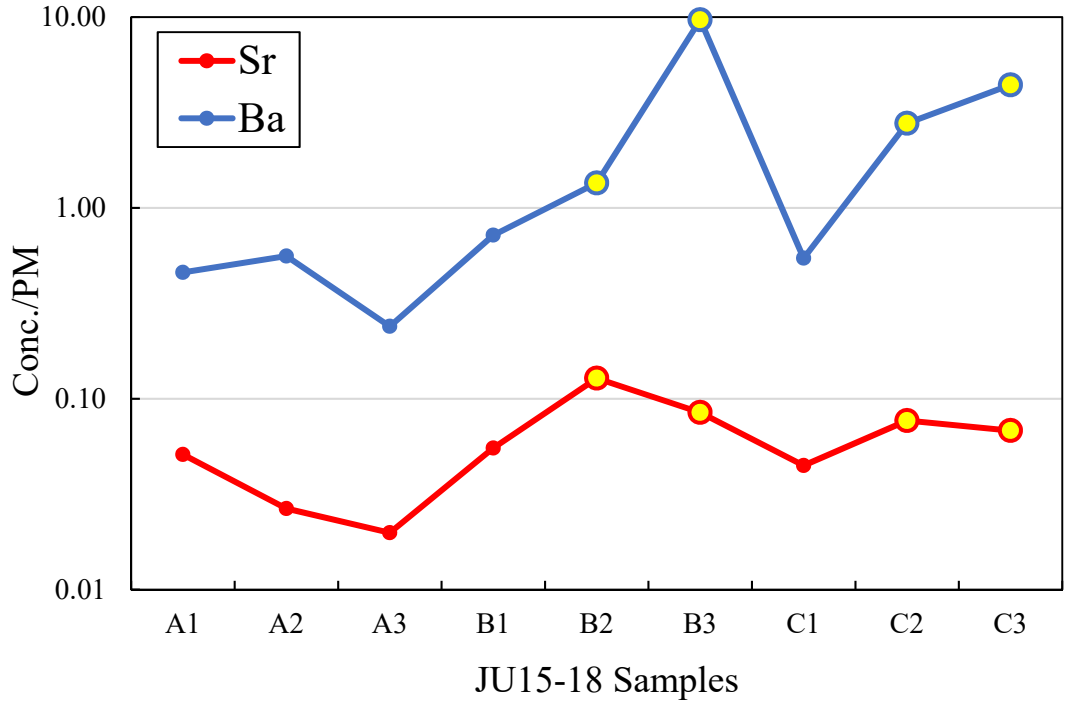

Figure 30. Primitive mantle normalized Sr and Ba for JU15-18 grid samples. Samples that show evidence for recent Re gain/loss are highlighted in yellow. Normalization values from McDonough & Sun (1995).

7.1.5. Timing of melt depletion in the JOC

The Re-depletion (T_{RD}) model ages of JOC serpentinites are calculated using the calculated initial $^{187}Os/^{188}Os$ ratio of the sample; at the time of ophiolite formation ~1.95 Ga) of JU15-16 serpentinites (T_{RD} ~ 2.0-2.4 Ga; **Table 4**), suggest that samples from this grid site experienced variable degrees of melt depletion up to 400 Ma prior to the accepted age of the ophiolite. Rhenium-loss during an early partial melting event would cause long-term lowered $^{187}Re/^{188}Os$ ratios, resulting in the subchondritic initial γOs values observed in JU15-16 samples. T_{RD} model ages for JU15-18 samples that plot near the reference isochron range from 1.8 to 2.4 Ga. Their average value (1.98 Ga; n = 5) is very similar to the chondritic reference, implying that none of these samples experienced substantial melt depletion prior to ophiolite formation. This is consistent with major and trace element data suggestive of low degrees of melt depletion (**Fig. 10; 21**).

7.2. Small-scale heterogeneity in the JOC mantle

7.2.1. JU15-16 Grid

Major and trace element data, as well as Os isotopic compositions of JU15-16 grid serpentinites, show that JOC samples from this grid location show modest geochemical (**Fig. 11D**) and isotopic heterogeneity (initial $\gamma Os_{(1.95\ Ga)}$ = -0.5 to -3.0; n = 9; **Fig. 18B**) at the meter scale in the eastern Antinmäki block. Geochemical and isotopic differences in JU15-16 samples, are likely the result of variable extents of melt depletion. Several elements (e.g., Cu) vary among samples from grid JU15-16. The cause of this is could be the result of incomplete homogenization of Cu-rich sulfides in JOC peridotites. Iridium-normalized HSE plots of JU15-16 samples, show fractionations between both the I-PGEs and P-PGE (**Fig. 31A-F**). While there are no obvious correlations between HSE concentrations and Cu (ppb), samples JU15-16 C1 and JU15-16 C2 have the highest Cu concentrations, as well as the highest concentration of Os.

The relatively flat-REE patterns of JU15-16 grid serpentinites (**Fig. 11D**) are similar to REE patterns of basaltic rocks of the Jormua complex (Peltonen et al., 1996; 1998). Peltonen et al. (1996) noted flat-REE patterns in peridotites, attributing them to infiltration by a relatively primitive basaltic melt. The samples from the JU15-16 grid site could be the result of similar processes as both sets of samples (this study and Peltonen et al., 1996) originate from the same eastern block, and have comparable REE patterns. However, the relative timing of this process remains unknown. Furthermore, the infiltration of this basaltic melt did not have any obvious effect on the Re composition of JU15-16 samples, unlike processes that affected JU15-18 samples.

7.2.2. JU15-18 Grid

Sample JU15-18 B2 (initial $\gamma Os_{(1.95\ Ga)} = +8.3$) shows enrichments in Ti, Zr, Nb, Hf, and Ta as well as relative depletions in Ni and Cu, compared to other JU15-18 serpentinites. The composition of sample JU15-18 B2 may reflect the presence of a chromite seam hosted within the analyzed serpentinite sample, most likely formed by fluid percolation along a fracture, resulting in the precipitation of phases enriched in Ti. Due to the significant chemical differences between B2 and the rest of the JU15-18 grid samples with respect to both trace element concentrations and Os isotopic compositions, we conclude that the composition of the analyzed powder for JU15-18 B2 is likely dominated by the chromite seam, rather than the host peridotite. Iridium-normalized HSE plots of JU15-18 samples (**Fig. 31A-F**), show less fraction between samples than JU15-16 samples, as well as small variation between Cu concentrations. This implies that Cu-rich sulfides hosting HSE concentrations in JOC peridotites are homogenized in JU15-18 samples, unlike JU15-16 grid samples.

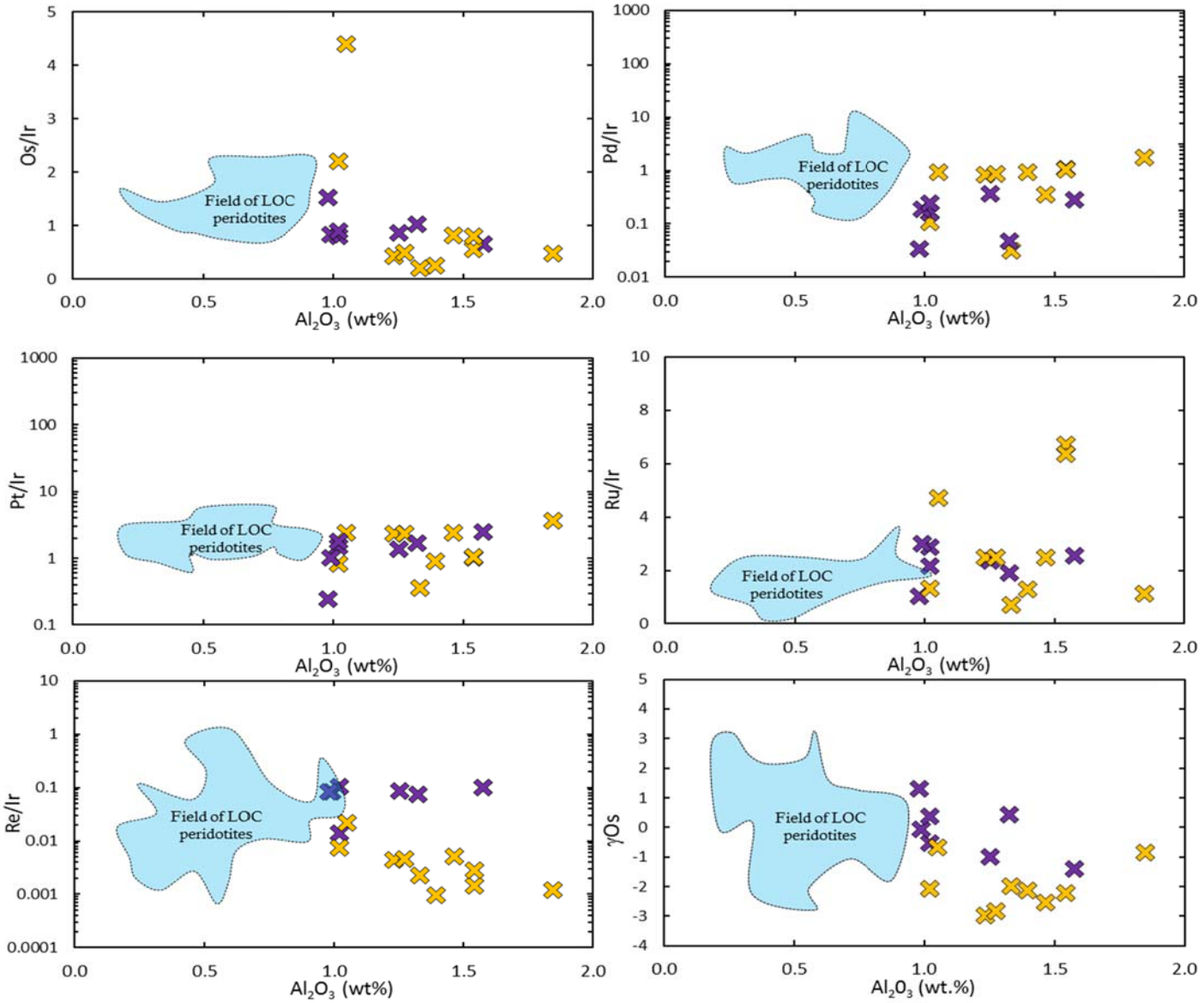

Figure 31. HSE ratios: (a) Os/Ir, (b) Pt/Ir, (c) Pd/Ir, (d) Ru/Ir, (e) Re/Ir, (f) γOs vs Al_2O_3 (wt % anhydrous corrected) for JOC peridotites. General fields of LOC peridotites are shown for comparison (This study & O'Driscoll et al., 2015). Symbols are the same as previous figures.

8. Jormua Summary

The Jormua ophiolite complex provides an opportunity to study oceanic mantle from the Proterozoic. Through systematic grid sampling techniques at different locations in the JOC, we were able to examine the processes responsible for oceanic mantle heterogeneity at both the meter and kilometer-scales. The JOC serpentinites are heavily altered, showing signs of Mg loss and possible SiO_2 loss by serpentinization. Grid samples of two locations (JU15-16 and JU15-18) within the eastern Antinmäki block of the JOC, show kilometer scale heterogeneity within the oceanic mantle, a result of variable melt-depletion at different times, as well as evidence of subsequent processes affecting the geochemical and Os isotopic composition of individual grid sites.

The JU15-16 grid, shows evidence of melt depletion as much as 400 Myr prior to the accepted age of the ophiolite (1953±2 Ma; Peltonen et al., 1996). JU15-16 grid serpentinites also show evidence of refertilization and infiltration by basaltic melts, based on trace element concentrations (V and Ti vs. Al_2O_3) and REE patterns. Overall, the JU15-16 grid shows modest geochemical and isotopic heterogeneity at the meter scale.

The JU15-18 grid, roughly 3 km away, shows evidence of Re addition/loss during the time of ophiolite formation via metasomatic processes, possibly related to spatially associated gabbros. Further evidence of metasomatic processes is indicated by LREE-enrichments comparable to those observed in the gabbros as well as other metasomatized JOC peridotites (Peltonen et al., 1996; 1998). Enrichments of fluid mobile elements in JU15-18 samples (e.g., Ba and Sr) are likely the result of ground water-rock interactions, causing recent Re loss and gain.

Overall, the combined data set shows that the Proterozoic oceanic mantle represented in this suite, is a complex set of serpentinites affected by various local scale processes, responsible for the geochemical and isotopic variations observed in these samples. Yet, it is remarkable that many isotopic and geochemical signatures survive processes such as, melt-extraction, alteration, melt-rock, and water-rock interactions over 2 billion years of Earth history.

9. Comparing the LOC and JOC

As a result of similar sampling and analytical methodologies, we are presented with a unique opportunity in this study to compare mantle materials from the Paleozoic and the Proterozoic. As a whole, it is noteworthy that in general, the geochemical and isotopic compositions of individual grids sites are a product of local scale processes such as, variable melt depletion (LOC and JOC), refertilization (JU15-16), metasomatic processes (LK15-10, JU15-18), water-rock interactions (JU15-18), as well as record evidence of melt depletion before the age of the ophiolite (LK15-10 Web, JU15-16, and LK15-4 A3 (Harz)).

In future sampling of ophiolite mantle sections, possible heterogeneities at different length scales should be taken into consideration. Kilometer-scale sampling of different areas in both the LOC and JOC shows that mantle sections of ophiolites can be heterogeneous with differing timing and intensity of prior-melt depletion, depths of melting, as well as different processes modifying local rocks in the same section. Comprehensive sampling of a single location, should not be extended to represent the entirety of the mantle section. Grid sampling methods can provide a more representative view of a sampling site, in that LOC peridotites and JOC serpentinites can be heterogeneous at the meter-scale, and individual samples are not always representative of an area (e.g., LK15-4 A3 Harz; JU15-18 B2). Additionally, grid sampling allows for pairing of field-based observations and geochemical analyses, to further investigate lithological interactions (LK15-4 and LK15-10). While grid sampling methods are useful for mapping meter-scale heterogeneities at these sites, laying out a 3m x 3m grid is not necessary for every sampling campaign. However, future sampling in ophiolite mantle sections should account for small-scale heterogeneities, to ensure representative sampling

of a site. Sampling of 4 to 5 rocks of a single lithology, within ~10m of each other, should be sufficient. Repeat analyses of LOC harzburgites and JOC serpentinites indicate that HSE can be heterogeneously distributed within a single sample powder, and between different 1cm cuts of a hand sample. Hand samples taken should be large enough for repeat analyses.

The northern harzburgite mantle section of the Leka ophiolite complex, is dominantly comprised of harzburgite followed by abundant dunite melt pods and channels. Leka ophiolite complex harzburgites host pyroxenites in the form of centimeter-thick veins to meter-thick dikes, and included orthopyroxenites and websterites. By comparison, the Proterozoic mantle section of the Jormua ophiolite complex, within the eastern Antinmäki block, is mostly comprised of serpentinized harzburgite, with spatially associated (E)-MORB sheeted dikes and gabbros. The extensive mapping and lithologic identification of the LOC is due to the excellent exposure of the ophiolite at Leka, Norway; compared to the JOC, which is far more concealed beneath vegetation. However, both ophiolites contain all of the principle components of a classic *Penrose* ophiolite sequence (**Fig. 2**).

Major (Al_2O_3 vs MgO; **Fig. 10A**) and trace element (V and Ti vs Yb; **Fig. 20 and 21**) plots of LOC peridotites and JOC serpentinites, show in general, LOC samples are more melt-depleted (>20%) than JOC samples (<20%) and appear less serpentinized in thin section analyses, further supported by the absence of relict olivine grains in JOC samples. However, it is noteworthy that the whole-rock LOI (wt%; a common indicator of degree of serpentinization) of LOC and JOC samples, are similar. While the average LOI for LOC samples (9.7 wt%; n = 41) is lower than the average LOI for JOC serpentinites (11.0 wt%; n = 18), many LOC peridotites have LOI values that fall within the range of values observed in JOC samples, yet do not show the same degree of alteration observed in thin

section analyses. There is considerable overlap between the major and trace element concentrations for the LOC and JOC, due to significant variation between individual samples, a result of local scale processes. However, there are overall concentration differences between the two ophiolites worth mention, including: SiO_2, Al_2O_3, MgO (**Fig. 10**).

Harzburgite samples from the LOC (LK15-10), and serpentinite samples from the JOC (JU15-16 and JU15-18), show evidence of crustal contamination based on flat to LREE-enriched REE patterns. Previous studies of the LOC (Furnes et al., 1992), and the JOC (Peltonen et al., 1996; 1998), showed Nd isotopic compositions consistent with metasomatic contamination by crustal-derived material. However, REE patterns in these LOC and JOC samples show no obvious correlation with HSE ratios and Os isotopic composition.

Similar to major and trace element concentrations, the concentrations of the HSE vary between samples for each ophiolite (**Table 4**). The LOC and JOC show differences between the average concentrations of Ru, Pt, Pd (LOC: 4.9, 9.3, and 6.0; respectively; n = 41) (JOC: 9.0, 5.5, and 2.9; respectively; n =26). Variations in Re between the two ophiolites are likely the result of primary (age of ophiolite) Re addition/loss and more recent Re mobilization (see JU15-18 discussion above). The average initial γOs values (calculated to the age of each ophiolite) show that the average initial $\gamma Os_{(497Ma)}$ for LOC peridotites in this study (+0.3 ± 1 (1σ SD); n =28), is more radiogenic, than the average initial $\gamma Os_{(1.95\ Ga)}$ for JOC serpentinites (-1.3 ± 3.2 (1σ SD); n = 27). The more radiogenic Os isotopic composition of the LOC, reflect a minor degree (~2%) of global-scale Os isotopic heterogeneity O'Driscoll et al. (2015).

The comprehensive analysis of portions of the LOC and JOC mantle sections in this study, provide an opportunity to investigate mantle heterogeneities at different length scales, during the Paleozoic and Proterozoic. The observations made in this study, highlight that the local scale processes and lithologic interactions, that affect the geochemical and isotopic compositions of ophiolite mantle samples, require further investigation.

Appendix A:

Tables

by

Mitchell B. Haller

Table 1: Major element abundances for LOC peridotites and pyroxenites (reported in wt%).

Grid	LK15-4	LK15-4	LK15-4	LK15-4	LK15-4	LK15-4	LK15-4	LK15-4	LK15-4	LK15-4	LK15-4
Sample:	A1 Harz	A2 Harz	A3 Dunite	A3 Harz	B1 Dunite	B1 Harz	B2 Harz	B3 Harz	C1 Harz	C2 Harz	C3 Dun/Harz
SiO_2	43.4	43.3	41.8	42.1	40.1	42.1	43.0	43.1	42.9	42.8	42.9
TiO_2	0.01	<0.01	<0.01	0.01	<0.01	0.01	0.01	0.01	<0.01	<0.01	<0.01
Al_2O_3	0.55	0.53	0.23	0.54	0.21	0.35	0.48	0.60	0.40	0.32	0.55
$Fe_2O_3^T$	8.6	8.9	8.9	9.4	9.7	9.2	9.2	9.3	9.0	8.9	8.9
MnO	0.13	0.14	0.13	0.13	0.12	0.13	0.12	0.14	0.13	0.13	0.13
MgO	45.5	45.0	47.3	45.6	48.2	46.3	45.2	44.7	45.6	45.9	45.5
CaO	0.68	0.64	0.11	0.54	0.03	0.43	0.52	0.83	0.49	0.41	0.50
Na_2O	0.02	0.02	0.02	0.08	0.02	0.01	0.02	0.04	0.02	0.01	0.08
K_2O	<0.01	<0.01	<0.01	0.01	<0.01	<0.01	<0.01	0.01	<0.01	<0.01	0.01
P_2O_5	<0.01	<0.01	<0.01	<0.01	<0.01	<0.01	<0.01	<0.01	<0.01	<0.01	<0.01
LOI	10.8	10.1	10.1	9.7	11.3	9.1	10.2	10.0	10.6	10.4	10.5
Total	98.8	98.5	98.5	98.4	98.4	98.5	98.5	98.8	98.5	98.5	98.6
Mg#	91.7	91.4	91.7	91.0	91.2	91.3	91.1	90.9	91.4	91.5	91.4

Grid	LK15-4	LK15-10	LK15-10	LK15-10	LK15-10	LK15-10	LK15-10	LK15-10	LK15-10	LK15-10	LK15-10
Sample:	C3 Harz	A1 Harz	A2 Harz	A3 Harz	A3 Web	B1 Harz	B2 Harz	B3 Harz	C1 Harz	C2 Harz	C3 Harz
SiO_2	43.1	42.8	43.9	43.2	49.3	42.5	44.0	42.3	43.4	43.7	43.9
TiO_2	0.01	0.01	0.01	0.01	0.02	<0.01	0.02	<0.01	0.01	0.01	0.01
Al_2O_3	0.58	0.80	0.87	0.74	0.68	0.70	0.82	0.55	0.87	0.71	0.90
$Fe_2O_3^T$	9.3	8.6	7.9	8.9	5.8	8.7	7.6	9.7	8.8	8.1	8.0
MnO	0.14	0.13	0.13	0.12	0.08	0.14	0.13	0.14	0.15	0.14	0.18
MgO	45.0	45.5	45.3	45.8	24.8	44.6	43.6	45.7	44.3	44.3	45.3
CaO	0.45	1.13	0.86	0.47	18.4	2.33	2.68	0.73	1.50	2.00	0.76
Na_2O	0.11	0.03	0.08	0.02	0.05	0.03	0.02	0.04	0.02	0.02	0.02
K_2O	0.01	<0.01	0.04	<0.01	0.01	<0.01	<0.01	<0.01	<0.01	<0.01	<0.01
P_2O_5	<0.01	<0.01	<0.01	<0.01	<0.01	<0.01	<0.01	<0.01	<0.01	<0.01	<0.01
LOI	9.8	7.6	8.2	8.8	3.5	6.8	8.1	7.4	8.0	8.9	8.8
Total	98.7	98.9	99.0	99.2	99.2	99.0	99.0	99.1	99.0	98.9	99.0
Mg#	91.0	91.7	92.3	91.5	89.9	91.5	92.3	90.8	91.3	91.9	92.2

Grid	LK15-4	LK15-4	LK15-4	LK15-4	LK15-9	LK15-9	LK15-9	LK15-9	LK15-9	LK15-9
Sample:	A3(1) Harz	A3(2) Ortho	A3(3) Harz	A3(4) Harz	A(1) Ortho	A(2) Harz	A(3) Harz	A(4) Harz	A(5) Harz	C Dunite
SiO_2	42.7	46.1	42.6	42.9	46.5	42.6	43.4	43.4	43.91	40.6
TiO_2	<0.01	<0.01	<0.01	<0.01	<0.01	<0.01	<0.01	<0.01	<0.01	0.02
Al_2O_3	0.55	1.09	0.49	0.58	0.60	0.38	0.34	0.47	0.49	0.22
$Fe_2O_3^T$	9.3	7.4	9.3	9.2	8.0	9.6	9.2	8.8	8.4	9.5
MnO	0.13	0.10	0.14	0.16	0.08	0.14	0.16	0.13	0.13	0.13
MgO	46.0	42.7	45.4	45.4	43.2	45.9	45.5	45.7	45.1	48.4
CaO	0.49	1.22	0.42	0.49	0.38	0.22	0.21	0.46	0.54	0.07
Na_2O	0.08	0.16	0.09	0.11	0.04	0.04	0.04	0.03	0.04	0.04
K_2O	<0.01	0.01	<0.01	<0.01	<0.01	<0.01	<0.01	<0.01	<0.01	<0.01
P_2O_5	<0.01	0.01	<0.01	<0.01	0.01	<0.01	<0.01	<0.01	<0.01	<0.01
LOI	9.5	10.7	9.5	9.8	11.8	10.6	10.4	10.6	11.1	10.4
Total	99.3	98.8	99.0	98.8	98.8	98.9	98.8	99.0	98.6	99.1
Mg#	91.2	92.3	91.2	91.4	91.8	90.9	91.2	91.6	91.8	91.4

Table 1: Major element abundances for LOC and JOC peridotites and pyroxenites (reported in wt%).

Grid	LK15-3	LK15-3	LK15-3	LK15-3	LK15-3	LK15-3	LK15-3	LK15-3	LK15-3	LK15-3
Sample:	Ortho	A1 Harz	A2 Harz	A3 Harz	B1 Harz	B2 Harz	B3 Harz	C1 Harz	C2 Harz	C3 Harz
SiO_2	47.2	44.3	43.3	43.2	43.9	43.5	42.9	44.0	44.0	44.1
TiO_2	<0.01	<0.01	<0.01	<0.01	<0.01	<0.01	<0.01	<0.01	<0.01	<0.01
Al_2O_3	1.60	0.87	0.70	0.80	1.08	0.58	0.78	0.72	1.01	0.91
$Fe_2O_3^T$	7.9	9.1	9.7	9.5	9.0	9.5	9.2	9.4	8.9	8.9
MnO	0.12	0.13	0.16	0.14	0.14	0.15	0.13	0.13	0.13	0.15
MgO	35.0	44.4	44.3	44.3	43.6	45.0	45.8	43.3	43.5	44.0
CaO	7.36	0.11	0.79	0.91	1.05	0.28	0.05	1.08	1.22	0.83
Na_2O	0.04	0.04	0.05	0.11	0.14	0.06	0.05	0.05	0.07	0.15
K_2O	<0.01	<0.01	<0.01	0.04	0.07	0.03	<0.01	<0.01	0.03	0.09
P_2O_5	<0.01	<0.01	<0.01	<0.01	<0.01	<0.01	<0.01	<0.01	<0.01	<0.01
LOI	8.2	11.4	10.3	9.0	9.4	10.0	10.1	9.6	9.2	9.6
Total	99.3	98.9	99.0	99.0	98.9	99.1	98.9	98.7	98.9	99.1
Mg#	90.2	91.1	90.5	90.6	91.0	90.8	91.3	90.6	91.1	91.1

Grid	JU15-16	JU15-16	JU15-16	JU15-16	JU15-16	JU15-16	JU15-16	JU15-16	JU15-16
Sample:	A1 Harz	A2 Harz	A3 Harz	B1 Harz	B2 Harz	B3 Harz	C1 Harz	C2 Harz	C3 Harz
SiO_2	44.0	45.7	45.3	44.1	43.2	44.5	44.7	44.2	44.3
TiO_2	<0.01	<0.01	0.02	<0.01	<0.01	<0.01	<0.01	<0.01	<0.01
Al_2O_3	1.38	1.53	1.83	1.22	1.26	1.45	1.01	1.04	1.32
$Fe_2O_3^T$	9.4	6.8	7.2	9.9	10.1	8.9	9.3	9.9	8.9
MnO	0.24	0.16	0.10	0.20	0.16	0.13	0.09	0.11	0.22
MgO	43.7	44.5	44.4	43.7	44.1	43.9	43.9	43.6	44.0
CaO	0.03	0.04	0.03	0.01	0.02	0.01	0.02	0.04	0.02
Na_2O	0.03	0.02	0.02	0.03	0.04	0.02	0.04	0.03	0.03
K_2O	<0.01	<0.01	<0.01	<0.01	<0.01	<0.01	<0.01	<0.01	<0.01
P_2O_5	0.01	0.01	<0.01	<0.01	<0.01	<0.01	<0.01	<0.01	<0.01
LOI	11.3	11.4	11.4	11.2	11.1	11.0	11.3	11.2	11.3
Total	98.8	98.7	98.9	99.1	98.8	98.9	99.0	98.8	98.8
Mg#	90.7	93.2	92.7	90.2	90.1	91.2	90.8	90.2	91.1

Grid	JU15-18	JU15-18	JU15-18	JU15-18	JU15-18	JU15-18	JU15-18	JU15-18	JU15-18
Sample:	A1 Harz	A2 Harz	A3 Harz	B1 Harz	B2 Harz	B3 Harz	C1 Web	C2 Harz	C3 Harz
SiO_2	46.6	45.9	46.1	47.0	45.4	46.6	46.1	46.7	46.6
TiO_2	0.02	0.03	0.03	0.02	2.27	0.02	0.06	0.02	0.03
Al_2O_3	1.01	1.93	1.56	0.98	1.01	1.24	1.31	0.97	1.21
$Fe_2O_3^T$	9.8	9.9	9.9	9.3	9.5	9.8	10.0	9.6	9.5
MnO	0.10	0.11	0.11	0.10	0.21	0.11	0.11	0.10	0.11
MgO	41.6	41.1	41.2	41.8	40.7	41.6	41.3	41.7	41.5
CaO	0.02	0.02	0.02	0.02	0.10	0.02	0.02	0.02	0.02
Na_2O	0.02	0.03	0.02	0.02	0.03	0.03	0.03	0.03	0.03
K_2O	<0.01	<0.01	<0.01	<0.01	<0.01	<0.01	<0.01	<0.01	<0.01
P_2O_5	<0.01	<0.01	<0.01	<0.01	<0.01	<0.01	<0.01	<0.01	<0.01
LOI	11.1	11.0	11.2	11.2	11.2	11.2	11.1	11.2	11.2
Total	99.2	99.0	99.0	99.3	99.2	99.3	99.0	99.0	98.9
Mg#	89.8	89.7	89.7	90.3	89.9	90.0	89.6	90.2	90.2

Table 2: Trace element abundances for selected Leka Ophiolite Complex peridotites (concentrations in ppm).

Grid Sample:	LK15-4 A1 Harz	LK15-4 A2 Harz	LK15-4 A3 Dunite	LK15-4 A3 Harz	LK15-4 B1 Dunite	LK15-4 B1 Harz	LK15-4 B2 Harz	LK15-4 B3 Harz	LK15-4 C1 Harz	LK15-4 C2 Harz	LK15-4 C3 Dun/Harz
Li	0.06	0.11	0.07	0.06	0.08	0.06	0.05	0.10	0.06	0.05	0.08
B	4.3	4.5	3.9	4.4	2.4	3.6	5.1	4.8	4.4	4.2	4.1
Sc	2.94	3.78	1.70	2.63	1.28	2.48	2.71	4.25	2.69	2.32	3.27
Ti	20.52	19.59	11.56	24.55	13.31	17.25	16.74	33.04	18.21	17.25	33.75
V	21.37	22.72	12.71	21.46	13.63	16.57	21.65	24.29	19.07	16.06	20.75
Cr	2784	2855	2407	2541	2809	2677	2619	2612	2971	2593	2330
Mn	662	814	793	775	752	841	753	874	808	773	759
Co	94.3	105.2	112.4	100.0	111.6	108.9	100.8	100.5	103.3	101.9	99.9
Ni	1989	2140	2260	2112	2449	2229	2105	2005	2156	2146	2051
Cu	1.1	1.0	1.8	0.7	3.4	3.7	1.8	0.9	0.8	4.2	2.3
Zn	37.0	43.3	40.5	39.0	45.4	42.8	40.5	39.1	40.2	40.2	37.3
Ga	0.49	0.48	0.26	0.48	0.32	0.36	0.43	0.51	0.41	0.36	0.49
Ge	0.76	0.83	0.80	0.80	0.88	0.82	0.79	0.81	0.85	0.87	0.80
Rb	0.276	0.061	0.018	0.309	0.017	0.036	0.053	0.264	0.035	0.032	0.282
Sr	0.561	0.346	0.149	0.192	0.235	0.193	0.316	0.445	0.415	0.232	0.256
Y	0.036	0.032	0.009	0.039	0.006	0.013	0.016	0.059	0.026	0.025	0.027
Zr	0.203	0.135	0.031	0.030	0.041	0.069	0.157	0.115	0.130	0.070	0.047
Nb	0.0137	0.0095	0.0035	0.0035	0.0044	0.0062	0.0095	0.0098	0.0092	0.0048	0.0044
Cs	0.0438	0.0386	0.0145	0.1608	0.0125	0.0240	0.0391	0.1017	0.0259	0.0350	0.1416
Ba	1.344	0.2871	0.0655	0.2545	0.2345	1.0874	1.480	25.29	2.338	0.5084	1.200
La	0.0387	0.0045	0.0010	0.0008	0.0023	0.0052	0.0016	0.0328	0.0032	0.0041	0.0123
Ce	0.0680	0.0094	0.0016	0.0018	0.0042	0.0106	0.0037	0.0481	0.0067	0.0079	0.0206
Pr	0.0082	0.0011	0.0003	0.0002	0.0006	0.0014	0.0005	0.0071	0.0009	0.0009	0.0023
Nd	0.0319	0.0046	0.0011	0.0014	0.0021	0.0050	0.0022	0.0288	0.0029	0.0036	0.0092
Sm	0.0051	0.0011	0.0003	0.0007	0.0004	0.0010	0.0007	0.0053	0.0008	0.0009	0.0014
Eu	0.0041	0.0004	0.0001	0.0003	0.0001	0.0004	0.0002	0.0016	0.0003	0.0003	0.0018
Gd	0.0053	0.0019	0.0007	0.0013	0.0004	0.0011	0.0010	0.0060	0.0012	0.0013	0.0016
Tb	0.0008	0.0004	0.0002	0.0004	0.0001	0.0002	0.0002	0.0011	0.0003	0.0003	0.0003
Dy	0.0057	0.0041	0.0015	0.0044	0.0006	0.0020	0.0025	0.0091	0.0028	0.0026	0.0036
Ho	0.0016	0.0013	0.0005	0.0016	0.0002	0.0006	0.0008	0.0026	0.0009	0.0009	0.0013
Er	0.0060	0.0058	0.0023	0.0070	0.0013	0.0028	0.0036	0.0103	0.0040	0.0034	0.0059
Tm	0.0012	0.0012	0.0005	0.0015	0.0004	0.0006	0.0008	0.0022	0.0009	0.0008	0.0013
Yb	0.0108	0.0115	0.0041	0.0139	0.0042	0.0058	0.0073	0.0188	0.0084	0.0075	0.0121
Lu	0.0022	0.0024	0.0009	0.0029	0.0011	0.0013	0.0016	0.0036	0.0017	0.0016	0.0026
Hf	0.0050	0.0038	0.0008	0.0010	0.0009	0.0018	0.0049	0.0034	0.0026	0.0017	0.0012
Ta	0.0015	0.0019	0.0013	0.0010	0.0012	0.0015	0.0015	0.0014	0.0015	0.0012	0.0011
W	0.0183	0.0169	0.0133	0.0137	0.0122	0.0124	0.0195	0.0183	0.0163	0.0148	0.0128
Pb	0.0483	0.0216	0.0180	0.0139	0.0077	0.0161	0.0154	0.0270	0.0314	0.0212	0.0299
Th	0.0020	0.0003	0.0002	<0.0001	0.0001	0.0001	<0.0001	0.0003	0.0006	0.0005	0.0004
U	0.0022	0.0022	0.0010	0.0011	0.0011	0.0016	0.0022	0.0056	0.0022	0.0014	0.0012

(continued)

Table 2: Continued

Grid Sample:	LK15-4 C3 Harz	LK15-10 A1 Harz	LK15-10 A2 Harz	LK15-10 A3 Harz	LK15-10 A3 Web	LK15-10 B1 Harz	LK15-10 B2 Harz	LK15-10 B3 Harz	LK15-10 C1 Harz	LK15-10 C2 Harz	LK15-10 C3 Harz
Li	0.98	0.58	0.62	0.55	5.61	0.87	1.17	0.69	0.60	0.99	0.51
B	4.9	21.8	25.2	27.1	13.6	17.0	23.8	15.7	21.0	23.7	23.7
Sc	11.23	8.81	9.62	8.50	38.78	9.07	13.01	8.50	8.64	9.54	8.31
Ti	37.32	14.82	41.51	29.10	101.23	11.33	52.91	13.71	20.11	48.37	28.80
V	22.92	24.26	27.78	33.61	54.39	25.94	30.22	23.59	25.96	26.41	26.73
Cr	2677	2423	2352	4091	5216	3555	2375	2865	3273	2669	3061
Mn	1021	939	925	864	734	1011	963	1047	1064	1014	896
Co	112.9	123.4	105.5	107.6	43.3	127.9	106.4	120.6	114.1	109.6	103.9
Ni	2109	2416	2420	2363	779	2370	2262	2458	2288	2193	2309
Cu	0.4	8.5	10.9	93.7	76.7	12.0	19.9	12.0	6.7	24.6	23.4
Zn	45.1	36.3	39.1	50.2	25.4	48.3	35.1	42.8	41.7	38.8	41.2
Ga	0.54	0.59	0.71	0.70	0.57	0.56	0.77	0.51	0.72	0.72	0.77
Ge	0.84	0.81	0.73	0.84	0.54	0.76	0.69	0.90	0.75	0.75	0.73
Rb	0.300	0.079	0.106	0.064	0.085	0.215	0.155	0.022	0.018	0.040	0.025
Sr	0.198	0.529	0.742	0.677	7.52	0.946	1.993	0.355	0.771	1.791	0.439
Y	0.047	0.118	0.233	0.113	1.27	0.091	0.373	0.073	0.146	0.285	0.187
Zr	0.028	0.278	1.720	0.936	0.909	0.897	3.101	0.802	1.101	1.510	1.164
Nb	0.0039	0.0129	0.0250	0.0148	0.0067	0.0078	0.0463	0.0052	0.0065	0.0230	0.0044
Cs	0.151	0.0303	0.0213	0.0193	0.0631	0.0282	0.0302	0.0225	0.0167	0.0150	0.0267
Ba	1.498	0.893	0.957	0.548	5.838	2.829	1.685	0.501	0.631	1.379	0.611
La	0.0025	0.0286	0.0375	0.0161	0.0134	0.0075	0.149	0.0042	0.0053	0.0555	0.0032
Ce	0.0031	0.0659	0.0883	0.0383	0.0561	0.0226	0.334	0.0105	0.0158	0.131	0.0102
Pr	0.0005	0.0093	0.0123	0.0053	0.0125	0.0025	0.0417	0.0012	0.0025	0.0170	0.0020
Nd	0.0018	0.0378	0.0581	0.0214	0.0968	0.0144	0.181	0.0091	0.0150	0.0733	0.0136
Sm	0.0005	0.0124	0.0146	0.0059	0.0655	0.0054	0.0382	0.0017	0.0073	0.0187	0.0070
Eu	0.0004	0.0050	0.0059	0.0025	0.0279	0.0039	0.0114	0.0024	0.0039	0.0071	0.0029
Gd	0.0011	0.0144	0.0249	0.0089	0.122	0.0066	0.0509	0.0046	0.0118	0.0297	0.0155
Tb	0.0004	0.0023	0.0044	0.0018	0.0267	0.0015	0.0071	0.0010	0.0028	0.0042	0.0029
Dy	0.0049	0.0163	0.0340	0.0166	0.208	0.0144	0.0562	0.0095	0.0202	0.0417	0.0239
Ho	0.0017	0.0044	0.0085	0.0039	0.0479	0.0032	0.0134	0.0022	0.0049	0.0099	0.0068
Er	0.0083	0.0157	0.0289	0.0156	0.140	0.0111	0.0420	0.0098	0.0171	0.0349	0.0230
Tm	0.0019	0.0027	0.0048	0.0023	0.0214	0.0021	0.0066	0.0018	0.0031	0.0057	0.0042
Yb	0.0175	0.0273	0.0375	0.0200	0.140	0.0213	0.0515	0.0188	0.0249	0.0427	0.0326
Lu	0.0035	0.0054	0.0063	0.0036	0.0201	0.0044	0.0080	0.0030	0.0042	0.0066	0.0054
Hf	0.0011	0.0094	0.0616	0.0334	0.0407	0.0354	0.116	0.0318	0.0447	0.0584	0.0480
Ta	0.0012	0.0038	0.0075	0.0061	0.0035	0.0062	0.0137	0.0062	0.0097	0.0076	0.0060
W	0.0125	0.213	0.170	0.128	0.790	0.212	0.210	0.134	0.211	0.259	0.150
Pb	0.0163	0.0676	0.0586	0.0440	0.0575	0.0606	0.0537	0.0290	0.0415	0.0490	0.0333
Th	<0.0001	0.0045	0.0132	0.0065	0.0060	0.0059	0.0403	0.0049	0.0050	0.0121	0.0053
U	0.0013	0.0017	0.0029	0.0012	0.0474	0.0007	0.0063	0.0004	0.0031	0.0022	0.0005

(continued)

Table 2: Continued

Grid Sample:	LK15-4 A3(1) Harz	LK15-4 A3(2) Ortho	LK15-4 A3(3) Harz	LK15-4 A3(4) Harz	LK15-9 A(1) Ortho	LK15-9 A(2) Harz	LK15-9 A(3) Harz	LK15-9 A(4) Harz	LK15-9 A(5) Harz	LK15-9 C Dunite
Li	0.49	1.71	0.66	0.56	0.21	0.62	1.36	0.38	0.15	1.46
B	3.0	6.3	2.5	2.9	5.3	3.5	2.1	3.3	2.8	2.0
Sc	5.06	9.60	4.08	4.69	7.15	5.43	6.30	4.45	3.12	3.62
Ti	23.65	38.15	18.10	22.45	24.41	14.43	12.68	18.24	17.71	10.10
V	23.11	36.19	20.74	22.82	27.97	18.84	15.08	20.15	27.18	10.28
Cr	2742	3926	2332	2565	2649	2484	1994	3216	4734	2038
Mn	868	618	884	887	531	930	1006	845	777	893
Co	107.6	85.0	106.3	102.4	81.0	115.8	116.0	105.0	97.9	122.0
Ni	2161	1728	2201	2098	1811	2243	2244	2115	1993	2494
Cu	0.9	10.2	1.1	1.1	4.2	3.4	2.6	2.9	3.5	2.4
Zn	43.1	41.4	49.5	47.4	37.1	43.6	48.8	44.1	52.7	44.8
Ga	0.48	0.88	0.45	0.49	0.47	0.34	0.31	0.42	0.53	0.22
Ge	0.81	0.75	0.83	0.79	0.77	0.82	0.84	0.75	0.79	0.87
Rb	0.190	0.481	0.150	0.241	0.061	0.035	0.036	0.042	0.041	0.021
Sr	0.17	1.52	0.11	0.19	3.68	0.54	0.49	0.68	0.77	0.28
Y	0.05	0.08	0.05	0.05	0.03	0.03	0.03	0.03	0.04	0.01
Zr	0.100	0.053	0.062	0.034	0.228	0.062	0.123	0.058	0.058	0.031
Nb	0.0046	0.0032	0.0060	0.0030	0.0034	0.0026	0.0052	0.0030	0.0058	0.0031
Cs	0.0655	0.207	0.0542	0.0894	0.0405	0.0182	0.0168	0.0212	0.0158	0.0041
Ba	0.435	0.868	0.608	0.497	1.089	0.950	0.355	0.254	0.320	0.0515
La	0.0064	0.0038	0.0037	0.0015	0.0047	0.0019	0.0061	0.0030	0.0022	0.0013
Ce	0.0113	0.0069	0.0074	0.0027	0.0094	0.0038	0.0101	0.0060	0.0037	0.0022
Pr	0.0017	0.0009	0.0010	0.0004	0.0014	0.0005	0.0016	0.0008	0.0006	0.0003
Nd	0.0073	0.0044	0.0044	0.0021	0.0054	0.0025	0.0066	0.0033	0.0026	0.0013
Sm	0.0018	0.0018	0.0016	0.0011	0.0014	0.0009	0.0021	0.0011	0.0010	0.0004
Eu	0.0006	0.0009	0.0005	0.0004	0.0006	0.0003	0.0006	0.0004	0.0004	0.0001
Gd	0.0026	0.0030	0.0020	0.0017	0.0020	0.0011	0.0023	0.0014	0.0015	0.0004
Tb	0.0006	0.0008	0.0005	0.0005	0.0004	0.0003	0.0004	0.0003	0.0004	0.0001
Dy	0.0063	0.0089	0.0056	0.0052	0.0041	0.0027	0.0038	0.0036	0.0042	0.0009
Ho	0.0018	0.0028	0.0017	0.0017	0.0012	0.0009	0.0012	0.0012	0.0014	0.0004
Er	0.0078	0.0113	0.0073	0.0077	0.0050	0.0041	0.0047	0.0048	0.0059	0.0020
Tm	0.0016	0.0025	0.0016	0.0016	0.0010	0.0010	0.0011	0.0011	0.0013	0.0006
Yb	0.0155	0.0211	0.0139	0.0150	0.0094	0.0091	0.0094	0.0096	0.0119	0.0064
Lu	0.0031	0.0041	0.0028	0.0031	0.0019	0.0020	0.0019	0.0019	0.0025	0.0015
Hf	0.0026	0.0020	0.0019	0.0012	0.0064	0.0021	0.0038	0.0018	0.0020	0.0010
Ta	0.0005	0.0003	0.0006	0.0003	0.0004	0.0003	0.0005	0.0003	0.0004	0.0003
W	0.0122	0.0450	0.0116	0.0125	0.0474	0.0239	0.0136	0.0129	0.0119	0.0122
Pb	0.0220	0.147	0.0123	0.0152	0.0157	0.0117	0.0125	0.0144	0.0138	0.0063
Th	0.0002	0.0003	0.0001	0.0000	0.0002	0.0001	0.0001	0.0001	0.0002	0.0002
U	0.0007	0.0853	0.0002	0.0001	0.0088	0.0007	0.0005	0.0012	0.0003	0.0003

Table 2: Continued

Grid Sample:	LK15-3 Ortho	LK15-3 A1 Harz	LK15-3 A2 Harz	LK15-3 A3 Harz	LK15-3 B1 Harz	LK15-3 B2 Harz	LK15-3 B3 Harz	LK15-3 C1 Harz	LK15-3 C2 Harz	LK15-3 C3 Harz
Li	2.79	0.02	0.19	0.39	0.07	0.18	0.06	4.32	0.07	0.11
B	8.7	3.6	3.3	3.2	3.6	3.5	3.2	3.0	2.9	3.1
Sc	13.3	5.83	8.03	6.93	6.17	7.02	4.92	34.5	6.22	6.77
Ti	100.4	23.99	18.88	29.67	20.55	17.22	11.28	31.34	23.19	21.32
V	57.04	29.07	35.67	29.68	37.20	30.59	22.75	31.76	38.80	36.73
Cr	4743	2547	2679	2381	2370	2613	1589	3122	2454	2499
Mn	851	809	1012	891	841	989	845	1277	822	766
Co	77.1	106.4	110.2	104.7	100.5	114.6	112.2	139.8	98.8	102.3
Ni	805	2215	2037	1956	2030	2187	2425	1910	2026	2070
Cu	3.3	4.9	4.6	5.4	6.4	6.3	19.1	6.0	5.1	5.7
Zn	37.6	52.6	51.2	49.4	48.0	54.2	53.4	61.1	47.7	48.5
Ga	1.03	0.74	0.54	0.57	0.79	0.49	0.55	0.63	0.72	0.66
Ge	0.68	0.88	0.82	0.81	0.83	0.83	0.83	0.77	0.77	0.75
Rb	0.327	0.010	0.008	0.013	0.010	0.007	0.008	0.010	0.010	0.010
Sr	11.54	0.29	0.28	0.36	0.41	0.23	0.12	0.33	0.26	0.25
Y	0.18	0.09	0.13	0.13	0.15	0.09	0.08	0.12	0.16	0.13
Zr	0.127	0.137	0.074	0.068	0.083	0.049	0.093	0.085	0.287	0.067
Nb	0.0039	0.0070	0.0047	0.0035	0.0044	0.0046	0.0046	0.0042	0.0029	0.0041
Cs	0.404	0.0090	0.0059	0.0106	0.0087	0.0064	0.0042	0.0066	0.0097	0.0095
Ba	0.0898	0.941	-	0.790	0.114	-	0.033	-	0.828	-
La	0.0057	0.0019	0.0018	0.0016	0.0025	0.0022	0.0033	0.0020	0.0014	0.0038
Ce	0.0102	0.0044	0.0038	0.0035	0.0066	0.0045	0.0070	0.0043	0.0032	0.0072
Pr	0.0016	0.0007	0.0006	0.0005	0.0008	0.0006	0.0010	0.0008	0.0006	0.0010
Nd	0.0072	0.0031	0.0029	0.0029	0.0047	0.0029	0.0040	0.0041	0.0037	0.0043
Sm	0.0031	0.0020	0.0019	0.0023	0.0022	0.0015	0.0015	0.0025	0.0023	0.0015
Eu	0.0020	0.0006	0.0006	0.0008	0.0008	0.0004	0.0005	0.0009	0.0009	0.0006
Gd	0.0063	0.0029	0.0039	0.0046	0.0045	0.0024	0.0020	0.0052	0.0051	0.0032
Tb	0.0019	0.0009	0.0013	0.0013	0.0014	0.0009	0.0006	0.0015	0.0017	0.0012
Dy	0.0207	0.0096	0.0150	0.0147	0.0169	0.0097	0.0084	0.0162	0.0188	0.0142
Ho	0.0063	0.0031	0.0047	0.0046	0.0055	0.0034	0.0029	0.0046	0.0059	0.0047
Er	0.0252	0.0131	0.0200	0.0181	0.0229	0.0139	0.0129	0.0171	0.0234	0.0185
Tm	0.0052	0.0027	0.0042	0.0036	0.0047	0.0031	0.0029	0.0033	0.0046	0.0039
Yb	0.0437	0.0251	0.0365	0.0322	0.0401	0.0274	0.0259	0.0277	0.0408	0.0340
Lu	0.0082	0.0051	0.0070	0.0061	0.0078	0.0055	0.0051	0.0052	0.0076	0.0062
Hf	0.0046	0.0045	0.0025	0.0026	0.0024	0.0015	0.0026	0.0032	0.0075	0.0023
Ta	0.0004	0.0012	0.0008	0.0006	0.0007	0.0006	0.0009	0.0004	0.0005	0.0005
W	0.0066	0.0093	0.0143	0.0137	0.0148	0.0121	0.0153	0.0137	0.0152	0.0132
Pb	0.0211	0.0046	0.0048	0.0048	0.0045	0.0046	0.0038	0.0060	0.0045	0.0049
Th	0.0008	0.0006	0.0002	0.0001	0.0001	0.0001	0.0004	0.0004	0.0002	0.0001
U	0.0014	0.0001	0.0001	0.0002	0.0005	0.0001	0.0001	0.0002	0.0001	0.0002

Table 2: Trace element abundances for selected Jormua Ophiolite Complex serpentinites (concentrations in ppm).

Grid Sample:	JU15-16 A1 Harz	JU15-16 A2 Harz	JU15-16 A3 Harz	JU15-16 B1 Harz	JU15-16 B2 Harz	JU15-16 B3 Harz	JU15-16 C1 Harz	JU15-16 C2 Harz	JU15-16 C3 Harz
Li	5.21	2.69	1.04	1.78	3.23	2.56	0.01	0.06	3.79
B	17.3	14.2	12.9	21.0	16.0	15.4	18.1	15.4	16.6
Sc	6.71	6.36	6.45	5.24	7.32	7.18	6.87	6.22	7.22
Ti	64.09	69.22	98.30	49.78	43.08	57.67	35.53	30.85	45.42
V	26.90	25.79	35.43	26.47	26.22	26.56	22.95	25.24	25.79
Cr	3187	2573	2493	3591	3485	2925	2269	2161	2455
Mn	1584	1079	678	1256	1035	884	624	718	1525
Co	137.8	112.2	112.6	131.2	131.5	117.2	104.3	120.2	121.7
Ni	2862	2609	2625	2745	2651	2474	2798	2563	2492
Cu	7.3	11.8	127.2	11.1	8.0	7.2	459.6	240.7	3.5
Zn	88.3	71.2	61.6	82.6	87.4	72.5	51.7	49.6	64.3
Ga	1.41	1.42	1.66	1.27	1.28	1.37	1.09	1.10	1.35
Ge	0.93	0.78	0.83	0.95	0.92	0.87	0.89	0.88	0.92
Rb	0.002	<0.001	0.001	<0.001	<0.001	0.000	<0.001	0.006	<0.001
Sr	0.21	0.17	0.11	0.06	0.28	0.21	0.21	0.46	0.15
Y	0.46	0.33	0.66	0.32	0.34	0.33	0.31	0.29	0.33
Zr	0.539	0.432	0.718	0.517	0.555	0.435	0.467	0.488	0.495
Nb	0.0578	0.0398	0.0536	0.0541	0.0526	0.0439	0.0482	0.0475	0.0554
Cs	0.0006	0.0006	0.0012	0.0003	0.0010	0.0005	0.0003	0.0011	0.0006
Ba	0.0919	0.0634	<0.0001	0.142	<0.0001	0.0887	0.0803	0.134	0.154
La	0.0540	0.0290	0.0323	0.0514	0.0619	0.0421	0.0373	0.0490	0.0504
Ce	0.151	0.0839	0.104	0.127	0.152	0.122	0.0850	0.138	0.124
Pr	0.0253	0.0147	0.0190	0.0191	0.0230	0.0201	0.0125	0.0221	0.0185
Nd	0.134	0.0808	0.117	0.0969	0.108	0.106	0.0604	0.101	0.0899
Sm	0.0477	0.0277	0.0536	0.0276	0.0310	0.0307	0.0223	0.0269	0.0260
Eu	0.0139	0.0072	0.0071	0.0132	0.0132	0.0084	0.0140	0.0135	0.0081
Gd	0.0558	0.0360	0.0766	0.0365	0.0372	0.0366	0.0302	0.0350	0.0331
Tb	0.0097	0.0064	0.0135	0.0060	0.0068	0.0066	0.0056	0.0062	0.0061
Dy	0.0694	0.0474	0.0981	0.0451	0.0454	0.0450	0.0441	0.0438	0.0472
Ho	0.0142	0.0100	0.0210	0.0099	0.0104	0.0099	0.0104	0.0095	0.0106
Er	0.0430	0.0304	0.0602	0.0326	0.0341	0.0307	0.0328	0.0317	0.0336
Tm	0.0067	0.0049	0.0094	0.0052	0.0055	0.0051	0.0055	0.0046	0.0055
Yb	0.0495	0.0383	0.0634	0.0399	0.0430	0.0379	0.0406	0.0334	0.0434
Lu	0.0074	0.0066	0.0100	0.0063	0.0062	0.0064	0.0061	0.0054	0.0069
Hf	0.0155	0.0133	0.0216	0.0149	0.0161	0.0133	0.0124	0.0150	0.0132
Ta	0.0039	0.0030	0.0038	0.0038	0.0045	0.0028	0.0038	0.0053	0.0030
W	0.0151	0.0110	0.0141	0.0254	0.0241	0.0235	0.0146	0.0159	0.0182
Pb	0.0505	0.0241	0.0416	0.0380	0.0319	0.0216	0.117	0.0888	0.0274
Th	<0.0001	<0.0001	<0.0001	<0.0001	<0.0001	<0.0001	<0.0001	<0.0001	<0.0001
U	0.0024	0.0010	0.0012	0.0024	0.0168	0.0018	0.0015	0.0035	0.0031

(continued)

Table 2: Continued

Grid Sample:	JU15-18 A1 Harz	JU15-18 A2 Harz	JU15-18 A3 Harz	JU15-18 B1 Harz	JU15-18 B2 Harz	JU15-18 B3 Harz	JU15-18 C1 Harz	JU15-18 C2 Harz	JU15-18 C3 Harz
Li	0.31	1.03	0.89	0.83	1.01	0.90	0.74	0.86	0.88
B	6.0	6.6	6.3	7.3	7.4	6.0	6.9	6.3	5.4
Sc	7.49	9.72	8.73	10.16	17.85	9.54	13.79	10.89	9.57
Ti	211.1	238.4	284.1	181.5	12450	271.5	440.9	270.2	264.2
V	63.94	74.27	82.25	58.57	59.55	75.85	66.38	61.48	75.98
Cr	1656	3390	2588	1445	911	2327	2536	1647	2633
Mn	771	796	835	773	1541	837	781	790	841
Co	123.3	119.6	120.1	121.1	86.1	122.4	124.3	122.5	128.0
Ni	2424	2296	2314	2329	1246	2245	2351	2304	2481
Cu	19.7	18.1	18.1	18.8	4.3	17.5	19.0	19.5	19.3
Zn	36.1	56.6	47.1	32.4	40.5	47.9	48.4	36.5	54.9
Ga	3.23	3.87	3.84	3.38	3.50	3.67	3.60	3.43	3.74
Ge	1.06	1.07	1.07	1.07	1.05	1.03	1.08	1.07	1.05
Rb	0.360	0.439	0.481	0.563	0.505	0.595	0.325	0.615	0.595
Sr	0.47	0.25	0.18	0.51	1.18	0.78	0.41	0.71	0.63
Y	2.38	2.09	3.14	2.53	3.08	2.79	2.62	2.47	2.68
Zr	1.680	1.670	2.077	1.787	31.60	3.038	1.982	2.000	1.788
Nb	0.497	0.459	0.466	0.546	7.879	0.458	0.784	0.568	0.419
Cs	0.0731	0.0663	0.0848	0.0832	0.0895	0.0863	0.0747	0.0811	0.0837
Ba	0.983	1.283	0.529	1.601	2.948	23.11	1.205	6.502	10.47
La	1.038	0.908	1.072	1.111	2.372	0.961	1.033	0.973	0.891
Ce	2.368	2.005	2.343	2.407	3.861	2.128	2.204	2.038	1.939
Pr	0.319	0.269	0.318	0.325	0.479	0.287	0.293	0.277	0.262
Nd	1.316	1.114	1.359	1.314	1.947	1.221	1.214	1.158	1.130
Sm	0.313	0.269	0.359	0.319	0.441	0.317	0.302	0.289	0.306
Eu	0.126	0.112	0.128	0.137	0.188	0.128	0.141	0.132	0.120
Gd	0.337	0.285	0.407	0.338	0.479	0.362	0.346	0.321	0.343
Tb	0.0559	0.0486	0.0691	0.0584	0.0751	0.0620	0.0607	0.0563	0.0593
Dy	0.370	0.324	0.475	0.392	0.497	0.423	0.405	0.396	0.405
Ho	0.0744	0.0663	0.100	0.0793	0.101	0.0876	0.0865	0.0803	0.0824
Er	0.211	0.185	0.2865	0.229	0.307	0.250	0.249	0.238	0.242
Tm	0.0295	0.0259	0.0416	0.0333	0.0456	0.0370	0.0378	0.0358	0.0356
Yb	0.184	0.170	0.276	0.217	0.304	0.238	0.247	0.240	0.228
Lu	0.0247	0.0238	0.0369	0.0305	0.0510	0.0332	0.0362	0.0359	0.0315
Hf	0.0493	0.0646	0.0740	0.0569	0.817	0.0904	0.0790	0.0800	0.0680
Ta	0.0397	0.0342	0.0321	0.0392	0.450	0.0308	0.0525	0.0367	0.0305
W	0.0548	0.0479	0.118	0.0484	0.175	0.0462	0.0474	0.0499	0.0425
Pb	0.362	0.336	0.382	0.372	0.156	0.371	0.350	0.323	0.420
Th	0.0082	0.0233	0.0218	0.0074	0.1010	0.0289	0.0391	0.0240	0.0195
U	0.0097	0.0087	0.0110	0.0093	0.0526	0.0096	0.0095	0.0086	0.0076

Table 3: Major element abundances for Leka Ophiolite Complex olivines (reported in wt%). Reported uncertainties (2σ) refer to the standard deviation of the averaged values for each sample. The number of spots analyzed for each sample ranged from 8 to 10.

Sample	FeO	2σ	CaO	2σ	TiO_2	2σ	MgO	2σ	MnO	2σ	Cr_2O_3	2σ	Al_2O_3	2σ	NiO	2σ	SiO_2	2σ	Total	Mg#
LK15-4																				
A1 Harz	8.50	0.22	0.01	0.02	0.00	0.01	49.79	0.30	0.12	0.04	0.01	0.02	0.00	0.01	0.39	0.06	40.93	0.29	99.8	91.3
A2 Harz	8.49	0.38	0.01	0.02	0.00	0.01	49.76	0.37	0.13	0.04	0.00	0.01	0.01	0.01	0.40	0.04	40.76	0.44	99.6	91.3
A3 Dunite	8.21	0.43	0.01	0.01	0.01	0.02	50.11	0.41	0.12	0.03	0.00	0.02	0.00	0.01	0.40	0.06	41.01	0.41	99.9	91.6
A3 Harz	8.67	0.20	0.01	0.02	0.00	0.02	50.16	0.56	0.12	0.03	0.00	0.02	0.00	0.01	0.42	0.05	41.05	0.35	100.4	91.2
B1 Dunite	8.44	0.30	0.01	0.01	0.00	0.01	50.09	0.60	0.12	0.03	0.00	0.02	0.01	0.01	0.38	0.04	40.92	0.45	100.0	91.4
B1 Harz	8.30	0.25	0.01	0.02	0.00	0.01	49.85	0.51	0.12	0.03	0.00	0.01	0.00	0.01	0.38	0.04	40.92	0.33	99.6	91.5
B2 Harz	8.42	0.27	0.02	0.02	0.00	0.00	49.57	0.61	0.11	0.06	0.01	0.03	0.00	0.01	0.40	0.03	40.76	0.39	99.3	91.3
B3 Harz	8.87	0.52	0.01	0.02	0.00	0.01	49.81	0.62	0.13	0.06	0.01	0.04	0.01	0.01	0.42	0.04	40.85	0.53	100.1	90.9
C1 Harz	8.56	0.40	0.01	0.03	0.00	0.00	50.08	0.46	0.11	0.03	0.01	0.02	0.01	0.01	0.41	0.05	41.09	0.26	100.3	91.2
C2 Harz	8.43	0.32	0.01	0.01	0.00	0.01	50.04	0.40	0.11	0.04	0.01	0.02	0.01	0.01	0.40	0.06	40.85	0.21	99.8	91.4
C3Dun/Harz	8.84	0.66	0.01	0.02	0.00	0.01	49.61	0.90	0.12	0.06	0.01	0.02	0.01	0.02	0.39	0.04	40.79	0.37	99.8	90.9
C3 Harz	8.76	0.62	0.01	0.01	0.01	0.02	49.86	0.33	0.12	0.04	0.02	0.03	0.01	0.01	0.41	0.05	40.84	0.19	100.0	91.0
LK15-10																				
A1 Harz	8.08	0.82	0.01	0.02	0.00	0.02	51.08	0.42	0.22	0.09	0.01	0.01	0.00	0.01	0.42	0.05	39.98	0.58	99.8	91.8
A2 Harz	8.30	0.81	0.02	0.03	0.00	0.02	50.44	0.64	0.21	0.07	0.01	0.03	0.00	0.01	0.37	0.05	40.70	0.58	100.1	91.5
A3 Harz	7.44	0.85	0.02	0.02	0.00	0.01	51.21	0.83	0.24	0.15	0.02	0.03	0.01	0.01	0.35	0.14	40.96	0.41	100.2	92.5
B1 Harz	8.08	0.49	0.02	0.05	0.00	0.00	50.63	0.78	0.18	0.08	0.01	0.02	0.01	0.01	0.40	0.04	40.64	0.44	100.0	91.8
B2 Harz	7.09	0.62	0.01	0.03	0.01	0.02	51.34	0.37	0.25	0.07	0.01	0.03	0.01	0.02	0.37	0.01	40.90	0.40	100.0	92.8
B3 Harz	8.13	0.29	0.02	0.02	0.00	0.01	50.82	0.39	0.38	0.22	0.00	0.01	0.01	0.02	0.33	0.23	40.53	0.32	100.2	91.8
C1 Harz	7.51	0.61	0.01	0.02	0.00	0.00	50.47	0.54	0.26	0.05	0.01	0.03	0.01	0.02	0.37	0.03	40.53	0.53	99.2	92.3

Table 4: Osmium isotope systematics and highly siderophile element abundance* data for Leka Ophiolite peridotites.

Grid Sample:	LK15-4 A1 Harz	LK15-4 A2 Harz	LK15-4 A3 Dunite	LK15-4 A3 Harz	LK15-4 A3 Harz (Replicate)	LK15-4 B1 Dunite	LK15-4 B1 Harz	LK15-4 B2 Harz	LK15-4 B3 Harz	LK15-4 C1 Harz	LK15-4 C2 Harz
Os	4.274	5.119	3.906	5.869	3.302	1.799	2.672	4.194	5.142	4.528	2.804
Ir	2.155	2.638	3.388	4.145	3.456	1.493	2.019	1.835	2.988	3.180	1.879
Ru	3.780	3.580	4.129	7.416	3.312	2.315	2.173	2.165	3.870	3.000	2.151
Pt	4.032	7.380	6.197	7.678	7.224	1.715	8.212	7.477	8.536	11.39	4.322
Pd	4.128	2.331	3.629	8.026	8.631	0.892	6.935	1.317	6.667	6.267	3.470
Re	0.021	0.030	0.024	0.012	0.011	0.060	0.028	0.022	0.020	0.031	0.037
$^{187}Re/^{188}Os$	0.0238	0.0283	0.030	0.0096	0.017	0.160	0.0501	0.0258	0.0185	0.033	0.0627
$\pm 2\sigma$ (abs)	0.0003	0.0003	0.0019	0.0002	0.0022	0.0041	0.0005	0.0003	0.0003	0.0016	0.0005
$^{187}Os/^{188}Os$	0.12652	0.12548	0.12579	0.12118	0.12147	0.12691	0.12570	0.12587	0.12572	0.12624	0.12628
$^{187}Os/^{188}Os_i$	0.1263	0.1252	0.1256	0.1211	0.1213	0.1256	0.1253	0.1257	0.1256	0.1260	0.1258
$\gamma Os_{(497\ Ma)}$	2.2	1.3	1.5	-2.1	-1.9	1.5	1.3	1.6	1.5	1.9	1.7
$\pm 2\sigma$	0.2	0.2	0.2	0.2	0.2	0.2	0.2	0.2	0.2	0.2	0.2
T_{RD}	0.3	0.4	0.4	1.0	1.0	0.4	0.4	0.4	0.4	0.3	0.4

Grid Sample:	LK15-4 C3 Dun/Harz	LK15-4 C3 Harz	LK15-4 A3(1) Harz	LK15-4 A3(2) Ortho	LK15-4 A3(3) Harz	LK15-4 A3(4) Harz
Os	2.523	3.201	3.352	2.792	4.965	5.103
Ir	2.402	4.076	3.006	2.255	2.586	1.921
Ru	1.877	3.303	4.271	0.924	5.582	2.824
Pt	8.769	8.362	8.511	94.20	7.423	6.452
Pd	2.517	2.601	7.003	80.83	6.163	7.114
Re	0.004	0.003	0.025	0.028	0.006	0.007
$^{187}Re/^{188}Os$	0.0085	0.0051	0.0358	0.0476	0.0062	0.0061
$\pm 2\sigma$ (abs)	0.0028	0.0023	0.0003	0.0005	0.0005	0.0005
$^{187}Os/^{188}Os$	0.12553	0.12528	0.12198	0.12465	0.12235	0.12221
$^{187}Os/^{188}Os_i$	0.1255	0.1252	0.1217	0.1243	0.1223	0.1222
$\gamma Os_{(497\ Ma)}$	1.5	1.3	-1.6	0.5	-1.1	-1.2
$\pm 2\sigma$	0.2	0.2	0.2	0.2	0.2	0.2
T_{RD}	0.4	0.4	0.9	0.6	0.9	0.9

*HSE are reported in ppb.

Locality abbreviations are the same as in Table 1.

Uncertainty on $^{187}Os/^{188}Os$ is ~±0.2% (see text for details)

Chondrite data for T_{RD} model age calculations obtained from Walker et al., 2002.

Table 4: Osmium isotope systematics and highly siderophile element abundance* data for Leka Ophiolite peridotites.

Grid Sample:	LK15-3 (Bulk) Ortho	LK15-9 A(1) Ortho	LK15-9 A(2) Harz	LK15-9 A(3) Harz	LK15-9 A(4) Harz	LK15-9 A(4) Harz (Replicate)	LK15-9 A(5) Harz	LK15-9 C Dunite	LK15-10 A1 Harz	LK15-10 A2 Harz	LK15-10 A3 Harz
Os	1.270	5.912	3.521	3.063	3.792	3.883	5.698	0.144	3.320	4.738	7.024
Ir	1.613	2.397	3.486	2.269	4.019	3.088	6.646	0.218	3.349	2.937	3.037
Ru	2.930	3.314	1.435	1.370	1.372	2.024	2.042	1.182	5.336	7.247	15.331
Pt	187.4	5.741	7.338	5.309	25.50	18.46	71.78	0.096	10.34	5.741	7.906
Pd	47.08	58.50	3.527	2.816	11.90	11.34	28.51	0.075	3.574	2.984	12.62
Re	0.0587	0.093	0.0192	0.017	0.0292	0.0375	0.0514	0.0335	0.044	0.055	0.059
$^{187}Re/^{188}Os$	0.223	0.0756	0.0263	0.0259	0.0371	0.0466	0.0434	1.125	0.064	0.056	0.040
$\pm 2\sigma$ (abs)	0.0016	0.0005	0.0003	0.0008	0.0003	0.0007	0.0007	0.0070	0.0022	0.0015	0.0010
$^{187}Os/^{188}Os$	0.12955	0.13697	0.12592	0.12546	0.12653	0.12635	0.12556	0.16499	0.12446	0.12276	0.12400
$^{187}Os/^{188}Os_i$	0.1277	0.1363	0.1257	0.1252	0.1262	0.1260	0.1252	0.1556	0.1239	0.1223	0.1237
$\gamma Os_{(497\ Ma)}$	3.3	10.3	1.6	1.3	2.1	1.9	1.2	25.9	0.2	-1.1	0.0
$\pm 2\sigma$	0.2	0.2	0.2	0.2	0.2	0.2	0.2	0.2	0.2	0.2	0.2
T_{RD}	0.1	-1.1	0.6	0.4	0.3	0.3	0.4	-4.0	0.6	0.9	0.6

Grid Sample:	LK15-10 A3 Web	LK15-10 A3 Web (Replicate)	LK15-10 B1 Harz	LK15-10 B2 Harz	LK15-10 B3 Harz	LK15-10 B3 Harz (Replicate)	LK15-10 C1 Harz	LK15-10 C2 Harz	LK15-10 C3 Harz
Os	0.087	0.071	2.746	4.840	6.551	3.760	3.209	2.054	5.131
Ir	0.163	0.176	2.387	3.442	4.463	4.002	2.550	2.572	2.246
Ru	0.062	0.040	5.705	5.521	10.41	5.016	4.466	3.338	8.921
Pt	54.84	41.85	4.953	6.164	24.56	10.92	5.648	15.83	5.814
Pd	-	67.28	10.84	1.578	2.542	1.043	2.914	21.31	4.901
Re	0.043	0.046	0.029	0.066	0.034	0.031	0.034	0.066	0.055
$^{187}Re/^{188}Os$	2.37	3.13	0.051	0.065	0.025	0.0392	0.050	0.156	0.052
$\pm 2\sigma$ (abs)	0.082	0.014	0.0027	0.0015	0.0011	0.0003	0.0022	0.0086	0.0034
$^{187}Os/^{188}Os$	0.15302	0.15687	0.12285	0.12475	0.12368	0.12374	0.12223	0.12387	0.12370
$^{187}Os/^{188}Os_i$	0.1333	0.1309	0.1224	0.1242	0.1235	0.1234	0.1218	0.1226	0.1233
$\gamma Os_{(1.95Ga)}$	7.8	5.8	-1.0	0.4	-0.2	-0.2	-1.5	-0.9	-0.3
$\pm 2\sigma$	0.2	0.2	0.2	0.2	0.2	0.2	0.2	0.2	0.2
T_{RD}	-0.8	-0.4	0.8	0.6	0.7	0.7	0.9	0.8	0.7

*HSE are reported in ppb.

Locality abbreviations are the same as in Table 1.

Uncertainty on $^{187}Os/^{188}Os$ is ~±0.2% (see text for details)

Chondrite data for T_{RD} model age calculations obtained from Walker et al., 2002.

Table 4: Osmium isotope systematics and highly siderophile element abundance* data for Leka/Jormua Ophiolite peridotites.

Grid Sample:	JU15-16 A1 Harz	JU15-16 A2 Harz	JU15-16 A2 Harz (Replicate)	JU15-16 A3 Harz	JU15-16 B1 Harz	JU15-16 B2 Harz	JU15-16 B3 Harz	JU15-16 C1 Harz	JU15-16 C2 Harz	JU15-16 C3 Harz
Os	1.838	3.358	4.943	1.860	1.787	2.076	2.534	9.004	5.270	1.590
Ir	7.222	5.984	6.111	3.778	4.072	4.117	3.079	4.063	1.193	7.472
Ru	9.525	40.34	38.93	4.371	10.14	10.29	7.724	5.464	5.637	5.537
Pt	6.543	6.200	6.479	13.86	9.673	9.723	7.427	3.357	2.950	2.749
Pd	6.799	6.642	6.574	6.620	3.512	3.561	1.094	0.446	1.123	0.242
Re	0.007	0.009	0.017	0.005	0.019	0.019	0.016	0.031	0.027	0.017
$^{187}Re/^{188}Os$	0.018	0.012	0.0168	0.012	0.050	0.045	0.0309	0.0163	0.0243	0.0521
$\pm 2\sigma$ (abs)	0.0050	0.0030	0.0002	0.0038	0.0077	0.0067	0.0004	0.0001	0.0002	0.0006
$^{187}Os/^{188}Os$	0.11193	0.11165	0.11120	0.11319	0.11201	0.11199	0.11189	0.11195	0.11379	0.11322
$^{187}Os/^{188}Os_i$	0.1113	0.1112	0.1106	0.1128	0.1104	0.1105	0.1109	0.1114	0.1130	0.1115
$\gamma Os_{(497\ Ma)}$	-2.1	-2.2	-2.7	-0.8	-3.0	-2.8	-2.5	-2.0	-0.7	-2.0
$\pm 2\sigma$	0.2	0.2	0.2	0.2	0.2	0.2	0.2	0.2	0.2	0.2
T_{RD}	2.4	2.4	2.5	2.2	2.5	2.5	2.4	2.4	2.1	2.4

Grid Sample:	JU15-18 A1 Harz	JU15-18 A2 Harz	JU15-18 A3 Harz	JU15-18 B1 Harz	JU15-18 B2 Harz	JU15-18 B3 Harz	JU15-18 C1 Harz	JU15-18 C2 Harz	JU15-18 C3 Harz
Os	1.677	1.555	1.373	2.087	3.912	1.762	3.337	4.241	1.928
Ir	2.051	2.651	2.057	2.494	4.344	2.011	3.202	2.769	2.893
Ru	5.957	5.146	5.312	7.492	9.534	4.760	6.165	2.927	5.881
Pt	3.135	3.155	5.168	2.606	7.852	2.779	5.521	0.688	7.214
Pd	1.928	0.952	3.007	2.639	5.673	3.680	1.142	0.738	2.734
Re	0.220	0.190	0.210	0.212	0.062	0.180	0.247	0.238	0.310
$^{187}Re/^{188}Os$	0.6316	0.589	0.7386	0.4891	0.0762	0.4931	0.3561	0.2702	0.776
$\pm 2\sigma$ (abs)	0.0006	0.0017	0.0007	0.0005	0.0003	0.0006	0.0003	0.0002	0.0014
$^{187}Os/^{188}Os$	0.13201	0.13494	0.13797	0.12872	0.12564	0.13517	0.12527	0.11892	0.13639
$^{187}Os/^{188}Os_i$	0.1112	0.1155	0.1136	0.1126	0.1231	0.1189	0.1135	0.1100	0.1108
$\gamma Os_{(1.95Ga)}$	-2.3	1.5	-0.1	-1.0	8.3	4.5	-0.2	-3.3	-2.6
$\pm 2\sigma$	0.2	0.2	0.2	0.2	0.2	0.2	0.2	0.2	0.2
T_{RD}	2.4	1.8	2.1	2.2	0.7	1.3	2.1	2.6	2.5

*HSE are reported in ppb.

Locality abbreviations are the same as in Table 1.

Uncertainty on $^{187}Os/^{188}Os$ is ~±0.2% (see text for details)

Chondrite data for T_{RD} model age calculations obtained from Walker et al., 2002.

Table 4: Osmium isotope systematics and highly siderophile element abundance* data for Leka/Jormua Ophiolite peridotites.

Grid	ATK	ATK	ATK	ATK	ATK	ATK	ATK	ATK	LHV
Sample:	57-A	57-B	59	75	76	96	589	600	21
Os	3.254	4.037	2.665	4.820	6.159	3.457	10.84	3.623	2.206
Ir	4.456	3.544	2.386	3.877	4.422	3.020	5.605	1.815	0.364
Ru	5.689	7.517	5.065	9.206	1.656	7.451	9.336	4.052	2.646
Pt	7.718	4.738	3.877	4.456	4.976	6.037	6.715	3.587	3.013
Pd	3.844	3.015	2.341	1.842	1.120	3.105	2.575	2.071	0.916
Re	0.034	0.037	0.112	0.033	0.052	0.284	0.030	0.046	0.084
$^{187}Re/^{188}Os$	0.0504	0.0436	0.203	0.0329	0.0404	0.395	0.0135	0.0605	0.184
$\pm2\sigma$ (abs)	0.0005	0.0004	0.0020	0.0003	0.0004	0.0040	0.0001	0.0006	0.0018
$^{187}Os/^{188}Os$	0.1159	0.1157	0.1174	0.1115	0.1113	0.1146	0.1111	0.1176	0.1174
$^{187}Os/^{188}Os_i$	0.1142	0.1143	0.1107	0.1104	0.1100	0.1016	0.1107	0.1156	0.1113
$\gamma Os_{(497\ Ma)}$	0.45	0.46	-2.7	-2.9	-3.3	-10.7	-2.7	1.6	-2.1
$\pm2\sigma$	0.2	0.2	0.2	0.2	0.2	0.2	0.2	0.2	0.2
T_{RD}	1.7	1.8	1.5	2.3	2.4	1.9	2.4	1.5	1.5

*HSE are reported in ppb.
Locality abbreviations are the same as in Table 1.
Uncertainty on $^{187}Os/^{188}Os$ is ~±0.2% (see text for details)
Chondrite data for T_{RD} model age calculations obtained from Walker et al., 2002.

Table 5: Total Analytical Blank (TAB) Data.

TAB	Ir (pg)	Ru (pg)	Pt (pg)	Pd (pg)	Re (pg)	Os (pg)	$^{187}Os/^{188}Os$
11/1/2015	0.10	20.1	432	5.9	0.8	1.20	0.1522
2/17/2016	0.01	9.6	152	3.4	4.5	0.68	0.3701
4/8/2016	0.17	8.0	191	1.9	4.5	0.64	0.6651
7/11/2016	0.28	20.8	146	11.4	13	0.37	0.1936
8/5/2016	0.23	10.4	254	6.6	0.6	2.94	0.4651
11/10/2016		16.7	256	0.8		1.56	0.1204
11/10/2016		6.8	145	0.3			
5/28/2017*	0.29	69.4	97.0	4.1	1.7	3.08	0.1247

*Ir, Ru, Pt, Pd, and Re run on *ThermoFisher Element2* sector field ICP-MS

Table 6: Os standard analyses for N-TIMS using a secondary electron multiplier (SEM) detector of a *ThermoFisher Triton*® mass spectrometer. 2SDM% represents the percent of standard deviation of the mean at the 2σ level

	$^{187}Os/^{188}Os$	2SDM	$^{186}Os/^{188}Os$	2SDM	$^{190}Os/^{188}Os$	2SDM	$^{189}Os/^{188}Os$	2SDM
12/16/2015	0.11376	0.058	0.12002	0.089	1.9838	0.040	1.2196	0.043
12/19/2015	0.11382	0.041	0.11991	0.061	1.9840	0.021	1.2197	0.021
12/19/2015	0.11378	0.040	0.11989	0.058	1.9837	0.017	1.2195	0.021
3/7/2016	0.11368	0.071	0.11985	0.069	1.9840	0.033	1.2197	0.040
3/8/2016	0.11381	0.073	0.11984	0.091	1.9848	0.035	1.2201	0.036
4/25/2016	0.11366	0.034	0.11976	0.040	1.9853	0.012	1.2200	0.016
4/27/2016	0.11356	0.068	0.11963	0.094	1.9836	0.032	1.2197	0.034
7/27/2016	0.11350	0.067	0.11950	0.085	1.9856	0.027	1.2198	0.028
7/28/2016	0.11357	0.083	0.11974	0.101	1.9846	0.021	1.2200	0.029
9/19/2016	0.11375	0.055	0.11978	0.068	1.9849	0.021	1.2226	0.028
9/21/2016	0.11380	0.052	0.11988	0.067	1.9847	0.023	1.2222	0.031
11/20/2016	0.11381	0.067	0.11994	0.089	1.9834	0.032	1.2191	0.036
11/21/2016	0.11393	0.082	0.12004	0.112	1.9846	0.051	1.2200	0.047
11/23/2016	0.11387	0.090	0.12029	0.158	1.9851	0.042	1.2208	0.047
11/23/2016	0.11371	0.072	0.11987	0.102	1.9837	0.035	1.2199	0.041
6/1/2017	0.11359	0.062	0.11960	0.073	1.9855	0.027	1.2203	0.037
6/3/2017	0.11363	0.079	0.11978	0.094	1.9849	0.034	1.2203	0.034

References

1. Abbey S. (1983) Studies in "standard samples" of silicate rocks and minerals 1969- 1982. *Pap Geol Surv Canada* 83-15: 1-114.

2. Alard, O., Griffin, W. L., Lorand, J. P., Jackson, S. E., O'Reilly, S. Y. O. (2000) Non-chondritic distribution of the highly siderophile elements in mantle sulphides. *Nature. Vol. 407* 891- 894.

3. Alard, O., Luguet, A., Pearson, N. J., Griffin, W. L., Lorand, J.-P., Gannoun, A., Burton, K. W. & O'Reilly, S. Y. (2005). *In situ* Os isotopes in abyssal peridotites bridge the isotopic gap between MORBs and their source mantle. *Nature* 436, 1005-1008.

4. Allégre, C.J., Luck, J.M., 1980. Osmium isotopes as petrogenetic and geological tracers. *Earth Planet. Sci. Lett.* 48, 148–154.

5. Allégre, C. J. & Turcotte, D. L. (1986). Implications of a two-component marble-cake mantle. *Nature* 323, 123-127.

6. Azimow P. D. (1999) A model that reconciles major- and trace element data from abyssal peridotites. *Earth Planet. Sci. Lett.* 169, 303–319.

7. Becker, H., Shirey, S. B. & Carlson, R. W. (2001). Effects of melt percolation on the Re–Os systematics of peridotites from a Paleozoic convergent plate margin. *Earth and Planetary Science Letters* 188, 107–121.

8. Becker, H., Horan, M. F., Walker, R. J., Gao S., Lorand J.-P. and Rudnick R. L. (2006). Highly siderophile element composition of the Earth's primitive upper mantle: constraints from new data on peridotite massifs and xenoliths. *Geochim. Cosmochim. Acta* 70(17), 4528–4550.

9. Birck, J. L., Roy-Barman, M. & Capmas, F. (1997). Re–Os isotopic measurements at the femtomole level in natural samples. *Geostandards Newsletter* 21, 19–27.

10. Bizimis, M., Griselin, M., Lassiter, J. C., Salters, V. J. M. & Sen, G. (2007). Ancient recycled mantle lithosphere in the Hawaiian plume: Osmium–Hafnium isotopic evidence from peridotite mantle xenoliths. *Earth and Planetary Science Letters* 257, 259–273.

11. Borghini, G., Rampone, E., Zanetti, A., Cipriani, A., Class, C., Hofmann, A.W., Goldstein, S., (2011). Small Scale Heterogeneities in MORB Mantle: Insights on Pyroxenite–Peridotite Association from External Liguride Ophiolites (Italy). Goldschmidt Conference 2011, Prague: Mineralogical Magazine, vol. 75 (3).

12. Borghini, G., Rampone, E., Zanetti, A., Cipriani, A., Class, C., Hofmann, A.W., Goldstein, S., (2016). Pyroxenite Layers in the Northern Apennines' Upper Mantle (Italy)—Generation by Pyroxenite Melting and Melt Infiltration. *Journal of Petrology*, Vol. 57, No. 4, 625-653.

13. Boyd F. R. and Mertzman S. A. (1987) Composition of structure of the Kaapvaal lithosphere, southern Africa. *Geochem. Soc. Spec.* Pub. 1, 13–24.

14. Brandon, A. D., Snow, J. E., Walker, R. J., Morgan, J. W. & Mock, T. D. (2000). 190Pt–186Os and 187Re–187Os systematics of abyssal peridotites. *Earth and Planetary Science Letters* 177, 319–335.

15. Büchl, A., Brügmann, G. E., Batanova, V. G., Münker, C. & Hofmann, A. W. (2002). Melt-percolation monitored by Os isotopes and HSE abundances: a case study from the mantle section of the Troodos Ophiolite. *Earth and Planetary Science Letters* 204, 385–402.

16. Büchl, A., Brügmann, G. E. & Batanova, V. G. (2004a). Formation of podiform chromitite deposits: implications from PGE abundances and Os isotopic compositions of chromites from the Troodos complex, Cyprus. Chemical Geology 208, 217–232.

17. Büchl, A., Brügmann, G. E., Batanova, V. G. & Hofmann, A. W. (2004b). Os mobilization during melt percolation: The evolution of Os isotope heterogeneities in the mantle sequence of the Troodos ophiolite, Cyprus. Geochimica et Cosmochimica Acta 68, 3397–3408.

18. Burton, K. W., Bourdon, B., Birck, J. L., Allégre, C. J., Hein, J. R. (1999). Osmium isotope variations in the oceans recorded by Fe-Mn crusts. *Earth and Planetary Science Letters* 171, 185-197.

19. Burton, K. W., Cenki-Tok, B., Mokadem, F., Harvey, J., Gannoun, A., Alard, O. & Parkinson, I. J. (2012). Unradiogenic lead in Earth's upper mantle. Nature Geoscience 5(8), 570–573.

20. Carlson, R.W., Moore, R.O., (2004). Age of the eastern Kaapvaal mantle: ReOs isotope data for peridotite xenoliths from the Monastery kimberlite. S. Afr. *J. Geol*. 107, 81–90.

21. Chew, D. M. & Strachan, R. A. (2014). The Laurentian Caledonides of Scotland and Ireland. In: Corfu, F., Gasser, D. & Chew, D. M. (eds) *New Perspectives on the Caledonides of Scandinavia and Related Areas. Geological Society, London, Special Publications* 309, 45–91.

22. Carlson, R. W. (2005). Application of the Pt–Re–Os isotopic systems to mantle geochemistry and geochronology. *Lithos* 82, 249–272.

23. Cohen, A. S. & Waters, G. G. (1996). Separation of osmium from geological materials by solvent extraction for analysis by thermal ionization mass spectrometry. *Analytica Chimica Acta* 332, 269–275.

24. Dahl, R. M., Carstens, H. & Haukdal, G. (2011). The election of a national Norwegian geological monument. A tool for raising awareness of geological heritage. *GeoJournal of Tourism and Geosites* 2(8), 178–184.

25. Day, J. M. D. (2013). Hotspot volcanism and highly siderophile elements. *Chemical Geology* 341, 50–74.

26. Day, J. M. D., Peters, B. J. & Janney, P. E. (2014). Oxygen isotope systematics of South African olivine melilitites and implications for HIMU mantle reservoirs. *Lithos* 202–203, 76–84.

27. DePaolo, D. J. & Wasserburg G. J. (1976). Nd Isotopic Variations and petrogenetic models. *Geophysical Research Letters* Vol. 3, No. 5, 249-252.

28. Dick, H. J. B., Fisher, R. L. & Bryan, W. B. (1984). Mineralogic variability of the uppermost mantle along mid-ocean ridges. *Earth and Planetary Science Letters* 69, 88–106.

29. Dilek, Y. & Furnes, H. (2011). Ophiolite genesis and global tectonics: Geochemical and tectonic fingerprinting of ancient oceanic lithosphere. *Geological Society of America Bulletin* 123, 387–411.

30. Droop, G. T. R. (1987). A general equation for estimating Fe^{3+} concentrations in ferromagnesian silicates and oxides from microprobe analyses, using stoichiometric criteria. *Mineralogical Magazine* 51, 431-435.

31. Dunning, G. R. & Pedersen, R. B. (1988). U/Pb ages of ophiolites mand arc-related plutons of the Norwegian Caledonides-implications for the development of Iapetus. *Contributions to Mineralogy and Petrology* 98, 13-23.

32. Evans, B.W., Trommsdorff, V. (1974). On elongate olivine of meta-morphic origin. *Geology 2*: 131-132.

33. Furnes, H., Pedersen, R. B. & Stillman, C. J. (1988). The Leka Ophiolite Complex, central Norwegian Caledonides—field characteristics and geotectonic significance. *Journal of The Geological Society, London* 145, 401–412.

34. Furnes, H., Pedersen, R. B., Hertogen, J. & Albrektsen, B. A. (1992). Magma development of the Leka Ophiolite Complex, Central Norwegian Caledonides. *Lithos* 27, 259–277.

35. Gannoun, A., Burton, K.W., Parkinson, I.J., Alard, O., Schiano, P., Thomas, L.E., (2007). The scale and origin of the osmium isotope variations in mid-ocean ridge basalts. Earth and Planetary Science Letters 259, 541–556.

36. Govindaraju, K. (1994). Compilation of working values and sample description for 383 geostandards. Geostandards Newsletter, *The Journal of Geostandards and Geoanalysis* 18: 158.

37. Hamdy, M. M., Harrz, H. Z., Aly, G. A. (2011). Pan-African (intraplate and subduction-related?) metasomatism in the Fawakhir ophiolitic serpentinites, Central Eastern Desert of Egypt: mineralogical and geochemical evidences. *Arabian Journal of Geosciences.* 6(1) 1-21.

38. Hanghøjet, K., Kelemen, P. B., Hassler, D. & Godard, M. (2010). Composition and genesis of depleted mantle peridotites from the Wadi Tayin Massif, Oman ophiolite; major and trace element geochemistry, and Os isotope and PGE systematics. *Journal of Petrology* 51, 201–227.

39. Hart, S. R., Blusztajn, J., Dick, H. J. B., Meyer, P. S. & Muehlenbachs, K. (1999). The fingerprint of seawater circulation in a 500-meter section of ocean crust gabbros. *Geochimica et Cosmochimica Acta* 63, 4059–4080.

40. Harvey, J., Gannoun, A., Burton, K. W., Rogers, N. W., Alard, O. & Parkinson, I. J. (2006). Ancient melt extraction from the oceanic upper mantle revealed by Re–Os isotopes in abyssal peridotites from the Mid-Atlantic ridge. *Earth and Planetary Science Letters* 244, 606–621.

41. Ishikawa, A., Pearson, D. G. & Dale, C. W. (2011). Ancient Os isotope signatures from the Ontong Java Plateau lithosphere: Tracing lithospheric accretion history. *Earth and Planetary Science Letters* 301, 159–170.

42. Iyer, K., Austrheim, H., John, T., Jamtveit, B., Serpentinization of the oceanic lithosphere and some geochemical consequences: Constraints from the Leka Ophiolite Complex, Norway (2007). *Chemical Geology* 249, 66-90.

43. Kelemen, P. B. (1990). Reaction between ultramafic wall rock and fractionating basaltic magma: Part I, Phase relations, the origin of calc-alkaline magma series, and the formation of discordant dunite. *Journal of Petrology* 31, 51–98.

44. Kelemen, P. B. & Dick, H. J. B. (1995). Focused melt flow and localized deformation in the upper mantle: juxtaposition of replacive dunite and ductile shear zones in the Josephine peridotite, SW Oregon. *Journal of Geophysical Research* 100, 423–438.

45. Kelemen, P. B., Dick, H. J. B. & Quick, J. E. (1992). Formation of harzburgite by pervasive melt–rock reaction in the upper mantle. *Nature* 358, 635–641.

46. Kelemen, P. B., Shimizu, N. & Salters, V. J. M. (1995a). Extraction of mid-ocean-ridge basalt from the upwelling mantle by focused flow of melt in dunite channels. *Nature* 375, 747–753.

47. Kelemen, P. B., Whitehead, J. A., Aharonov, E. & Jordahl, K. A. (1995b). Experiments on flow focusing in soluble porousmedia, with applications to melt extraction from the mantle. *Journal of Geophysical Research* 100, 475–496.

48. Kelemen, P. B., Hirth, G., Shimizu, N., Spiegelman, M. & Dick, H. J. B. (1997). A review of melt migration processes in the adiabatically upwelling mantle beneath oceanic spreading ridges. *Philosophical Transactions of the Royal Society of London* 355, 283–318.

49. Kelemen, P. B., Hart, S. R., Bernstein, S. (1998) Silica enrichment in the continental upper mantle via melt/rock reaction. Earth and Planetary Science Letters. 164, 387-406.
50. Kontinen, A., (1987) An Early Proterozoic ophiolite—The Jormua mafic-ultramafic complex, northeastern Finland: *Precambrian Research*, v. 35, p. 313–341.

51. Lassiter, J. C., Byerly, B. L., Snow, J. E. & Hellebrand, E. (2014). Constraints from Os-isotope variations on the origin of Lena Trough abyssal peridotites and implications for the composition and evolution of the depleted upper mantle. *Earth and Planetary Science Letters* 403, 178–187.

52. Le Roux V., Bodinier J.-L., Tommasi A., Alard O., Dautria J.-M., Vauchez A. and Riches A. J. V. (2007) The Lherz spinel lherzolite: refertilization rather than pristine mantle. *Earth Planet. Sci. Lett.* 259, 599–612.

53. Levasseur S., Birck J.-L. & Alle`gre C. J. (1998) Direct measurement of femtomoles of osmium and the 187Os/186Os ratio in seawater. *Science* 282, 272–274.

54. Liu, C. Z., Snow, J. E., Hellebrand, E., Brügmann, G. E., von der Handt, A., Büchl, A. & Hofmann, A. W. (2008). Ancient, highly heterogeneous mantle beneath Gakkel Ridge, Arctic Ocean. *Nature* 452, 311–316.

55. Liu, C.-Z., Snow, J. E., Brügmann, G., Hellebrand, E. & Hofmann, A. W. (2009). Non-chondritic HSE budget in Earth's upper mantle evidenced by abyssal peridotites from Gakkel ridge (Arctic Ocean). *Earth and Planetary Science Letters* 283, 122–132.

56. Lorand J.-P. & Alard O. (2001). Platinum-group element abundances in the upper mantle: new constraints from in situ and whole-rock analyses of Massif Central xenoliths (France). *Geochim Cosmochim Acta* 65:2789–2806.

57. Lorand, J.-P., Luguet, A., Alard, O., Bezos, A. & Meisel, T. (2008). Abundance and distribution of platinum-group elements in orogenic lherzolites; a case study in a Fontete Rouge lherzolite (French Pyrenees). *Chemical Geology* 248, 174–194.

58. Lorand, J. P., Luguet, A. & Alard, O. (2013). Platinum-group elements systematics and petrogenetic processing of the continental upper mantle: a review. *Lithos* 164–167, 2–21.

59. Luguet, A., Shirey, S. B., Lorand, J.-P., Horan, M. F. & Carlson, R. W. (2007). Residual platinum-group minerals from highly depleted harzburgites of the Lherz massif (France) and their role in HSE fractionation of the mantle. *Geochimica et Cosmochimica Acta* 71, 3082–3097.

60. Luguet, A., Pearson, D. G., Nowell, G. M., Dreher, S. T., Coggon, J. A., Spetsius, Z. V. & Parman, S. W. (2008). Enriched Pt–Re–Os isotope systematics in plume lavas explained by metasomatic sulfides. *Science* 319, 453–456.

61. Maaløe, S. (2005). The dunite bodies, websterite and orthopyroxenite dikes of the Leka Ophiolite Complex, Norway. *Mineralogy and Petrology* 85, 163–204.

62. McDonough, W. F. & Sun, S-s. (1995). The composition of the Earth. *Chemical Geology* 120, 223–253.

63. Meibom, A., Sleep, N. H., Chamberlain, C. P., Coleman, R. G., Frei, R., Hren, M. T. & Wooden, J. L. (2002). Re–Os isotopic evidence for long-lived heterogeneity and equilibration processes in the Earth's upper mantle. Nature 419, 705–708.

64. Meisel, T. C., Moser, J., Wegscheider, W. (2001) Recognizing heterogeneous distribution of platinum group elements (PGE) in geological materials by means of the Re-Os system. *Fresenuius Journal of Analytical Chemistry* 370(5), 566-572.

65. Mertzman, S. A. (2000). K-Ar results from the southern Oregon-northern California Cascade Range. *Oregon Geology*. Vol. 62, No. 4, 99-122.

66. Niu, Y. L. & He´ kinian, R. (1997). Basaltic liquids and harzburgitic residues in the Garrett Transform: A case study at fastspreading ridges. *Earth and Planetary Science Letters* 6, 243–258.

67. O'Driscoll, B., Day, J. M. D., Walker, R. J., Daly, J. S., McDonough, W. F. & Piccoli, P. M. (2012). Chemical heterogeneity in the upper mantle recorded by peridotites and chromitites from the Shetland Ophiolite Complex, Scotland. *Earth and Planetary Science Letters* 333–334, 226–237.

68. O'Driscoll, B., Walker, R.J., Day, J.M., Ash, R.D., Daly, SJ. (2015). Generations of Melt Extraction, Melt–Rock Interaction and High-Temperature Metasomatism Preserved in Peridotites of the ~497Ma Leka Ophiolite Complex, Norway. *Journal of Petrology*, Vol. 59, No. 9, 1797-1828.

69. Parkinson, I. J. & Pearce, J. A. (1998). Peridotites from the Izu–Bonin–Mariana Forearc (ODP Leg 125): Evidence for mantle melting and melt–mantle interaction in a supra-subduction zone setting. *Journal of Petrology* 39, 1577–1618.

70. Pearson, D. G., Irvine, G. J., Ionov, D. A., Boyd, F. R. & Dreibus, G. E. (2004). Re–Os isotope systematics and platinum group element fractionation during mantle melt extraction: a study of massif and xenolith peridotite suites. Chemical Geology 208, 29–59.

71. Peltonen, P., Kontinen, H. & Huhma, H. (1996). Petrology and geochemistry of metabasalts from the 1.95 Ga Jormua Ophiolite, northeastern Finland. *Journal of Petrology* 37, 1359–1383.

72. Peltonen, P., Kontinen, A., and Huhma, H. (1998) Petrogenesis of the mantle sequence of the Jormua ophiolite (Finland): Melt migration in the upper mantle during Palaeoproterozoic continental break-up: *Journal of Petrology*, v. 39, p. 297–329.

73. Peltonen, P., Mänttäri, I., Huhma, H., Kontinen, A. (2003) Archean zicons from the mantle: The Jormua ophiolite revisited. *Geological Society of America* v. 31, no. 7, 645-648.

74. Prestvik T. (1972) Alpine-type mafic and ultramafic rocks of Leka, Nord-Trøndelag. *Norsk Geol Unders* 273: 33–34.

75. Putchel, I. S., Touboul, M., Blichert-Toft, J., Walker, R. J., Brandon, A. D., Nicklas, R. W., Kulikov, V. S., Samsonov, A. V. (2016). Lithophile and siderophile element systematics of Earth's mantle at the Archean-Proterozoic boundary: Evidence from 2.4 Ga komatiites. *Geochimica et Cosmochimica Acta* 180, 227-255.

76. Quick, J. E. (1981) Petrology and Petrogenesis of the Trinity Peridotite, an Upper Mantle Diapir in the Eastern Klamath Mountains, Northern California. *Journal of Geophysical Research*, Vol. 86, No. B12, 11,837-11,863.

77. Rampone, E., Borghini, G., Hofmann, A.W., Class, C., Cipriani, A., Zanetti, A., Goldstein, S., 2011. Upper mantle isotopic heterogeneities – global overview with new results from Alpine–Apennine ophiolites. *Fall Meeting Suppl., Abstract*, V41G-03.

78. Rampone, E. & Hofmann, A. W. (2012). A global overview of isotopic heterogeneities in the oceanic mantle. *Lithos*. 148. 247-261.

79. Rehkämper, M. & Halliday, A. N. (1997). Development and application of new ion-exchange techniques for the separation of the platinum group and other siderophile elements from geological samples. *Talanta* 44, 663–672.

80. Reisberg, L. & Lorand, J.-P. (1995). Longevity of sub-continental mantle lithosphere from osmium isotope systematics in orogenic peridotite massifs. *Nature* 376, 159-162.

81. Rudnick, R. L. & Walker, R. J. (2009). Interpreting ages from Re–Os isotopes in peridotites. *Lithos* 112S, 1083–1095.

82. Saal, A. E., Takazawa, E., Frey, F. A., Shimizu, N., Hart, S. R. (2000). Re-Os Isotopes in Horoman Peridotite: Evidence for Refertilization?. *Journal of Petrology* Vol. 42 No. 1. 25-37.

83. Schulte, R. F., Schilling, M., Horan, M. F., Anma, R., Komiya, T., Farquhar, J., Piccoli, P. M., Pitcher, L. & Walker, R. J. (2009). Chemical and chronologic complexity in the convecting upper mantle: evidence from the Taitao Ophiolite, southern Chile. *Geochimica et Cosmochimica Acta* 73, 5793–5819.

84. Sharma, M. & Wasserburg, G. J. (1996). The neodymium isotopic compositions and rare earth patterns in highly depleted ultramafic rocks. *Geochimica et Cosmochimica Acta* 60, 4537–4550.

85. Sharma, M., Wasserburg, G. J., Papanastassiou, D. A., Quick, J. E., Sharkov, E. V., Laz'ko, E. E. (1995). High $^{143}Nd/^{144}Nd$ in extremely depleted mantle rocks. *Earth and Planetary Science Letters.* 135. 101-114.

86. Shirey, S. B. & Walker, R. J. (1995). Carius tube digestion for low blank rhenium–osmium analysis. *Analytical Chemistry* 67, 2136–2141.

87. Shirey, S. B. &Walker, R. J. (1998). The Re–Os isotope system in cosmochemistry and high-temperature geochemistry. *Annual Review of Earth and Planetary Sciences* 26, 423–500.

88. Snow, J. E., Hart, S. R. & Dick, H. J. B. (1994). Nd and Sr isotopic evidence for a link between mid-ocean ridge basalts and abyssal peridotites. *Nature* 371, 57–60.

89. Snow, J. E. & Dick, H. J. B. (1995). Pervasive magnesium loss by marine weathering of peridotite. *Geochimica et Cosmochimica* Vol. 59, No. 20, 4219-4235.

90. Snow, J. E. & Reisberg, L. (1995). Os isotopic systematics of the MORB mantle: results from altered abyssal peridotites. *Earth and Planetary Science Letters* 133, 411–421.

91. Snow, J. E., Schmidt, G., Rampone, E. (1999). Os isotopes and highly siderophile elements (HSE) in the Ligurian ophiolites, Italy. *Earth and Planetary Science Letters* 175, 119-132.

92. Snow, J.E., Schmidt, G., Rampone, E. (2000). Os isotopes and highly siderophile elements (HSE) in the Ligurian ophiolites, Italy. Earth and Planetary Science Letters 175, 119–132.

93. Sobolev, A. V., Hofmann, A. W., Sobolev, S. V., Nikogosian, I. K. (2005). An olivine-free mantle source of Hawaiian shield basalts. *Nature* 434, 590-597.

94. Sobolev, A. V., Hofmann, A. W., Kuzmin, D. V., Yaxley, G. M., Arndt, N. T., Chung, S.-L., Danyushevsky, L. V., Elliott, T., Frey, F. A., Garcia, M. O., Gurenko, A. A., Kamenetsky, V. S., Kerr, A. C., Krivolutskaya, N. A., Matvienkov, V. V., Nikogosian, I. K., Rocholl, A., Sigurdsson, I. A., Sushchevskaya, N. M. & Teklay, M. (2007). The amount of recycled crust in sources of mantle derived melts. *Science* 316, 412–417.

95. Sobolev, A. V., Hofmann, A. W., Brügmann, G., Batanova, V. G. & Kuzmin, D. V. (2008). A quantitative link between recycling and osmium isotopes. *Science* 321, 536.

96. Standish, J. J., Hart, S. R., Blusztajn, J., Dick, H. J. B., Lee, K. L., (2002). Abyssal peridotite osmium isotopic compositions from Cr-spinel. *Geochemistry, Geophysics, Geosystems* 3(1) (n. 2001GC000161).

97. Stracke, A., Snow, J. E., Hellebrand, E., von der Handt, A., Bourdon, B., Birbaum, K. & Günther, D. (2011). Abyssal peridotite Hf isotopes identify extreme mantle depletion. *Earth and Planetary Science Letters* 308, 359–368.

98. Sturt, B. A. & Ramsay, D. M. (1994). The structure and regional setting of the Skei Group, Leka, north-central Norway. *NGU* 426, 31-36.

99. Takazawa E., Frey F. A., Shimizu N. and Obata M. (2000) Whole rock compositional variations in an upper mantle peridotite (Horoman, Hokkaido, Japan): are they consistent with a partial melting process? *Geochim. Cosmochim. Acta* 64, 695–716.

100. The Isotope Geochemistry Lab HSE Manual. *University of Maryland*. 2012.

101. Titus, S. J., Fossen, H., Pedersen, R. B., Vigneresse, J. L. & Tikoff, B. (2002). Pull-apart formation and strike-slip partitioning in an obliquely divergent setting, Leka Ophiolite, Norway. *Tectonophysics* 354, 101–119.

102. Trommsdorff, V., López Sánchez-Vizcaino, Gomez-Pugnair, M. T., Müntener, O. (1998). High pressure breakdown of antigorite to spinifex-textured olivine and orthopyroxene, SE Spain. *Contributions to Mineral Petrology* 132: 139-148.

103. Tsuru, A., Walker, R.J., Kontinen, A., Peltonen, P., Hanski, E., (2000) Re–Os isotopic systematics of the 1.95 Ga Jormua Ophiolite Complex, northeastern Finland. *Chemical Geology* 164, 123-141.

104. Van Acken, D., Becker, H.,Walker, R.J., (2008). Refertilization of Jurassic oceanic peridotites from the Tethys Ocean – implications for the Re–Os systematics of the upper mantle. Earth and Planetary Science Letters 268, 171–181.

105. Walker, R. J.,Shirey, S. B. & Boyd, F.R. (1989).Os, Sr,Nd, and Pb isotope systematics of Southern African peridotite xenoliths; implications for the chemical evolution of subcontinental mantle. *Geochimica et Cosmochimica Acta* 53, 1583–1595.

106. Walker, R. J., Horan, M. F., Morgan, J. W., Becker, H., Grossman, J. N., Rubin., A. E. (2002) Comparative 187Re-187Os systematics of chondrites: Implications regarding early solar system processes. *Geochimica et Cosmochimica Acta* 66, 4187-4201.

107. Warren, J. M., Shimizu, N., Sakaguchi, C., Dick, H. J. B. & Nakamura, E. (2009). An assessment of mantle heterogeneity based on abyssal peridotite isotopic compositions. *Journal of Geophysical Research* 114, B12203.

108. Workman, R. K. & Hart, S. R. (2005). Major and trace element composition of the depleted MORB mantle (DMM). *Earth and Planetary Science Letters* 231, 53-72.

109. Yaxley, G. M. & Green, D. H. (1998). Reactions between eclogite and peridotite: mantle refertilisation by subduction of oceanic crust. *Schweizerische Mineralogische und Petrographische* Mitteilungen 78, 243–255.